Gradient Statistics for Cosmic Microwave Background Analysis

Master of Science Thesis by
Cathrine Udnes
Institute of Theoretical Astrophysics
University of Oslo

June, 2011

Preface

Since the 1990's the temperature anisotropies of the Cosmic Microwave Background (CMB) have been observed with the COBE satellite and recently with the WMAP satellite. Anomalies in the CMB have been detected in this data by several different research groups using various methods. Some of these anomalies are an asymmetry in the northern and southern hemispheres, a cold spot in the southern hemisphere and a lack of structure in the northern hemisphere.

In this work statistical tests based on the gradients of the CMB temperature have been investigated, and one of these statistics can detect a preferred direction. It gives anomalously small or large values if the gradients align or avoid a particular direction. A preferred direction in the CMB could possibly be due to some large scale pattern, and a detection of a preferred direction could indicate that the universe is not isotropic.

If a large scale pattern were to be detected this could be caused by cosmic strings, other defects or by rotation. The Bianchi VII_h model is a model of a rotating universe, and has been investigated here.

But these statistical tests can also detect other anomalies. Because of the reported asymmetry in the two hemispheres the preferred direction statistic, and the function used to evaluate it, were also applied to these individually to see if it could detect this effect or gain any new information it. These anomalies in the CMB are interesting as they could provide insights into new physics.

These statistics ability to detect any primordial non-Gaussianity was also investigated to see if it could be used to put further constraints on its amplitude, f_{NL}. A detection of non-Gaussianity could give information about inflation, the hypothetical period of rapid expansion in the early universe. Inflation is a very popular model as it solves problems in the Big Bang scenario and provides a mechanism to create the CMB fluctuations.

Along with the Bianchi VII_h model and the model with primordial non-Gaussianity these statistical tests have also been tested for their sensitivity to foregrounds, point sources, and a dipole. It is useful to consider these effects so as to be sure that they do not contaminate the results from the observational data.

It was also considered of interest to look at the power spectra of the gradients. The main focus here has been on the positive gradient power spectrum. This power spectrum can be estimated using the MASTER algorithm which compensates for beam, noise and masks in the data. Previously this algorithm has been used to estimate the CMB temperature power spectrum and polarization power spectra.

The gradient power spectrum can be used as a consistency check, and it has also been compared to the E-mode polarization power spectrum. This comparison could be a useful tool when better estimates of this power spectrum has been made. The gradient power spectrum has also been used to look for point sources in the data and how their strength depends on the frequency.

With these tools the seven year WMAP data will be compared to simulations of CMB sky maps based on the ΛCDM model with Guassian anisotropies. Perhaps we can learn something new from these tests and gain valuable tools for further CMB analysis, or perhaps it will simply confirm that the CMB is very close to what it is expect to be.

Cathrine Udnes

Acknowledgments

I wish to thank my supervisor Hans Kristian Eriksen for the choice of topic which has been a very interesting introduction to CMB analysis. I am also thankful for all his help, thoughts and suggestions throughout this project.

I also wish to thank Frode Hansen, Michele Liguori and Sabino Matarrese for letting me use the simulated non-Gaussian CMB maps that they have made. Also special thanks to Frode Hansen for helping me out with the MASTER algorithm.

I acknowledge use of the Legacy Archive for Microwave Background Data Analysis (LAMBDA)[1], and the HEALPix software [2].

[1] see http://lambda.gsfc.nasa.gov/

[2] http://healpix.jpl.nasa.gov/

Contents

List of Figures

Part I

Introduction

Chapter 1

Cosmology and the Cosmic Microwave Background

Cosmology is the study of the universe as a whole, from the early universe to structure formation and its evolution. With Einstein's theory of General Relativity it became possible to construct cosmological models describing the universe we live in, and with the discovery of the Cosmic Microwave Background (CMB) these models could be tested. The detection of the CMB has resulted in a lot of observational data, and this has enabled us to gain further knowledge of the early universe.

1.1 The Cosmic Microwave Background

In the early universe matter and radiation were coupled through Thomson scattering. Photons would scatter off free electrons causing the photons to be in equilibrium, and the universe to be optically thick. The high energy of the photons ensured that any atom that was formed would immediately be destroyed, keeping the atoms ionized. These high energy photons, and the large amount of photons compared to baryons, caused the first stable hydrogen atoms to form during the epoch of recombination when the temperature had dropped to about 3000K. Thus matter and radiation decoupled during this epoch as there were fewer free electrons and less scattering. This happened approximately 400 000 years after the Big Bang, and since then these photon have travelled freely through the universe. It is these photons that make up the Cosmic Microwave Background (CMB) radiation, and so the earliest radiation we can observe today is the CMB.

From this radiation information about the composition, structure formation and geometry of the universe can be found. Currently the best-fit model to the observational data is a flat (Euclidean) universe, with $\sim 70\%$ dark energy (Λ), $\sim 25\%$ cold dark[1] matter (CDM) and $\sim 5\%$ baryonic matter (i.e. atoms). This model is known as the ΛCDM model. However, there are still many unanswered questions about dark energy

[1]Dark matter is called dark because it does not interact with other particles other than through gravity.

and dark matter although some of the properties of dark matter has been inferred from observational data, see Dodelson and references therein [13].

The CMB radiation was first detected by Penzias and Wilson in 1965, [38]. They observed a source of radiation with a temperature of 3K which was uniform in all directions. Today this temperature has been measured to be 2.725K. The detection of the CMB radiation in 1965 was also sufficient evidence to favour the Big Bang model over the steady state model which were the two main cosmological models being debated at the time. This was because the CMB was a prediction of the Big Bang model. Since then several experiments have been preformed to measure the CMB temperature, [13].

In the 1990's the Cosmic Background Explorer (COBE) satellite measured the CMB temperature black body spectrum. It was also the first experiment to detect the temperature anisotropies.

Today seven years of observational data from the Wilkinson Microwave Anisotropy Probe (WMAP) is available[2]. Although it completed its observations in 2010, the nine year data release is yet to come in 2012. With its $13'$ beam and full sky coverage WMAP has a higher resolution than previous missions to explore the CMB, like the COBE satellite. It also observed at 5 different frequencies. The interested reader can refer to [5], [30], and [37] for more details on the WMAP satellite.

However, ESA's Plank satellite has even higher resolution in more frequencies. It is currently operating, and is planned to observe for a few years. With the measurements provided by the Plack satellite it is thought that many of the remaining questions about the CMB will be answered, and that the high resolution of Plack means that it will be able to extract all the primordial information from the CMB.

1.2 Inflation

Inflation is a hypothetical period of rapid, exponential, expansion that may have taken place very early in the history of the universe, i.e. before nucleosynthesis. Inflation was proposed as a mechanism to solve the problems of the Big Bang model, like the flatness problem and the horizon problem, see Guth, [20].

The flatness problem, that we observe the universe to be very close to flat today, is a problem because this would mean a fine tuning of the universe very early on. Inflation solves this problem when a large expansion would drive the universe towards flat even if this was not the case in the beginning.

The other problem, the horizon problem, arises because the CMB is observed to be uniform in all directions even though regions on opposite sides of the universe should not have been in causal contact. This is solved by inflation because regions separated by large distances today were in causal contact before and during inflation. At that time the regions got the initial conditions, smoothness and perturbations we observe today.

[2] see http://lambda.gsfc.nasa.gov/

Another problem is the magnetic monopole problem. The Big Bang model predicts the existence of magnetic monopoles, but these have not been observed. However, the large expansion would reduce their density so that it is unlikely that we observe them today.

These are some of the problems of the Big Bang model, but there are also other problems that have been predicted like several topological defects, for example textures and domain walls, [13].

But inflation does not just provide a means to solve problems in the Big Bang model. It also gives a mechanism for producing the primordial fluctuations and the CMB temperature anisotropies, as well as the density perturbations which are the seeds of large scale structure. Thus it is possible to use the measurements of the anisotropies to differ between inflationary models. This can be done by measuring the deviation from Guassianity of the anisotropies, [4]. Inflation also predicts the production of primordial gravitational waves, [31]. These waves would cause the B-mode polarization in the CMB. Thus measuring the CMB polarization is of great interest as this would also give information about inflation.

1.3 In Search of Non-Gaussianity

One of the basic assumptions in cosmology is that the CMB is Gaussian, which is presumably due to inflation. That is, the Fourier components are uncorrelated and have random phases. However, inflationary models predicts different levels of Gaussianity, and so by measuring any deviation from Guassianity it is possible to narrow down the number of inflationary models for our universe, [4].

Many tests have been applied to the data from the WMAP satellite to search for any deviations from Gaussianity, and to put constraints on the primordial non-Gaussianity amplitude, f_{NL}, [11],[25]. Through these analysis some detections of non-Gaussianity have been made, and anomalies have also been found. Some of these are a cold spot in the southern hemisphere which could be a source of non-Gaussianity,see [42], as well as an asymmetry in the two hemispheres, see [14],[15], [27], and references therein. There has also been reports on other cold spots, and a lack of structure in the northern hemisphere, see [39], [40].

However, the WMAP team has found that there is no asymmetry, and stated that the greatest discovery is that there is no great discovery, everything is as expected, [7]. But the asymmetry in the two hemispheres, and the various anomalies, have been detected by several different research groups.

In this work statistical tests based on the gradients of the CMB temperature will be applied to the seven year WMAP data. One of these statistics can detect a preferred direction in the CMB. This statistic, along with the direction function, could possibly detect an asymmetry or other anomalies in the CMB.

1.4 Are there anomalies in the CMB?

In this work a preferred direction statistic has been applied to the WMAP seven year data of the CMB temperature. This statistic was proposed by Bunn and Scott, [8], and could potentially detect a large scale pattern. Such a pattern could be caused by rotation or shear, i.e. a rotating universe, or topological defects like cosmic strings. This statistic can also be used to look for foreground contamination, for a dipole or point sources which may be in the data. It has already been proposed by Hanson et al.,[23] to use this statistic to look for foreground contamination in the polarization data as these foregrounds are uncertain.

This statistic and the direction function have also been used to look for other anomalies and the asymmetry of the northern and southern hemispheres that has been reported, [14], [15], [39], [42]. The direction function is the function from which the preferred direction statistic is evaluated. This functions maximum and minimum values have here been treated as two separate statistical tests. The advantage of this function is that it could detect anomalies even if these do not cause a preferred direction. Any detection of anomalies or a preferred direction could give new insights into the physics of the CMB.

The preferred direction statistic and the direction function requires the calculation of the gradients of the CMB. It then uses these to see whether there is a particular direction they align with or avoid. We therefore need expressions for these gradients on the sphere along with a mathematical description of the CMB temperature.

As for the temperature anisotropies and polarization it is also possible to estimate the power spectra of the temperature gradients. This might give additional information about the CMB. As we are already working with the gradients of the temperature maps it was considered of interest to find their power spectra as well. In order to do this the MASTER algorithm (Monte Carlo Apodized Spherical Transform Estimator) was used to estimate the power spectra from the WMAP data, and has therefore been treated here, [26]. It might also be of interest to compare this power spectrum to the E-mode polarization power spectrum or use it to look for point sources in the CMB.

Chapter 2

Physics of the CMB

Before we develop the formalism which we will use to treat the CMB temperature sky maps, and find the gradients, we will look at the equations that govern the evolution of the temperature perturbations. As photons couple to electrons, electrons to protons, and since the baryons affects the gravitational potential, which again affects all the other components, it is a large set of coupled equations that has to be solved. From these equations it will be shown that we can find the temperature power spectrum, which can also be estimated from the observational data. Thus we have a quantity that can be used to compare theory and observation. We are also interested to know what happened before recombination, and what models that actually describes an inflationary era in the early universe. Here only a short and general introduction to these topics will be made to show some of the physics of the CMB.

2.1 Preliminaries

Before we can find the equations that give the perturbations to the temperature, we need to know about the background cosmology. We begin with the geometry which is described by the Friedmann-Robertson-Walker metric

$$ds^2 = -c^2dt^2 + a^2(t)(dx^2 + dy^2 + dz^2), \tag{2.1}$$

where $a(t)$ is the scale factor, which is a function of time describing the expansion of the universe. This metric describes distances in four dimensional space for a flat universe. It can also be written in a more general way as

$$ds^2 = \sum_{\mu,\nu=0}^{3} g_{\mu\nu}dx^\mu dx^\nu. \tag{2.2}$$

We will also need the definition of conformal time, η, which is the distance light has travelled since $t = 0$, so

$$\eta = \int_0^t \frac{dt'}{a(t')}. \tag{2.3}$$

This is important because no information could have propagated further than η. This is also the particle horizon because regions separated by distances greater than η are not causally connected. When finding the perturbation equations it is convenient to change to conformal time before writing down the final expressions.

We will also need an expression for the optical depth τ. In the early universe atoms were ionized, and photons scattered of free electrons through Thomson scattering. Because of this scattering photons were constantly changing direction making the universe optically thick until electrons and protons combined to atoms during recombination. The optical depth, τ, is given by, using conformal time,

$$\tau(\eta) = \int_{\eta}^{\eta_0} n_e \sigma_T a d\eta'. \tag{2.4}$$

σ_T is the Thomson cross section and n_e is the free electron density. In order to find the number of free electrons the Saha equation and Peebles equation must be used, see [9] and [13].

Finally we also need an expression for the Hubble rate $H(t)$, which measures how rapidly the scale factor changes. This can be found from one of the Friedmann equation which can be derived from the Einstein equations of general relativity (see section 2.2) with Eq.(2.1) as the metric. The Friedmann equation we are interested in relates the scale factor, density and the curvature through

$$\frac{\dot{a}^2}{a^2} + \frac{kc^2}{a^2} = \frac{8\pi G\rho}{3}. \tag{2.5}$$

For a flat universe $k = 0$ and the critical density is $\rho_{\text{crit}} = 3H_0^2/8\pi G$, i.e. it is the energy density required for the universe to be flat. Using this with the definitions $H(t) = da/dt/a = \dot{a}/a$, $\Omega_{\text{X}} = \rho_{\text{X}}/\rho_{\text{crit}}$, with ρ_{X} the density of either baryons, radiation, dark energy or dark matter (i.e. X denotes the species), the Friedmann equation becomes

$$H(t) = H_0\sqrt{(\Omega_m + \Omega_b)a^{-3} + \Omega_r a^{-4} + \Omega_\Lambda} \tag{2.6}$$

where $H_0 = 100h$ km s^{-1} Mpc^{-1} with $h = 0.72 \pm 0.08$. The derivation of Eq.(2.5) can be found in [13].

2.2 Perturbations to the Gravitational Potential

We will now look at the equations for the perturbations to the gravitational potential. To describe these perturbations we use the Newtonian gauge with the metric

$$ds^2 = -c^2(1 + \Psi)dt^2 + a^2(t)(1 + \Phi)(dx^2 + dy^2 + dz^2). \tag{2.7}$$

Here Φ and Ψ correspond to the perturbation to the space-time curvature and the perturbation to the Newtonian potential, respectively. This only considers scalar perturbations, but equations for tensor perturbations can also be derived, see [13]. We can now find the Einstein equations for this metric.

The Einstein equations relate the metric to the matter and energy in the universe, see [16] and [24] for more details on general relativity. Thus the Einstein equations relates the components of the Einstein tensor, which describes geometry, to the energy-momentum tensor, which describes the energy,

$$G_{\mu\nu} = R_{\mu\nu} - \frac{1}{2}g_{\mu\nu}\mathcal{R} = 8\pi G T_{\mu\nu}. \tag{2.8}$$

Here $G_{\mu\nu}$ is the Einstein tensor, $R_{\mu\nu}$ is the Ricci tensor, $\mathcal{R}$ is the Ricci scalar, G is Newton's constant, and $T_{\mu\nu}$ is the energy-momentum tensor. The Ricci tensor is given by

$$R_{\mu\nu} = \Gamma^{\alpha}_{\mu\nu,\alpha} - \Gamma^{\alpha}_{\mu\alpha,\nu} + \Gamma^{\alpha}_{\beta\alpha}\Gamma^{\beta}_{\mu\nu} - \Gamma^{\alpha}_{\beta\nu}\Gamma^{\beta}_{\mu\alpha} \tag{2.9}$$

where

$$\Gamma^{\mu}_{\alpha\beta} = \frac{g^{\mu\nu}}{2}\left[\frac{\partial g_{\alpha\nu}}{\partial x^{\beta}} + \frac{\partial g_{\beta\nu}}{\partial x^{\alpha}} - \frac{\partial g_{\alpha\beta}}{\partial x^{\nu}}\right]. \tag{2.10}$$

From the Ricci tensor we can find the Ricci scalar $\mathcal{R} = g^{\mu\nu}R_{\mu\nu}$ where $g^{\mu\nu}$ is defined by Eq.(2.2) and Eq.(2.7) but where the indices have to be raised. From the Ricci tensor and the Ricci scalar we can find all the components on the left hand side of Eq.(2.8).

From the energy-momentum tensor it is the energy density of the particles in the universe that is most important. The contribution from each species is an integral over its distribution function. This then gives the perturbation equations, for the metric given by Eq.(2.7), as

$$\frac{d\Phi}{dt} = \Psi - \frac{c^2k^2}{2H^2}\Phi + \frac{H_0^2}{2H^2}[\Omega_m a^{-1}\delta + \Omega_b a^{-1}\delta_b + 4\Omega_r a^{-2}\Theta_0], \tag{2.11}$$

and

$$\Psi = -\Phi - \frac{12H_0^2}{c^2k^2a^2}\Omega_r\Theta_2. \tag{2.12}$$

All the derivations can be found in [13]. These are the perturbation equations for the gravitational potential.

2.3 The Temperature Anisotropies

To find the photon distribution, and so the equation for the temperature perturbations, we have to solve for all components. We have already found the equations for the perturbations to the gravitational potential in section 2.2, but we still need equations for the perturbations to the baryons and dark matter, and also neutrinos. The equations of motion for the perturbations to the photons, baryons, dark matter and neutrinos can be derived from the Boltzmann equations. The Boltzmann equation gives the abundance of a particle as the difference between the rate of production and elimination. Generally the unintegrated Boltzmann equation is

$$\frac{df}{dt} = C[f] \tag{2.13}$$

where C[f] accounts for all possible collision terms. We are interested in the perturbation to the photon temperature, this can be described by

$$T(\vec{x}, \hat{p}, \eta) = T(\eta)[1 + \Theta(\vec{x}, \hat{p}, \eta)]. \tag{2.14}$$

$T(\eta)$ is the zero-order temperature which describes the smooth universe with the photons distributed homogeneously and isotropically, which is why $T(\eta)$ is independent of position and direction. $\Theta(\vec{x}, \hat{p}, \eta)$ is the perturbation to the smooth zero-order universe, which allows for inhomogeneities and anisotropies, i.e. dependence on the position and direction. It is the directional dependence which leads to the temperature anisotropies.

The derivation for the perturbation equation for photons can be found in [13], but here only the result will be quoted. When using conformal time and changing to Fourier space the perturbation equation for the photons become

$$\dot{\tilde{\Theta}} + ik\mu\tilde{\Theta} + \dot{\tilde{\Phi}} + ik\mu\tilde{\Psi} = -\dot{\tau}[\tilde{\Theta}_0 - \tilde{\Theta} + \mu\tilde{v}_b] \tag{2.15}$$

where $\tilde{}$ indicates Fourier space and $\dot{}$ is the derivative with respect to conformal time. This convention is used throughout the rest of this section.

Because dark matter does not interact with any other particles, other than through gravity, there is no collision term in the Boltzmann equation for these particles. The particles are also massive and non-relativistic so that we obtain equations for the density and velocity. This is because we can take only the first two moments of its equations instead of keeping an arbitrary directional dependence. Using again conformal time and changing to Fourier space we get the density equation

$$\dot{\tilde{\delta}} + ik\tilde{v} + 3\dot{\tilde{\Psi}} = 0, \tag{2.16}$$

and the velocity equation

$$\dot{\tilde{v}} + \frac{\dot{a}}{a}\tilde{v} + ik\tilde{\Psi} = 0, \tag{2.17}$$

were v is the velocity and δ is the density of dark matter.

Finally, baryons are also non-relativistic, but unlike dark matter, we have Coulomb scattering which couples the protons and electrons. Including this, again using conformal time and changing to Fourier space, we have, as for cold dark matter, two equation. The density equation is identical to that found for dark matter,

$$\dot{\tilde{\delta}}_b + ik\tilde{v}_b + 3\dot{\tilde{\Psi}} = 0. \tag{2.18}$$

However, the velocity equation now becomes

$$\dot{\tilde{v}}_b + \frac{\dot{a}}{a}\tilde{v}_b + ik\tilde{\Psi} = \dot{\tau}\frac{4\rho_\gamma}{3\rho_b}[3i\tilde{\Theta}_1 + \tilde{v}_b]. \tag{2.19}$$

Here v_b and δ_b are the velocity and density of baryons. For a complete treatment the neutrino equations are also required, but they will not be included here. All the

derivations of these equations can be found in [13], and all the equations are also listed in [9]. All these equations, along with the perturbation equations to the gravitational potentials, describe the evolution of the of the perturbations with time.

By solving all of these coupled differential equations it is possible to calculate the temperature anisotropies, and from these find the temperature power spectrum, which is useful when comparing cosmological models with the CMB data. This is also interesting as we later on will set up the formalism required to estimate the power spectrum from the observational data (see section 3.2), and use this formalism to estimate the gradient power spectrum. The power spectrum in terms of the perturbations to the temperature, Θ_l, is given by

$$C_l = \int \frac{d^3k}{(2\pi)^3} P(k)\Theta_l^2(k). \tag{2.20}$$

Here P(k) is the primordial power spectrum from inflation. This spectrum can be given by Harrison-Zel'dovich spectrum,

$$\frac{k^3}{2\pi^2}P(k) = \left(\frac{ck}{H_0}\right)^{n-1}, \tag{2.21}$$

which is predicted by most inflationary models. The ΛCDM model best-fit power spectrum to the WMAP data is shown in Fig.2.1. The power spectrum is plotted as $C_l l(l+1)/2\pi$ as its overall trend is to drop as l^{-2}.

The power spectrum is important because it can tell us a lot about the universe we live in. The first acoustic peak can tell us about the geometry of the universe. Dependent on whether the universe is flat, open or closed the first peak will be at higher or lower l because the geometry is given by the angular size of the horizon. In a flat universe the photon geodesics are parallel, in a closed universe the geodesics will converge, and in an open universe they will diverge, so the angular size of the horizon will be larger or smaller for a closed or open universe respectively. So in a flat universe the first acoustic peak is at $l = 220$, but if the universe is open the peak will move to smaller scales or $l > 220$. In a closed universe the peak will be at larger angular scales or at $l < 220$.

From the higher peaks it is possible to get a measure of the baryon density. Dark matter will set up a gravitational potential in which matter and radiation will oscillate. The matter will be acted on by gravity and contract. As matter contracts the pressure increases, so that the matter will expand when the pressure is greater than gravity before contracting again when the pressure is no longer dominating. When the baryons and photons oscillate sound waves are created which propagate through the universe. The modes will begin to grow when the horizon is larger than the wavelength. As time passes the horizon becomes larger, and larger scales begin to oscillate, but after recombination the CMB is "frozen". In the power spectrum we can see the acoustic peaks created from the compressions and decompressions of the matter. The first peak corresponds to a compression, the second to a decompression, the third to a compression, and the fourth to a decompression.

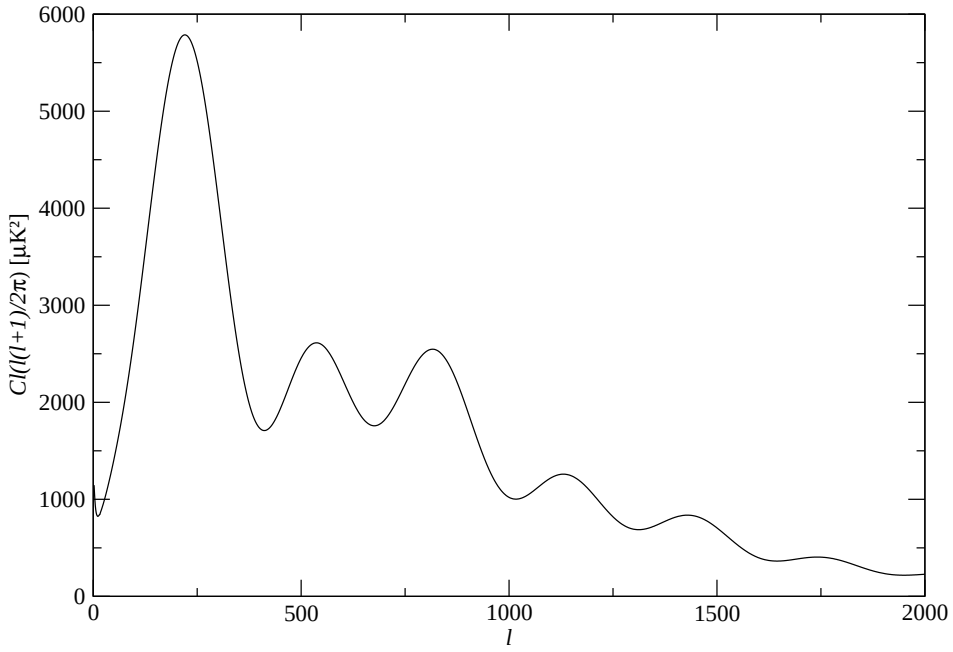

Figure 2.1: Best-fit temperature power spectrum for the ΛCDM model from the WMAP data. Here plotted as $C_l(l(l+1)/2\pi)$.

The baryon density also corresponds directly to the CMB temperature. Areas of high density gives lower temperature and areas of low density gives larger temperatures as the photons lose energy when they travel out of gravitational potentials. If there are more baryons these will add to the potential during compressions. This makes the compressions stronger than the decompressions, so that the odd peaks are larger than the even peaks. As the first and third peak are caused by compressions these can give information about the amount of baryons.

It is also possible to get information about inflation by looking at the power spectrum for $l < 50$. One prediction of inflation is that the spectrum should be almost scale invariant. So there is no characteristic scale, and the fluctuations are equally strong on all scales (i.e. flat spectrum). From the initial conditions of inflation there are two relevant parameters an amplitude A and a tilt parameter n_s so that

$$C_l = A\left(\frac{l}{l_0}\right)^{n_s-1}. \tag{2.22}$$

This can be fitted to the power spectrum to get estimates of the amplitude and tilt

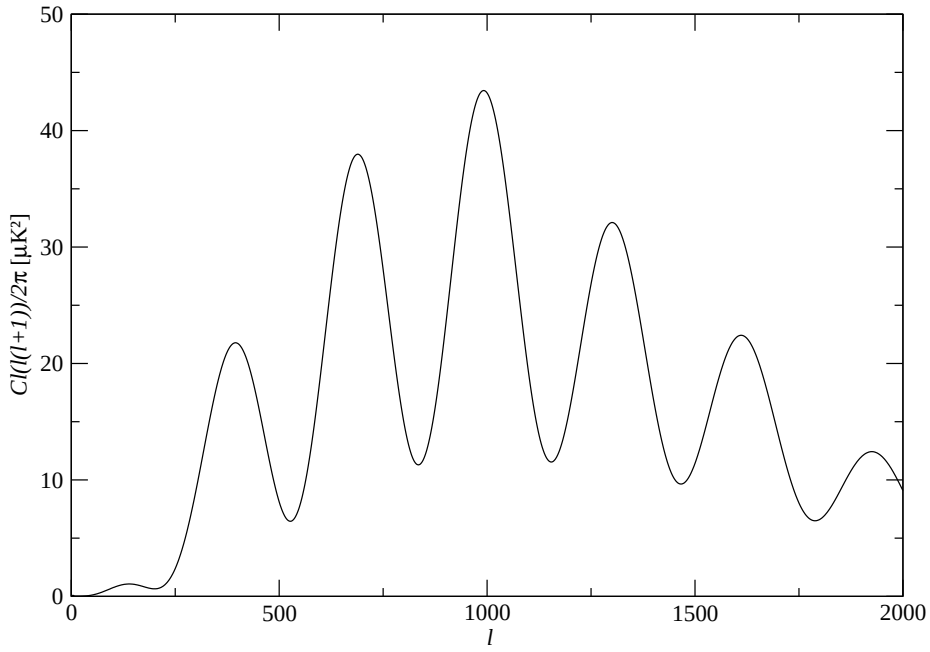

Figure 2.2: Best-fit E-mode polarization power spectrum for the ΛCDM model from the WMAP data, here plotted as $C_l(l(l+1)/2\pi)$.

parameter.

These are some of the parameters of the universe that can be estimated from the power spectrum. Other parameters are the matter density, and the cosmological constant, but there is also the effect of reionization, i.e. change in optical depth τ, and the effect of tensor perturbations which will affect the temperature power spectrum, see [13] for the details. The first two of these, along with the baryon density and curvature, have the most distinct effects on the power spectrum, and are therefore the easiest to extract estimates of.

2.4 Polarization

As the primordial photons travel through the hot electron gas on their way to us they get rescattered. This rescattering can cause the photons to become polarized. The radiation is polarized if the intensity in the two transverse directions is unequal. In order for this to happen there has to be a quadrupole to give different intensity to

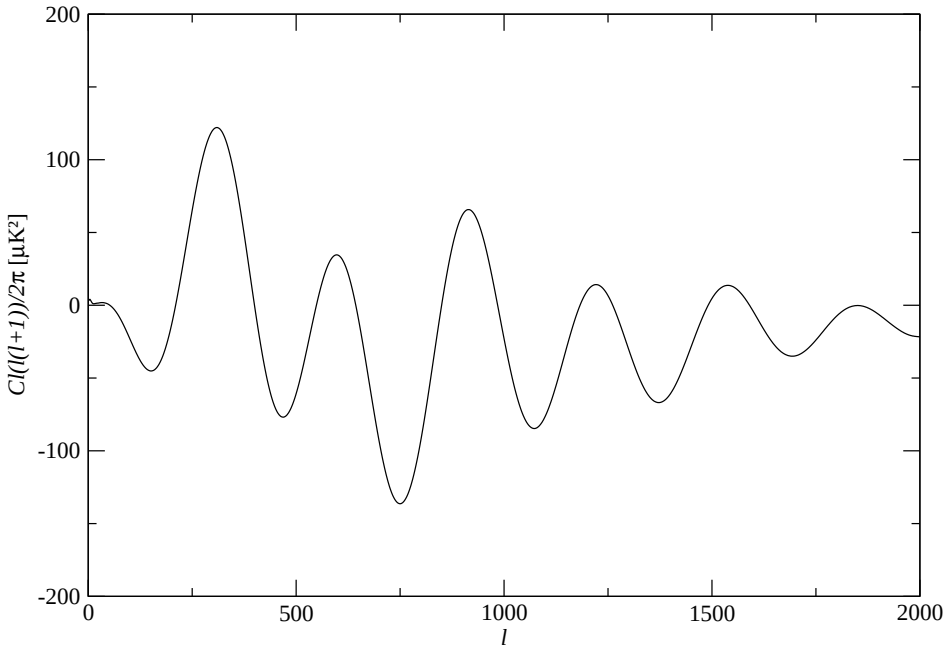

Figure 2.3: Best-fit temperature and E-mode polarization cross-correlation (TE) power spectrum for the ΛCDM model from the WMAP data. Here plotted as $C_l(l(l+1)/2\pi)$.

the photons from different directions. This is the case before matter and radiation decouples. These photons then scatter of the electrons through Thomson scattering, and get polarized in the direction of observation. This is the polarization from the last scattering that we can observe today, [13].

It is however difficult to detect the polarization because of noise and also because there is not enough knowledge about the polarization foregrounds. One of the effects is from reionization. Electrons from this epoch rescatter the CMB photons which distorts the CMB spectrum and dilutes the temperature fluctuations. This effect of the polarized photons from reionization can be seen on large scales. Also lensing distorts the polarization by deflecting changes in spatial patterns. However, it is also possible to learn something about lensing and reionization from observing these effects, [31], [47].

The kind of polarization described above is caused by scalar perturbations, and gives the E-mode polarization of the CMB. The power spectrum for the E-mode and the cross correlation power spectrum for E-mode and temperature are shown in Figs.2.2 and 2.3, respectively. There is also another type of polarization, the B-mode polarization, caused

by tensor perturbations, or gravitational waves. Generation of gravitational waves is a prediction of inflation, and thus detection of the B-mode would give further information about inflation.

2.5 Inflationary Models

There are various inflationary models, and most of them predict Gaussian, adiabatic, nearly scale-invariant primordial fluctuations. Because inflation almost always predicts Guassianity and isotropy it is important in this work as we will use the preferred direction statistic and direction function to look for anomalies which would be in disagreement with this.

Generally inflation is a hypothetical period of rapid expansion in the early universe. This expansion is thought to be exponential and can therefore be described by the de Sitter model, [13]. In this model the relation between the scale factor and time is given by

$$a(t) \propto e^{H_0 t} \tag{2.23}$$

where $H_0 = \sqrt{\Lambda/3}$ is a constant. During this period of rapid expansion quantum mechanical fluctuations are highly amplified and their wavelengths stretched to outside the horizon. The fluctuations become "frozen-in", and this then leads to large-scale fluctuations. Gravitational waves are also created from the quantum fluctuations.

This model with constant vacuum energy solves the problems of the Big Bang scenario described in section 1.2. However, this model has no way to end the inflationary era, so the universe would inflate forever. More complicated models have therefore been developed which keeps the main idea of exponential expansion as in the de Sitter universe. These models usually contain one or more scalar fields.

Inflation also gives a mechanism for generating the primordial fluctuation as the inflationary field sets up quantum mechanical fluctuations. However, there are two types of perturbations namely adiabatic and isocurvature perturbations. Adiabatic perturbations affect all the cosmological components, baryons, dark matter, radiation and curvature, so that the relative number densities remain unperturbed. However, it is also possible to perturb the matter content without perturbing the geometry. This is the isocurvature perturbations. It is characterized by vanishing perturbations to the geometry so that instead there are variations in the particle number ratios, [33].

As inflation will begin and end at different times in different regions, this leads to energy density perturbations. Most inflationary models predicts that the temperature anisotropies in the CMB are a homogeneous and isotropic Gaussian random field. In addition a way to reheat the universe is also required in the model for inflation. This is because the expansion will cool the universe while high temperatures are required for nucleocynthesis to take place.

2.5.1 Slow-Roll Inflation

We will now take a look at one inflationary model which is driven by a scalar field, [4], [13], [36]. This is the slow-roll model, and it is one of the simplest models which requires only one scalar field[1], the inflaton. This scalar field has a potential and kinetic energy. It also has an energy density and a pressure given by

$$\rho_\phi c^2 = \frac{1}{2\hbar c^3}\dot{\phi}^2 + V(\phi), \tag{2.24}$$

$$p_\phi = \frac{1}{2\hbar c^3}\dot{\phi}^2 - V(\phi). \tag{2.25}$$

For a homogeneous scalar field the equation of motion is given by

$$\ddot{\phi} + 3H\dot{\phi} + \hbar c^3 V'(\phi) = 0, \tag{2.26}$$

where ϕ is the scalar field[2], or the inflaton, and $V(\phi)$ is the potential energy of the field. If the scalar field varies slowly with time, or rolls slowly down the potential, so that

$$\frac{\dot{\phi}^2}{2\hbar c^3} \ll V(\phi) \tag{2.27}$$

then the field will have an equation of state $p_\phi = -c^2\rho_\phi$. This is similar to the equation of stat for a cosmological constant which has a negative pressure. Using this criterion, and that the scalar field will eventually settle down in the potential with constant "velocity" then

$$\dot{\phi} = -\frac{\hbar c^3}{3H}\frac{dV}{d\phi}. \tag{2.28}$$

Using the definition of the Hubble rate, $H^2 = 8\pi G V(\phi)/3c^3$ we get

$$\left(\frac{dV}{d\phi}\right) \ll \frac{24\pi G}{\hbar c^5}V^2 = \frac{24\pi G}{E_{PI}}V^2.$$

From this we get the first of the slow-roll parameter

$$\frac{2}{3}\frac{E_{PI}^2}{16\pi}\left(\frac{V'}{V}\right)^2 \ll 1. \tag{2.29}$$

The slow-roll parameter ϵ is usually defined as

$$\frac{E_{PI}^2}{16\pi}\left(\frac{V'}{V}\right)^2 = \epsilon. \tag{2.30}$$

Another condition can also be derived on the curvature of V''. Using Eq.(2.28) we get

$$\ddot{\phi} = -\hbar c^3\frac{\dot{\phi}}{3H}V''(\phi), \tag{2.31}$$

[1] A scalar field associates a real or complex number with a point in space at a given time

[2] measured in units of energy

and using Eq.(2.28) again this gives

$$\frac{E_{PI}^2}{8}\left(\frac{V''}{V}\right) = \eta. \tag{2.32}$$

This leads to the slow-roll approximation. If the condition that $\epsilon \ll 1$ is satisfied then inflation will occur. Inflation is taken to end when $\epsilon = 1$. When inflation ends the inflaton oscillates about its potential minimum and decays. This leads to reheating of the universe. Because of the fluctuations this happens everywhere in the universe, but at different times in different regions, and results in the temperature perturbations. These perturbations are also adiabatic.

The amount which the universe has to expand in order to solve the problems of the Big Bang model is given by the number of e-foldings. This is defined as the ratio of the scale factor at the end of inflation, $a_f(t)$, to the scale factor at the beginning of inflation $a_i(t)$. So that $a_f(t)/a_i(t) = e^N$. The number of e-foldings taking place is given by

$$N = \ln\left[\frac{a(t_{end})}{a(t)}\right] = \frac{8\pi}{E_{PI}^2}\int_{\phi_{end}}^{\phi}\frac{V}{V'}d\phi. \tag{2.33}$$

Typically at least more than 50 e-foldings are required in order for inflation to solve the problems of the Big Bang model.

2.5.2 Other Models of Inflation

The models of inflation can be divided into two groups, single field inflation and hybrid models. The single field models only require one scalar field, while the hybrid models require a second field to end inflation. But this second field does not contribute to the dynamics of inflation. These different models predict smaller or larger non-Gaussianity in the CMB. In the slow-roll model described above there is only one scalar field, the inflaton, and this model predicts Gaussian temperature perturbations.

Another models is the curvaton scenario which is a hybrid model with two scalar fields, the inflaton and the curvaton. Here the final curvature perturbations are produced from an initial isocurvature perturbation associated with the quantum fluctuations of the curvaton. The curvaton is a light scalar field, and its energy density is negligible during inflation. The curvaton isocurvature perturbations are transformed into adiabatic ones when the curvaton decays into radiation some time after the end of inflation,[4], [36].

The amplitude of the primordial non-Gaussianity is given by the f_{NL} parameter. By measuring the non-Gaussianity in the CMB temperature it is possible to put constraints on the inflationary model, [4], [36].

There has also been proposed other mechanisms for generating the perturbations. There is the ghost inflationary scenario, and the D-cceleration scenario. There is also the inhomogeneous reheating scenario which causes adiabatic perturbations in the final reheating temperature in different region of the universe, see Bartolo et al. [4] and references therein for more details on these models.

Chapter 3

Mathematical Description of the CMB

The CMB is a noise-like phenomenon, and it is the amplitude of the temperature anisotropies that are of the greatest interest. As any function can be expanded in Fourier space as the sum of wave-functions times an amplitude this can also be done for the CMB temperature anisotropies. It is also easier to find the temperature gradients using the spherical harmonics, which is the equivalent of Fourier transforms on the sphere. We can also find the power spectrum using this description. Thus here will be presented the mathematical tools which will be used to treat the CMB temperature, and find the gradients so that we can evaluate the direction function and preferred direction statistic. The formalism required when finding the power spectrum and gradient power spectra will also be presented.

3.1 The CMB described in Harmonic space

The CMB temperature measured on the sky can be described in harmonic space using the spherical harmonic functions, [19]. The temperature is then given by

$$T(\theta,\phi) = \sum_{l=0}^{\infty} \sum_{m=-l}^{l} a_{lm} Y_{lm}(\theta,\phi), \tag{3.1}$$

and the expansion coefficients, a_{lm}'s, are defined by

$$a_{lm} = \int d(\cos\theta) d\phi T(\theta,\phi) Y^*_{lm}(\theta,\phi). \tag{3.2}$$

The spherical harmonics, Y_{lm}, are

$$Y_{lm} = \sqrt{\frac{2l+1}{4\pi}\frac{(l-m)!}{(l+m)!}} P_{lm} e^{im\phi}, \tag{3.3}$$

where the P_{lm}'s are the Legendre polynomials,[12]. These are wave-functions on the sphere described by l and m. Here l gives the number of waves along a meridian, and m gives number of modes along the equator. Another relation between the expansion coefficients is

$$a_{l-m} = (-1)^m a^*_{lm}. \tag{3.4}$$

This is useful when finding the power spectrum.

3.2 The Angular Power Spectrum

The power spectrum is the variance of the a_{lm}'s, and can be found from the squared amplitude of the fluctuations. Thus power on a given scale is the squared Fourier amplitude. So the temperature power spectrum is given by

$$C_l = \langle a_{lm} a^*_{lm} \rangle. \tag{3.5}$$

An unbiased estimator of C_l, if there is no noise, is given by

$$\hat{C}_l = \frac{1}{2l+1} \sum_{m=-l}^{l} |a_{lm}|^2. \tag{3.6}$$

Because the universe is assumed to be isotropic this function only has the l subscript, not the m, as the power spectrum must be the same in all directions x, y and z. Because the CMB radiation is a noise-like phenomenon it is the amplitude of the fluctuations as a function of scale that is of interest, while the specific position of a maximum or minimum is not relevant. Here l gives the angular scale.

3.3 Temperature Gradients

As we now have a formalism to express the CMB temperature in harmonic space we can find the temperature gradients needed to evaluate the direction function and preferred direction statistic. To get the covariant derivatives we can differentiate in harmonic space, and find the gradients as expression of a_{lm}'s and spherical harmonics, Y_{lm}'s. The covariant derivatives are given by

$$\nabla T = (T_{;\theta}, T_{;\phi}), \tag{3.7}$$

where

$$T_{;\phi} = \frac{1}{\sin\theta} \frac{\partial T}{\partial \phi}, \tag{3.8}$$

and

$$T_{;\theta} = \partial T / \partial \theta. \tag{3.9}$$

Thus we differentiate Eq.(3.1) with respect to θ and ϕ. To get $T_{;\phi}$ is straightforward as the only dependence on ϕ is in the exponential part of the spherical harmonic function, since

$$T(\theta,\phi)=\sum_{l=0}^{\infty}\sum_{m=-l}^{l}a_{lm}Y_{lm}(\theta,\phi)=\sum_{l=0}^{\infty}\sum_{m=-l}^{l}a_{lm}\sqrt{\frac{2l+1}{4\pi}\frac{(l-m)!}{(l+m)!}}P_{lm}e^{im\phi}. \tag{3.10}$$

When differentiating Eq.(3.10) with respect to ϕ we get

$$T_{;\phi}=\frac{i}{\sin\theta}\sum_{l=0}^{l_{max}}\sum_{m=-l}^{l}ma_{lm}Y_{lm}. \tag{3.11}$$

To get the $T_{;\theta}$ we differentiate Eq.(3.10) with respect to θ. The θ dependence is in the Legendre polynomials so we need the relation for the derivative of the associated Legendre polynomials that is

$$\frac{dP_{lm}}{d\theta}=\frac{1}{\sin\theta}\left[-\frac{(l+m)(l+1)}{2l+1}P_{l-1,m}+\frac{l(l-m+1)}{2l+1}P_{l+1,m}\right]. \tag{3.12}$$

We thus find the covariant derivative to be given by

$$\begin{aligned}T_{;\theta}=\frac{1}{\sin\theta}\Bigg[&\sum_{l=2}^{l_{max}+1}\sum_{m=l+1}^{l-1}\frac{l(l+m-1)}{2l+1}a_{l-1,m}\frac{X_{l-1,m}}{X_{lm}}Y_{lm}\\&-\sum_{l=0}^{l_{max}-1}\sum_{m=-l}^{l}\frac{(l+1)(l-m+2)}{2l+3}a_{l+1,m}\frac{X_{l+1,m}}{X_{lm}}Y_{lm}\Bigg]\end{aligned} \tag{3.13}$$

$$\tag{3.14}$$

where

$$X_{lm}=\left[\frac{2l+1}{4\pi}\frac{(l-m)!}{(l+m)!}\right] \tag{3.15}$$

This gives the covariant derivatives with respect to θ and ϕ for a given map. The second derivatives can either be found by similar expressions or by applying the above expressions again to a gradient map.

3.4 Expanding Spin-fields in Harmonic Space

To treat polarization or gradients in harmonic space we need to define spin, and use the spin spherical harmonics. For a given direction on the sphere specified by the angles, (θ,ϕ), one can define three orthogonal vectors; one radial, $\vec{n}$, and two tangential to the sphere, $\hat{e}_1$, and $\hat{e}_2$. The tangential vectors are only defined up to a rotation around $\vec{n}$. A function ${}_sf(\theta,\phi)$ defined on the sphere is said to have spin s if under a right handed rotation of the tangential vectors by an angle ψ it transforms as

$${}_sf'(\theta,\phi)={}_s\,f(\theta,\phi)e^{is\psi}. \tag{3.16}$$

An arbitrary vector $\vec{a}$ on the sphere has quantities $\vec{a}\hat{e_1} + \vec{a}\hat{e_2}, \vec{a}\vec{n}, \vec{a}\hat{e_1} - \vec{a}\hat{e_2}$ with spin $|s|$, 0 , $-|s|$, [46]. The temperature anisotropies are a spin-0 field. However, polarization is a spin-2 field and the gradients a spin-1 field.

It is convenient to make linear combinations of the spin a_{lm}'s so that we get

$$a^+_{lm} = \frac{1}{2}({}_{|s|}a_{lm} + {}_{-|s|}\, a_{lm}),$$
$$a^-_{lm} = \frac{1}{2i}({}_{|s|}a_{lm} - {}_{-|s|}\, a_{lm}). \tag{3.17}$$

3.4.1 Polarization

Polarization analysis in harmonic space, using spin-weighted functions, is described by Zaldarriaga and Seljak, [46]. The polarization is given by the two Stokes parameters Q and U. Unlike the temperature, the Q and U parameters transform under rotation by an angle ψ as

$$Q' = Q\cos(2\psi) + U\sin(2\psi),$$
$$U' = -Q\sin(2\psi) + U\cos(2\psi),$$

where $\hat{e}'_1 = \cos(\psi)\hat{e}_1 + \sin(\psi)\hat{e}_2$ and $\hat{e}'_2 = -\sin(\psi)\hat{e}_1 + \cos(\psi)\hat{e}_2$. It is therefore possible to construct two quantities that have a definite value of spin, namely

$$(Q \pm iU)'(\hat{n}) = e^{\pm 2i\psi}(Q \pm iU)(\hat{n}).$$

These can then be expanded in spherical harmonics with spin-weighted basis as

$$(Q + iU)(\hat{n}) = \sum_{lm} {}_2a_{lm}\, {}_2Y_{lm}, \tag{3.18}$$
$$(Q - iU)(\hat{n}) = \sum_{lm} {}_{-2}a_{lm}\, {}_{-2}Y_{lm}. \tag{3.19}$$

With the spin a_{lm}'s a linear combination of these can be introduced such that we have

$$a_{E,lm} = -\frac{1}{2}({}_2a_{lm} + {}_{-2}\, a_{lm}), \tag{3.20}$$

$$a_{B,lm} = \frac{i}{2}({}_2a_{lm} - {}_{-2}\, a_{lm}). \tag{3.21}$$

From these we get the E-mode and B-mode power spectra. The E-mode can also be combined with the temperature to give the cross-correlation TE power spectrum. We therefore have

$$C_l^{EE} = \frac{1}{2l+1}\langle a_{E,lm} a^*_{E,lm}\rangle, \tag{3.22}$$

$$C_l^{BB} = \frac{1}{2l+1}\langle a_{B,lm} a^*_{B,lm}\rangle, \tag{3.23}$$

and

$$C_l^{TE} = \frac{1}{2l+1}\langle a_{T,lm} a^*_{E,lm}\rangle. \tag{3.24}$$

The cross correlation between the E- and B-modes, and the temperature and B-mode vanish as the B-mode has opposite parity of these. Also, the E-mode and the B-mode behave differently under parity transformations. The E-mode remains the same, but the B-mode changes sign which is analogous to the electric and magnetic fields respectively, [46].

3.4.2 Temperature Gradients

The gradients are spin-1 vectors, and make up a spin-1 field. The spin spherical harmonics must therefore be used when expanding the gradients in harmonic space. The gradients have two components, a derivative with respect to θ and a derivative with respect to ϕ, as given by Eq.(3.7). This results in two modes, one positive and one negative (the analogue of the E- and B-modes of polarization). Now these derivatives have to satisfy Eq.(3.16). Thus we get

$$\frac{\partial T}{\partial \theta} + \frac{i}{\sin\theta}\frac{\partial T}{\partial \phi} = \sum_{lm} {}_1a_{lm1}Y_{lm}, \tag{3.25}$$

and

$$\frac{\partial T}{\partial \theta} - \frac{i}{\sin\theta}\frac{\partial T}{\partial \phi} = \sum_{lm} {}_{-1}a_{lm-1}Y_{lm}. \tag{3.26}$$

With the expansion coefficients we can now make linear combinations of these, Eq.(3.17), such that we have the positive mode

$$a^+_{lm} = -\frac{1}{2}({}_1a_{lm} + {}_{-1}a_{lm}), \tag{3.27}$$

and the negative mode

$$a^-_{lm} = \frac{i}{2}({}_1a_{lm} - {}_{-1}a_{lm}). \tag{3.28}$$

These expressions are rotationally invariant. From these coefficients the power spectrum can be found, which is given by

$$C^+_l = \frac{1}{2l+1}\sum_m \langle a^+_{lm} a^{+*}_{lm}\rangle \tag{3.29}$$

for the positive mode. It is also possible to find the power spectrum of the negative mode.

Chapter 4

The MASTER algorithm

As we now have expressions for the temperature gradients it is of interest to look at their power spectra as this might give further information about the CMB. These can also be used for consistency checks and perhaps also to look for point sources in the data. When using the formalism in chapter 3 to find the power spectra from the data we will get the pseudo-power spectra. These power spectra will contain noise, instrumental beam and any mask applied to the data to remove foregrounds. In order to estimate the true power spectra, which does not contain any of these contributions, from the pseudo-power spectra, we can use the MASTER algorithm. The MASTER algorithm is the Monte Carlo Apodized Spherical Transform Estimator, described by Hivon et al.[26], and it can be used to estimate the power spectra from a temperature map, a polarization map or a gradient map.

4.1 The Temperature Power Spectrum

The CMB data can be modelled as a signal, s, times an instrumental beam, A, plus the pixel noise, n, that is

$$d = As + n. \tag{4.1}$$

There will also be a mask or other cut which removes any foreground contamination in the map by setting these regions to zero. In order to estimate the power spectrum, from the pseudo-power spectrum, this noise, instrumental beam, and mask must be compensated for. Whereas compensating for the noise or instrumental beam is straightforward, an expression for the effect of the mask has to be derived. This expression is the mode-mode coupling kernel, $M_{l_1 l_2}$.

From Eqs.(3.1) and (3.2) we know that the temperature can be expanded using spherical harmonics. The mask is characterized by a window function $W(\hat{n})$ so that we get the pseudo $\tilde{a}_{lm}$'s as

$$\tilde{a}_{lm} = \int d\hat{n} W(\hat{n}) T(\hat{n}) Y^*_{lm}. \tag{4.2}$$

Using Eq.(3.1) we can rewrite Eq.(4.2) so that we have

$$\tilde{a}_{lm} = a_{l'm'} \int Y_{l'm'} W(\hat{n}) Y^*_{lm}. \tag{4.3}$$

It is the integral in this equation which describes the effect of the mask, and thus what we want an expression for. We therefore pull this out and define

$$K_{l'm'lm} = \int Y_{l'm'} W(\hat{n}) Y^*_{lm} d\hat{n}. \tag{4.4}$$

We now need the expansion coefficients for the window function

$$W(\hat{n}) = \sum w_{lm} Y_{lm}. \tag{4.5}$$

Substituting this into Eq.(4.4), and changing the indices such that $l'm' = l_1 m_1$, $lm = l_2 m_2$, we get

$$K_{l_1 m_1 l_2 m_2} = \sum_{l_3 m_3} w_{l_3 m_3} \int Y_{l_1 m_1} Y_{l_3 m_3} Y^*_{l_2 m_2} d\hat{n} \tag{4.6}$$

Now we can use the Wigner 3j symbols and the relation

$$\begin{aligned} \int Y_{l_1 m_1} Y_{l_3 m_3} Y_{l_2 m_2} d\hat{n} = \sqrt{\frac{(2l_1+1)(2l_2+1)(2l_3+1)}{4\pi}} \\ \times \begin{pmatrix} l_1 & l_2 & l_3 \\ m_1 & m_2 & m_3 \end{pmatrix} \begin{pmatrix} l_1 & l_2 & l_3 \\ 0 & 0 & 0 \end{pmatrix} \end{aligned} \tag{4.7}$$

where the Wigner 3j symbols are given by

$$\begin{pmatrix} l_1 & l_2 & l_3 \\ m_1 & m_2 & m_3 \end{pmatrix} \tag{4.8}$$

where m_1, m_2 and m_3 are zero for spin 0. Using this relation between the spherical harmonic functions and the Wigner 3j symbols, and that $Y^*_{lm} = (-1)^m Y_{l-m}$, we get

$$\begin{aligned} K_{l_1 m_1 l_2 m_2} = \sum_{l_3 m_3} w_{l_3 m_3} (-1)^{m_2} \sqrt{\frac{(2l_1+1)(2l_2+1)(2l_3+1)}{4\pi}} \\ \times \begin{pmatrix} l_1 & l_2 & l_3 \\ 0 & 0 & 0 \end{pmatrix} \begin{pmatrix} l_1 & l_2 & l_3 \\ m_1 & m_2 & -m_3 \end{pmatrix}. \end{aligned} \tag{4.9}$$

With this expression for $K_{l_1 m_1 l_2 m_2}$ we now find the power spectrum, that is

$$\begin{aligned} \langle \tilde{C}_l \rangle &= \frac{1}{2l_1+1} \sum_{m_1=-l_1}^{l_1} \langle \tilde{a}_{lm} \tilde{a}^*_{lm} \rangle \\ &= \frac{1}{2l_1+1} \sum_{m_1=-l_1}^{l_1} \sum_{l_2 m_2} \langle a_{lm} a^*_{lm} \rangle K_{l_1 m_1 l_2 m_2} K^*_{l_1 m_1 l_2 m_2} \\ &= \frac{1}{2l_1+1} \sum_{m_1=-l_1}^{l_1} \sum_{l_2} \langle C_{l_2} \rangle \sum_{m_2=-l_2} |K_{l_1 m_1 l_2 m_2}|^2. \end{aligned}$$

We then get, for $|K_{l_1m_1l_2m_2}|^2$, that

$$|K_{l_1m_1l_2m_2}|^2 = \sum_{l_3m_3}\sum_{l_4m_4} w_{l_3m_3}w_{l_4m_4}\sqrt{[(2l_3+1)(2l_4+1)]}$$
$$\times \begin{pmatrix} l_1 & l_2 & l_3 \\ 0 & 0 & 0 \end{pmatrix}\begin{pmatrix} l_1 & l_2 & l_3 \\ 0 & 0 & 0 \end{pmatrix}\sum_{m_1m_2}\begin{pmatrix} l_1 & l_2 & l_3 \\ m_1 & m_2 & -m_3 \end{pmatrix}\begin{pmatrix} l_1 & l_2 & l_3 \\ m_1 & m_2 & -m_3 \end{pmatrix} \quad (4.10)$$

Now the orthogonality relation for the Wigner 3j symbols,

$$\sum_{m_1m_2}\begin{pmatrix} l_1 & l_2 & l_3 \\ m_1 & m_2 & m_3 \end{pmatrix}\begin{pmatrix} l_1 & l_2 & L_3 \\ m_1 & m_2 & M_3 \end{pmatrix} = (2l_3+1)^{-1}\delta_{l_2L_3}\delta_{m_3M_3}, \quad (4.11)$$

can be used. This means that Eq.(4.10) cancel down to give the mode-mode coupling kernel, $M_{l_1l_2}$, which is

$$M_{l_1l_2} = \frac{2l_2+1}{4\pi}\sum_{l_3}(2l_3+1)W_{l_3}\begin{pmatrix} l_1 & l_2 & l_3 \\ 0 & 0 & 0 \end{pmatrix}^2, \quad (4.12)$$

since

$$W_l = \frac{1}{2l+1}\sum_{lm} w_{lm}w^*_{lm} \quad (4.13)$$

is the power spectrum of the window function. This describes the effect of a window function on the power spectrum and its correlation. The pseudo-power spectrum is therefore given by

$$\langle\tilde{C_{l_1}}\rangle = \sum_{l_2} M_{l_1l_2}B^2_{l_2}\langle C_{l_2}\rangle + \langle\tilde{N_{l_2}}\rangle \quad (4.14)$$

where $\tilde{N}_{l'}$ is the noise power spectrum, and $B_{l'}$ describes the combined smoothing effect of finite pixel size and the instrumental beam. The noise power spectrum can be found from Monte Carlo simulations, see chapter 6 and 8. So to estimate the power spectrum from the pseudo-power spectrum we use

$$\langle C_{l_1}\rangle = \sum_{l_2} M^{-1}_{l_1l_2}B^{-2}_{l_2}(\langle\tilde{C_{l_2}}\rangle - \langle\tilde{N_{l_2}}\rangle). \quad (4.15)$$

It is useful to bin the power spectrum in l to avoid correlations between the C_l's. We therefore introduce two binning operators P_{bl} and Q_{lb} given by

$$P_{bl}\begin{cases} \frac{1}{2\pi}\frac{l(l+1)}{l^{(b+1)}_{\rm low}-l^{(b)}_{\rm low}} & \text{if} \quad 2 \le \mathrm{l}^{(\mathrm{b})}_{\rm low} \le \mathrm{l} < \mathrm{l}^{(\mathrm{b+1})}_{\rm low}, \\ 0 \end{cases} \quad (4.16)$$

and

$$Q_{lb}\begin{cases} \frac{2\pi}{l(l+1)} & \text{if} \quad 2 \le \mathrm{l}^{(\mathrm{b})}_{\rm low} \le \mathrm{l} < \mathrm{l}^{(\mathrm{b+1})}_{\rm low}. \\ 0 \end{cases} \quad (4.17)$$

Using these gives

$$\hat{C}_b = K^{-1}_{bb'}P_{bl'}(\tilde{C}_l - N_l) \quad (4.18)$$

for the binned power spectrum. Here $K_{bb'}$ is just the binned version of $M_{l_1l_2}$ with the beam function B_{l_2} included. See also [21] and [43] for estimation of the temperature power spectrum.

4.2 The Power Spectrum for non-zero Spin

For the non-zero spin fields, like polarization and the gradients, we have the same data model as in Eq.(4.1), and need to compensate for the same effects as in the temperature case. The derivation of the mode-mode coupling kernel for the non-zero spin fields is similar to that of temperature, but instead we have spin-s spherical harmonic functions. This derivation will now be done generally for any spin-s field. Here the absolute value of the spin, $|s|$, has been used in order make it clear which spin, positive or negative, which is used.

Firstly we need to know what the spin-s spherical harmonics are given by, that is

$$ {}_sY_{lm}(\theta,\phi) = \sqrt{\frac{2l+1}{4\pi}} D^l_{-sm}(\phi,\theta,0) \tag{4.19} $$

where $D^l_{-sm}(\phi_2,\theta,\phi_1)$ is a rotation matrix. We will now define two functions, ${}_{|s|}G$ and ${}_{-|s|}G$, which has a definite value of spin, and has to transform according to Eq.(3.16). As for the coupling kernel for temperature we start with the the functions ${}_{\pm|s|}G$ expanded with spin-s spherical harmonics. Thus we have

$$ {}_{\pm|s|}G = \sum_{lm} {}_{\pm|s|}a_{lm\pm|s|}Y_{lm}, \tag{4.20} $$

or

$$ {}_{\pm|s|}a_{lm} = \int d\hat{n}_{\pm|s|}Y^*_{lm\pm|s|}G. \tag{4.21} $$

For non-zero spin we have two modes

$$ {}_{|s|}a^+_{lm} = -\frac{1}{2}({}_{|s|}a_{lm} + {}_{-|s|}\,a_{lm}), \tag{4.22} $$

and

$$ {}_{|s|}a^-_{lm} = \frac{i}{2}({}_{|s|}a_{lm} - {}_{-|s|}\,a_{lm}). \tag{4.23} $$

As for temperature we have a window function $W(\hat{n})$ which can be expanded in spherical harmonics, Eq.(4.5), and has a power spectrum as in Eq.(4.13). Now starting with the positive spin we have

$$ {}_{|s|}\tilde{a}_{lm} = \int d\hat{n}_{|s|}Y^*_{lm}W(\hat{n})_{|s|}G. \tag{4.24} $$

Using Eq.(4.20) we get

$$ {}_{|s|}\tilde{a}_{lm} = {}_{|s|}\,a_{l'm'} \int d\hat{n}_{|s|}Y^*_{lm|s|}Y_{l'm'}W(\hat{n}), \tag{4.25} $$

and substituting for the window function $W(\hat{n})$ using Eq.(4.5) gives

$$ {}_{|s|}\tilde{a}_{lm} = {}_{|s|}\,a_{l'm'} \sum_{l''m''} w_{l''m''} \int d\hat{n}_{|s|}Y^*_{lm|s|}Y_{l'm'}Y_{l''m''}. \tag{4.26} $$

Again we pull out the window function and the spherical harmonic functions as this is what we are interested in, so

$$ {}_{|s|}K_{lml'm'} = \sum_{l''m''} w_{l''m''} \int d\hat{n}\, {}_{|s|}Y^*_{lm|s|} Y_{l'm'} Y_{l''m''}. \tag{4.27}$$

Before we proceed we need some more relations for the spherical harmonic functions. First of all we need to know what the complex conjugate of a spin-s spherical harmonic function is, namely

$$ {}_{|s|}Y^*_{lm} = {}_{-|s|}\, Y_{l-m}(-1)^{m+s}. \tag{4.28}$$

We also need the relation between the Wigner 3j symbols and the rotation matrices given by

$$\begin{aligned} &\frac{1}{8\pi^2} \int d(cos(\theta)) d\phi d\gamma D^l_{m1m1'} D^{l'}_{m2m2'} D^{l''}_{m3m3'} \\ &\quad = \begin{pmatrix} l & l' & l'' \\ m_1 & m_2 & m_3 \end{pmatrix} \begin{pmatrix} l & l' & l'' \\ m'_1 & m'_2 & m'_3 \end{pmatrix}. \end{aligned} \tag{4.29}$$

Now using the relation between the spherical harmonic function and the rotation matrices, Eq.(4.19), the above relations, Eqs.(4.28) and (4.29), and substituting for the spherical harmonics in Eq.(4.27) we get

$$\begin{aligned} {}_{|s|}K_{lml'm'} = \frac{8\pi^2}{2\pi}(-1)^{m+|s|} \sum_{l''m''} w_{l''m''} \sqrt{\frac{(2l+1)(2l'+1)(2l''+1)}{(4\pi)^3}} \\ \times \begin{pmatrix} l & l' & l'' \\ -|s| & |s| & 0 \end{pmatrix} \begin{pmatrix} l & l' & l'' \\ -m'_1 & m'_2 & m'_3 \end{pmatrix}. \end{aligned} \tag{4.30}$$

We now have for the positive spin

$$\begin{aligned} {}_{|s|}K_{lml'm'} = 4\pi(-1)^{m+|s|} \sum_{l''m''} w_{l''m''} \sqrt{\frac{(2l+1)(2l'+1)(2l''+1)}{(4\pi)^3}} \\ \times \begin{pmatrix} l & l' & l'' \\ -|s| & |s| & 0 \end{pmatrix} \begin{pmatrix} l & l' & l'' \\ -m'_1 & m'_2 & m'_3 \end{pmatrix}. \end{aligned} \tag{4.31}$$

For the negative spin component we have a very similar expression which can be derived in the same way,

$$\begin{aligned} {}_{-|s|}K_{lml'm'} = 4\pi(-1)^{m-|s|} \sum_{l''m''} w_{l''m''} \sqrt{\frac{(2l+1)(2l'+1)(2l''+1)}{(4\pi)^3}} \\ \times \begin{pmatrix} l & l' & l'' \\ |s| & -|s| & 0 \end{pmatrix} \begin{pmatrix} l & l' & l'' \\ -m'_1 & m'_2 & m'_3 \end{pmatrix}. \end{aligned} \tag{4.32}$$

However we can use the following relation for the Wigner 3j symbol

$$\begin{pmatrix} l & l' & l'' \\ |s| & -|s| & 0 \end{pmatrix} = (-1)^{l+l'+l''} \begin{pmatrix} l & l' & l'' \\ -|s| & |s| & 0 \end{pmatrix} \tag{4.33}$$

so that we have

$$ {}_{-|s|}K_{lml'm'} = 4\pi(-1)^{m-|s|}\sum_{l''m''} w_{l''m''}\sqrt{\frac{(2l+1)(2l'+1)(2l''+1)}{(4\pi)^3}} \times \begin{pmatrix} l & l' & l'' \\ -|s| & |s| & 0 \end{pmatrix}\begin{pmatrix} l & l' & l'' \\ -m'_1 & m'_2 & m'_3 \end{pmatrix}(-1)^{l+l'+l''}. \quad (4.34) $$

As ${}_{|s|}K_{lml'm'}$ and ${}_{-|s|}K_{lml'm'}$ do not have a symmetry we can construct a coupling kernel that has an m symmetry from theses two, similarly to that done with the spin-s a_{lm}. So we have

$$ H_{|s|} = \frac{1}{2}({}_{|s|}K + {}_{-|s|}K) \quad (4.35) $$

and

$$ H_{-|s|} = \frac{1}{2}({}_{|s|}K - {}_{-|s|}K). \quad (4.36) $$

We now want the power spectrum from Eq.(4.22), or Eq.(4.23), depending on the mode of interest. So we get, using Eq.(3.5),

$$ \begin{aligned} \tilde{C}_l &= \frac{1}{2l+1}\sum_{l'm'} |a^+_{l'm'}|^2 H^2_{|s|} \\ &= \frac{1}{2l+1}\sum_{m} |{}_{|s|}a^+_{lm}|^2({}_{|s|}K^2 + {}_{|s|}K_{-|s|}K)/2. \end{aligned} $$

This then gives

$$ \tilde{C}_l = \frac{1}{2l+1}\sum_{l'l''} C_{l'}\frac{1}{2}\frac{1}{2l''+1}W_{l''}\frac{(2l+1)(2l'+1)(2l''+1)}{(4\pi)^3}(4\pi)^2 \times \begin{pmatrix} l & l' & l'' \\ -|s| & |s| & 0 \end{pmatrix}^2 [1+(-1)^{l+l'+l''}]. $$

From this the mode-mode coupling kernel for the positive mode becomes

$$ M_{|s|,lml'm'} = \sum_{l''} W_{l''}\frac{(2l'+1)(2l''+1)}{(8\pi)} \times \begin{pmatrix} l & l' & l'' \\ -|s| & |s| & 0 \end{pmatrix}^2 [1+(-1)^{l+l'+l''}] $$

using the relation

$$ \sum_{mm'} \begin{pmatrix} l & l' & l'' \\ m & m' & m'' \end{pmatrix}\begin{pmatrix} l & l' & L'' \\ m' & m' & M'' \end{pmatrix} = (2l''+1)^{-1}\delta_{l''L''}\delta_{m''M''}. $$

For the negative mode we have similarly

$$ M_{-|s|,lml'm'} = \sum_{l''} W_{l''}\frac{(2l'+1)(2l''+1)}{(8\pi)} \times \begin{pmatrix} l & l' & l'' \\ -|s| & |s| & 0 \end{pmatrix}^2 [1-(-1)^{l+l'+l''}]. $$

Gathering these two expressions into one expression, and changing the labeling so that $lm = l_1m_1$, $l'm' = l_2m_2$ and $l''m'' = l_3m_3$ we get

$$M_{\pm|s|,l_1l_2} = \frac{2l_2+1}{8\pi}\sum_{l_3}(2l_3+1)W_{l_3}\begin{pmatrix} l_1 & l_2 & l_3 \\ -|s| & |s| & 0 \end{pmatrix}^2 \times [1 \pm (-1)^{l_1+l_2+l_3}], \quad (4.37)$$

as the final expression for the mode-mode coupling kernel for the estimation of the power spectra of a non-zero spin field.

4.2.1 The Polarization Power Spectra

In the case of the polarization power spectra we have that the pseudo-power spectra are given by

$$\begin{pmatrix} \langle \tilde{C}_l^{EE} \rangle \\ \langle \tilde{C}_l^{BB} \rangle \end{pmatrix} = \begin{pmatrix} K_{ll'}^{+} & K_{ll'}^{-} \\ K_{ll'}^{-} & K_{ll'}^{+} \end{pmatrix} \begin{pmatrix} \langle C_l^{EE} \rangle \\ \langle C_l^{BB} \rangle \end{pmatrix} + \begin{pmatrix} \tilde{N}_l^{EE} \\ \tilde{N}_l^{BB} \end{pmatrix}. \quad (4.38)$$

Here $\tilde{N}_l^{BB}$ and $\tilde{N}_l^{EE}$ are the noise power spectra for the B-mode and the E-mode polarization respectively. $K_{ll'}^{\pm}$ is the mode-mode coupling kernel with the the function $B_{l'}$, of the instrumental beam and finite pixel size, included. In order to get the estimated C_l's from the data we need to take the inverse of this giving

$$\begin{pmatrix} \langle C_l^{EE} \rangle \\ \langle C_l^{BB} \rangle \end{pmatrix} = \begin{pmatrix} K_{ll'}^{+} & K_{ll'}^{-} \\ K_{ll'}^{-} & K_{ll'}^{+} \end{pmatrix}^{-1} \begin{pmatrix} \langle \tilde{C}_l^{EE} \rangle - \tilde{N}_l^{EE} \\ \langle \tilde{C}_l^{BB} \rangle - \tilde{N}_l^{BB} \end{pmatrix}. \quad (4.39)$$

Thus the coupling kernel is a $2l_{max}$-by-$2l_{lmax}$ matrix. From the derivation of the mode-mode coupling kernel for a spin-s field the polarization mode-mode coupling kernel is given by

$$M_{\pm 2,l_1l_2} = \frac{2l_2+1}{8\pi^2}\sum_{l_3} W_{l_3}(2l_3+1)\begin{pmatrix} l_1 & l_2 & l_3 \\ -2 & 2 & 0 \end{pmatrix}^2 \times [1 \pm (-1)^{l_1+l_2+l_3}], \quad (4.40)$$

so that

$$K_{ll'}^{\pm} = M_{\pm 2,ll'}B_{l'}.$$

Since the coupling kernel mixes the two modes the B-mode power spectrum will contain a contribution from the E-mode, and visa versa, when attempting to use these equations. As the E-mode is a lot stronger than the B-mode it will be difficult to get any of the B-mode from the data. However, Smith,[41], has proposed a method to remove any contribution from the E-mode. This gives a more complicated coupling kernel for the B-mode. There is also a contribution from the B-mode in the E-mode, but since the E-mode is a lot stronger it is not noticeable. See also [22] for estimation of the polarization power spectra.

4.2.2 The Gradient Power Spectrum

As the gradients are spin-1 vectors we get two components, or modes, and therefore two power spectra. So Eq.(4.38), and Eq.(4.39), can be used for the gradients as well, so that

$$\begin{pmatrix} \langle C_l^+ \rangle \\ \langle C_l^- \rangle \end{pmatrix} = \begin{pmatrix} K_{ll'}^+ & K_{ll'}^- \\ K_{ll'}^- & K_{ll'}^+ \end{pmatrix}^{-1} \begin{pmatrix} \langle \tilde{C_l}^+ \rangle - \tilde{N_l}^+ \\ \langle \tilde{C_l}^- \rangle - \tilde{N_l}^- \end{pmatrix} \tag{4.41}$$

Here B_l is part of $K_{ll}^{\pm}$, and $\tilde{N_l}^{\pm}$ the noise gradient power spectra for the positive and negative modes. We also get the mode-mode coupling kernel as

$$M_{\pm 1,l_1l_2} = \frac{2l_2+1}{8\pi} \sum_{l_3} (2l_3+1) W_{l_3} \begin{pmatrix} l_1 & l_2 & l_3 \\ -1 & 1 & 0 \end{pmatrix}^2 \times [1 \pm (-1)^{l_1+l_2+l_3}], \tag{4.42}$$

so that

$$K_{ll'}^{\pm} = M_{\pm 1,ll'} B_{l'}.$$

This is exactly the same approach as for the mode-mode coupling kernel for polarization. In the same way as for polarization there will be a mixing of the two modes. But also here the positive mode is a lot stronger than the negative mode, and so does not contribute noticeably to the power spectrum of the positive mode, see section 11.1.

Chapter 5

Statistics

We have now found convenient expressions for the gradients in chapter 3, and a way to estimate the gradient power spectrum in chapter 4. We will now look at some statistics that will be used to look for anomalies in the CMB. One of these statistical tests is the preferred direction statistic. In general we will test whether the gradients from the WMAP data come from the same distribution as the gradients of a simulated Gaussian temperature map.

5.1 A Preferred Direction Statistic

One statistic that has been investigated is the preferred direction statistic proposed by Bunn and Scott in 2000[8]. They applied it to the COBE data, and later Hanson et al.[23] have used it to look for further foreground contamination in foreground cleaned CMB polarization maps. Here it has been applied to the seven year WMAP temperature data. In order to calculate the statistic we use the formalism in section 3.3 to find the gradients of the temperature map. These can then be used to evaluate the dot-product of gradients and unit vectors on the sphere. Thus we have a function, which will be referred to as the direction function, given by

$$f(\hat{n}) = \sum_{i=0}^{N_{\rm pix}-1} (\nabla T(\theta,\phi)_i \cdot \hat{n})^2. \tag{5.1}$$

This function can be used to look for anomalies by treating its maximum and minimum values as two separate statistics. The maximum and minimum of this function are also compared to give the preferred direction statistic, as presented by Bunn and Scott,

$$\mathcal{D} = \frac{\max(f(\hat{n}))}{\min(f(\hat{n}))}. \tag{5.2}$$

This is a statistic that can find a preferred direction in the CMB, or assess the level of "preferred directionality" as the dot-product tells us how much two vectors align. The statistic reveals a preferred direction by giving either anomalously small or anomalously

larges values of $\mathcal{D}$. It can be either a direction which the gradients align with or avoid. The only difference from Bunn and Scott's approach is the calculation of the gradients which here are found in harmonic space.

5.2 Other Statistical Tests

We would also like to test if the gradients found from the WMAP temperature map come from the same distribution as the gradients from simulated temperature maps. This can be achieved by using either the χ^2-test or the Kolmogorov-Smirnov test, [2]. Using these we can find out if the simulated maps are reasonable or not when comparing with the WMAP data.

5.2.1 The χ^2 - test

The χ^2-test is a test for the goodness of fit of a sample to a given distribution. The values in the sample are compared to the mean of the test distribution, from which the χ^2-test can determine whether the sample differs significantly from the test distribution or not. The χ^2 test is defined as

$$\chi^2 = (C - \mu)^T V^{-1} (C - \mu) \tag{5.3}$$

where C is a given measurement. The average, μ, is given by

$$\mu = \frac{1}{N} \sum_i C_i \tag{5.4}$$

where N is the number of measurements. V^{-1} is the inverse of the covariance matrix given by

$$V_{ij} = \langle (C_i - \mu_i)(C_j - \mu_j) \rangle. \tag{5.5}$$

Here the distribution of the sample and the test distribution has been divided into M intervals, and the mean, μ, of each interval has been calculated for the test distribution. The values from the sample in each interval are then compared to the mean of each interval from the test distribution.

The above equation for χ^2 can also be simplified to give

$$\chi^2 = \sum_i \frac{(C_i - \mu)^2}{\sigma^2} \tag{5.6}$$

if the data points are uncorrelated. The variance, σ^2, is given by

$$\sigma^2 = \frac{1}{N}(\langle C_i^2 \rangle - \langle C_i \rangle^2) = \frac{1}{N} \sum_i (C_i - \mu)^2. \tag{5.7}$$

In the simplest cases of the χ^2-test the result is expected to be close to zero when the sample comes from the test distribution. When the test distribution is divided into intervals, as above, χ^2 is expected to be close to the number of intervals M, if the sample comes from the test distribution. The test distribution can be found from samples from simulations.

5.2.2 The Kolmogorov-Smirnov test

The Kolmogorov-Smirnov test can determine if the sampled data comes from a given distribution, or whether two samples come from the same distribution or not. We will here look at the second case. To apply this test we need to find the probability functions of the samples. With this function we can now integrate to get the corresponding cumulative distribution function $F_n(x)$. $F_n(x)$ is a step function increasing from zero to one.

We can now do this for both of the samples of interest, so that we have the cumulative distribution functions $F_n(x)$ for sample one, and $F_m(x)$ for sample two. The statistic given by the Kolmogorov-Smirnov test is called the D-statistic and is defined as

$$D = \max(F_n(x) - F_m(x)). \tag{5.8}$$

This statistic looks at the difference between the two distribution functions $F_n(x)$ and $F_m(x)$. If the difference between the distribution functions is large, i.e. large values of D, then they are not from the same distribution. We can therefore look at the maximum difference between the distribution functions and use this to determine whether they are from the same distribution or not. We can also find the probability for a given result of this test

$$Pr(K \leq x) = \frac{\sqrt{2\pi}}{x} \sum_{i=1} e^{-(2i-1)^2\pi^2/(8x^2)}. \tag{5.9}$$

For the two sample test we have that

$$K < D_{nm}\sqrt{\frac{nm}{n+m}}. \tag{5.10}$$

If the value of $Pr(K \leq x)$ is large we can accept the results from the D-statistic, and thus learn whether the samples are from the same distribution or not.

Fig.5.1 shows the principle of the Kolmogorov-Smirnov test for two distributions. The largest difference between these distributions is marked by a line, and its value, in this case, is $D = 2.9 \times 10^{-2}$.

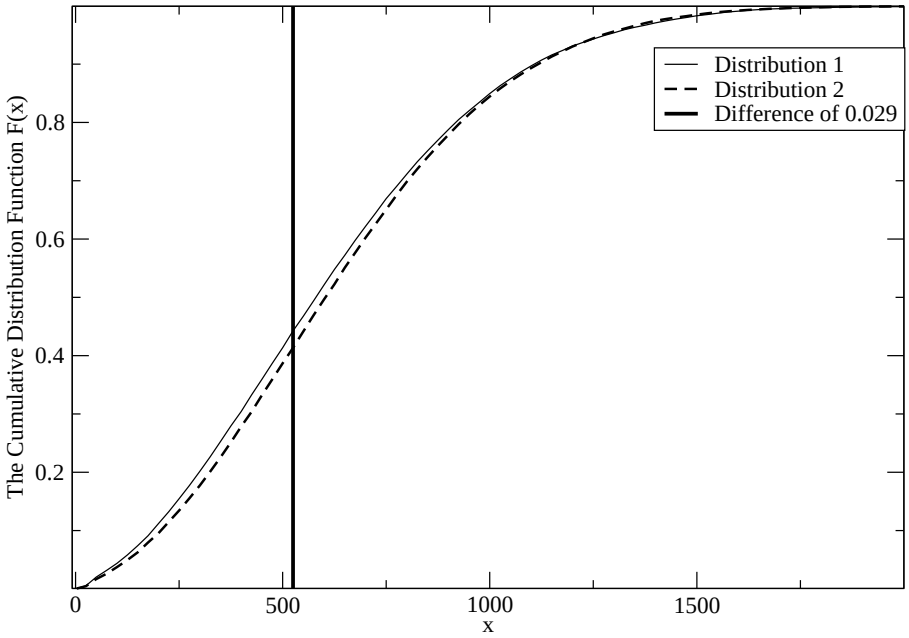

Figure 5.1: The cumulative distribution functions of two distributions for the Kolmogorov-Smirnov test. The line shows the D-statistic of this test. This is the maximum difference between the two distributions, with $D = 2.9 \times 10^{-2}$ here.

Part II

Method

Chapter 6

Data Analysis

Having defined the statistical tests we wish to apply to the data, we will now review the method for creating simulations, to compare with the real data from WMAP, and the steps used to analyse these maps when applying the statistical tests. We will also look at the template for analyzing the northern and southern hemispheres individually. This is of interest due to the reported detections of the asymmetry in the CMB.

6.1 WMAP Specifics

The WMAP satellite has five different frequency bands, these are K, Ka, Q, V and W. The typical frequencies for these bands can be found in Table 6.1. The pixel noise, in mK, for each frequency can also be found in this table and a plot of this noise for V1-channel can be seen in Fig.6.2.

The Q- and V-bands have two different channels each, while W-band has four. K-band is the most foreground contaminated map, and it has been used by the WMAP team to make foreground templates. These again have been used to reduce the foregrounds in the sky maps for the other frequency bands, [6]. W-band has the least foreground contamination, but has more correlated noise.

The instrumental beams also differ from frequency to frequency and between the different channels. These instrumental beam profiles for the different channels can be seen in Fig.6.1. We will need the information about the beam profiles and the noise properties of each of the channels when creating simulations with the same properties as the WMAP data.

6.2 Creating Simulations of CMB Temperature Maps

The simulations of the temperature anisotropies is based on the ΛCDM model best-fit power spectrum to the WMAP data. This is then used to generate the a_{lm} coefficients, which is done by using the relation

$$a_{lm} = \sqrt{\frac{C_l}{2}} \times (\eta_1 + i\eta_2) \tag{6.1}$$

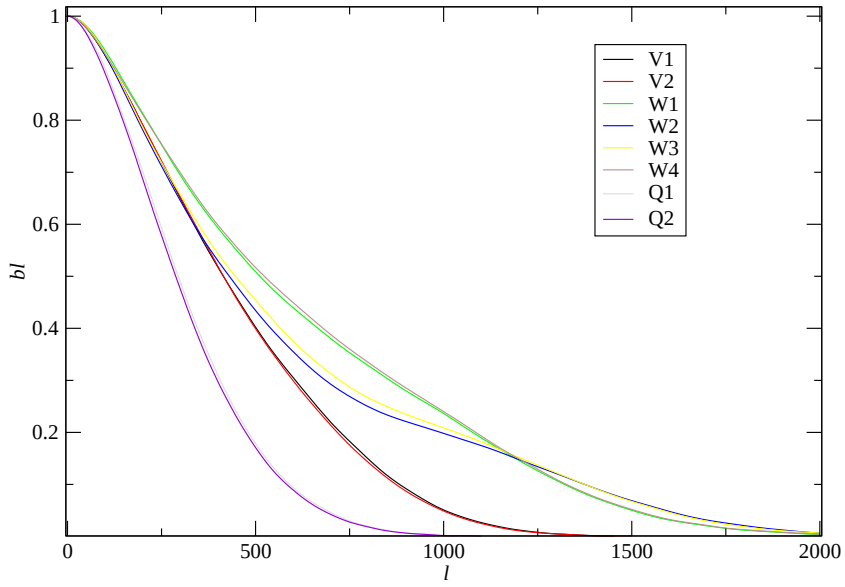

Figure 6.1: Different beam profiles for all the channels of each frequency band for the WMAP satellite used to smoothed simulated CMB sky maps in Eq.(6.3).

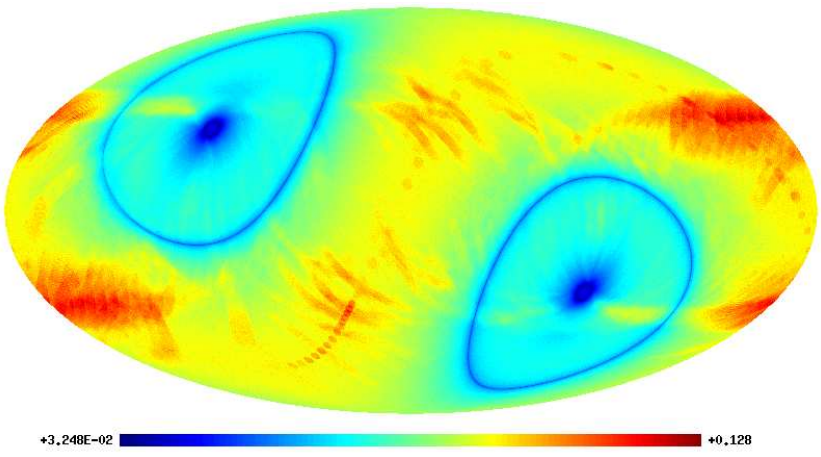

Figure 6.2: Map of the pixel noise for the V1-band. This is the map created from Eq.(6.4), and which is multiplied with random numbers from a Gaussian distribution.

Band	Frequency (GHz)	σ_0 (mK)
K	23	1.437
Ka	33	1.470
Q	41	2.197
V	61	3.137
W	94	6.549

Table 6.1: Typical frequencies for each band in GHz for the WMAP satellite, as well as pixel noise in mK. This pixel noise is used when adding noise to simulated CMB sky maps when looking at each frequency band. The noise is for temperature maps only.

where η_1 and η_2 are random numbers generated from a Gaussian probability distribution. The square root of two comes from the fact that we have $-m < l < m$, and that $a_{lm} = a_{l-m}$. However, there is one special case which has to be treated separately. When $m = 0$ the a_{lm}'s are real numbers, not complex, so that we get

$$a_{lm} = \sqrt{C_l} \times \eta_1. \tag{6.2}$$

There is also no division by two as there is only one a_{lm} for $m = 0$. This can be coded using the HEALPix routine rand_init to generate random numbers from a Gaussian distribution,[19] and using Eqs.(6.7) and (6.2) so that we have

```
call rand_init(rng_handle,12345+2563)

! Generate alms from the cls using the random numbers
do l = 0, lmax
    do m = 0, l

       eta = rand_gauss(rng_handle)

        if(m==0) then
             alm(1,l,m) = sqrt(cl(l))*eta
        else
             eta2 = rand_gauss(rng_handle)

             alm(1,l,m) = sqrt(cl(l)/2.0d0)*cmplx(eta,eta2)
        endif

    enddo
enddo
```

The data model, given by Eq.(4.1), includes an instrumental beam and noise. So the next step is to add the smoothing effect of finite pixel size, using the pixel window function, and the instrumental beam. The instrumental beam is the WMAP instrumental beam corresponding to the frequency or channel of interest, and the window function

depends on $N_{\rm side}$ of the map, i.e. pixel size. We therefore have

$$a_{lm} = a_{lm} b_l(\text{WMAP}) p_l^{\rm N_{side}} \tag{6.3}$$

where b_l(WMAP) is the WMAP instrumental beam, and $p_l^{N_{\rm side}}$ is the pixel window function. These a_{lm}'s can now be used to generate a map using the HEALPix routine alm2map which converts from harmonic space to pixel space.

With this temperature map the last thing that needs to be added is noise. The noise can be evaluated from the pixel noise, σ_0[1], as tabulated by the WMAP team, see Table 6.1, and by the number of times each pixel has been observed, $N_{\rm obs}$[2], that is

$$\sigma = \frac{\sigma_0}{\sqrt{N_{\rm obs}}}. \tag{6.4}$$

This was then added to the map multiplied by a random number from a Gaussian distribution, using a random number generator, for each pixel. When evaluating the statistical tests 1000 simulated sky maps were made using Monte Carlo cycles.

6.3 Analysing Temperature Maps for Apply the Statistical Tests

When simulated maps have been made, as in section 6.2, the rest of the analysis is the same for these maps and the WMAP sky maps. All these maps have been analysed in μK. We will also be testing template corrected maps where the templates have been applied to the simulated maps. These templates are presented in chapter 7. Before applying the preferred direction statistic, or finding the gradients and direction function, we will need to add a mask and we will also change the beam.

First we will apply a mask to remove foreground contamination from dust, free-free emission and synchrotron radiation by setting pixels with this contamination to zero, [6]. The largest contaminant is our own galaxy. This foreground contamination has been reduced by the WMAP team, but a mask is still required. This mask can be seen in Fig.6.3.

Here the mask has been applied before the map is smoothed with the new beam. This means that the mask will get smoothed with the map so that there will not be a sharp edge between the mask and the map when finding the gradients. This reduces the ringing in the gradient map. It is important to note that the point source mask has been removed from the mask so that the parts masking the point sources does not get smoothed out. When the point source mask has been removed the mask has also been smoothed with a beam of $40'$ before being applied to the map. A lager mask ensures that all the foreground contamination has been removed. To smooth the mask it is converted to a_{lm}'s, using the HEALPix routine map2alm, and then smoothed with the beam function so that

$$a_{lm}^{\rm smooth} = a_{lm} b_l. \tag{6.5}$$

[1] see http://lambda.gsfc.nasa.gov/

[2] This information is given in the WMAP data files for each frequency band

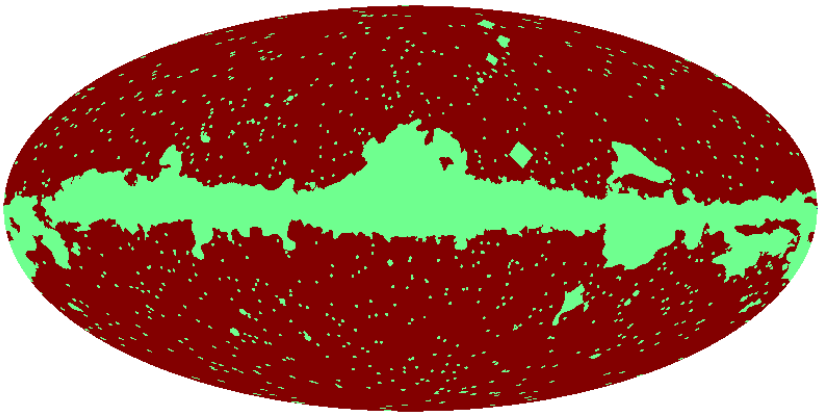

Figure 6.3: Temperature analysis mask used to remove foreground contamination and point sources in the WMAP data. This is the KQ85 mask (and can be found on the LAMBDA webpage).

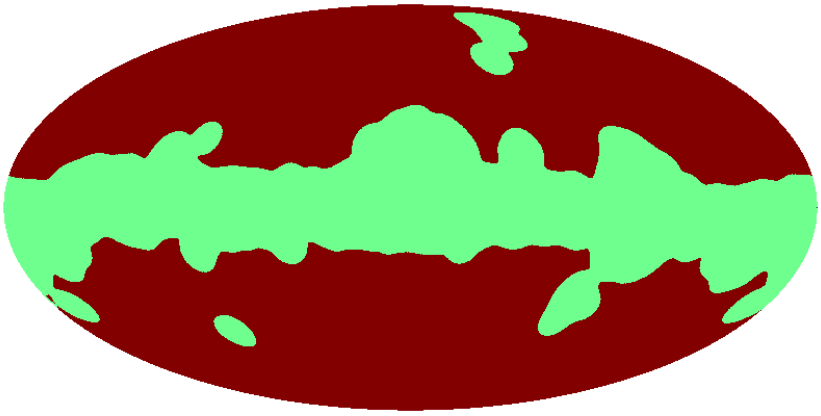

Figure 6.4: Smoothed temperature analysis mask used to remove border effects after the gradients have been found from a smoothed temperature map. This is the KQ85 mask with the point source mask removed, and smoothed with a beam of 6°.

This Gaussian beam is given by

$$b_l = e^{-\frac{1}{2}l(l+1)(\frac{\theta(\mathrm{FWHM})\pi}{180\times 60}\frac{1}{\sqrt{8ln(2)}})^2}. \tag{6.6}$$

A beam of $40'$ for smoothing the mask is sufficient when the mask gets smoothed out with the map. If this is not the case, the mask should not be smoothed with a beam smaller than $50'$ after removing the point source mask. The reason is that any less smoothing leaves holes in the mask which will contaminate the results.

When the mask has been smoothed, it is converted back to pixel space using the

HEALPix routine alm2map. Then all pixels with values larger than a given threshold, here 0.99, are set to one, and are not part of the mask. This mask is then multiplied into the map.

With the mask applied to the data the map can be deconvolved with a new beam and the new desired resolution using the pixel window functions. The original instrumental beam is also removed from the data so that we get the new a_{lm}'s, a_{lm}^{NEW}, given by

$$a_{lm}^{\mathrm{NEW}} = a_{lm} \frac{b_{l(\mathrm{new})} p_{l(N_{\mathrm{side}}\mathrm{new})}}{b_{l(\mathrm{old})} p_{l(N_{\mathrm{side}}\mathrm{old})}}. \tag{6.7}$$

The new beam is given by the Gaussian beam in Eq.(6.6). This smoothing is used to reduce the noise in the map and the effect of point sources.

It is from these maps, with a mask and a new beam, that the gradients are found. When applying Eq.(3.14) and Eq.(3.11) these equations will give the gradients in polar coordinates. In order to evaluate the preferred direction statistic the gradients must be converted to Cartesian coordinates. This was done by using Euler rotation matrices.

When the gradients have been found the same mask is applied to remove border effects between the mask and the map, but now it has been smoothed by 6°. The point source mask is removed, and the mask is treated the same way as the mask described above. This mask is then multiplied into the gradient map. The smoothed mask can be seen in Fig.6.4. Finally the point source mask can be added again if desired, but this has not been done here.

When using lower resolution maps the mask also has to be reduced to a lower resolution. This can be achieved by adding together the number of pixels required to make one new pixel in the new resolution. This can be easily done using the nested HEALPix scheme, [18], [19] . With the final mask in place, the next step is to find the preferred direction statistic or to look at the other statistical test.

When finding the direction function and the preferred direction statistic from the gradient map the sum in Eq.(5.1) is found for each unit vector on the sphere. This is done in pixel space, and the function will have the same amount of points as there are pixels in the map. Before the gradients are calculated from the temperature map, the map is smoothed with a beam of 4°. The resolution of the map is also set to $N_{\mathrm{side}} = 128$, so that there is $N_{\mathrm{pix}} = 12 \times N_{\mathrm{side}}^2 \approx 2 \times 10^5$ pixels in the temperature map. The reason for this choice of new beam was to have a beam which smooths out a lot of the noise, to get better signal to noise, and point sources so that these have a small, ideally no, effect on the results.

The choice of $N_{\mathrm{side}} = 128$ was due to the time required to calculate the statistic. The dot-product of the gradients and the unit vectors have been coded as given below. As this is done in pixel space we get a double loop over the number of pixels in the gradient map because we have N_{pix} gradients and N_{pix} unit vectors on the sphere. Thus the computation of the direction function given by Eq(5.1) takes $N(\mathcal{O}) \approx N_{\mathrm{pix}}^2$ operations which makes this very time consuming for high resolution gradient maps. For a map of close to a million pixels, or more, this summation will take a lot of time

for one map only. By choosing $N_{\text{side}} = 128$ it was possible to run 1000 Monte Carlo simulations in a few hours.

```
do i = 0, npix - 1
  do j = 0, npix - 1
     Cp(i) = Cp(i) + (((grad_xyz(j,1)*n_vec(1,i))&
                   + (grad_xyz(j,2)*n_vec(2,i))  &
                   + (grad_xyz(j,3)*n_vec(3,i)))**2)
  enddo
enddo
```

This smoothing and resolution have been used in all simulations, both with and without templates or for the other models, and on the WMAP data.

When testing the gradients distributions, of the simulated maps and the WMAP sky maps with the Kolmogorov-Smirnov test and χ^2-test, the same amount of smoothing and the same mask was used. When applying these tests the number of gradients in a given interval was counted to make a probability distribution of these. It was the total length of the gradients that was used in these tests, not the individual components in Cartesian coordinates, or polar coordinates.

The number of gradient outside the mask were counted, and saved, before the number of gradients in each interval was counted. The number in each interval was then divided by the total number of gradients to get the probability, this can be seen below. The distribution was divided into 100 intervals. In these two tests it was important that only the parts of the gradient maps outside the mask were taken into account. The masked area would only contribute with a large number of gradients that were zero, and would therefore introduce a peak in the distribution at zero.

```
mu = (max - min)/real(interval,dp)

do i = 0, interval
  do j = 1, count
    if((gradients(j) >= min + mu*real(i,dp)).and. &
      (gradients(j) < min + mu + mu*real(i,dp)))then
       counter(i) = counter(i) + 1
    endif
  enddo
  probability(i,k) = real(counter(i),dp)/(real(count,dp))
enddo
```

For the χ^2-test the mean of each interval for 500 simulations were found along with the standard deviation using Eqs.(5.6),(5.4) and (5.7). Using another 500 simulated maps χ^2 was calculated for each of these maps in order to make a distribution. Finally χ^2 for the WMAP data was calculated and compared to this distribution.

When using the covariance matrix, Eqs.(5.3) and (5.5), 800 simulations were used to find the mean of each interval and to build the covariance matrix. This was then

compared to 400 simulations to get a χ^2-distribution as in the case without the covariance matrix. Finally χ^2 was again calculated for the WMAP data and compared to this distribution.

In the Kolmogorov-Smirnov test the probability distributions were integrated to get the cumulative distributions functions. The probability distributions were integrated over intervals which meant that the values for each interval could be summed for each step. This was done for 500 simulations and for the WMAP data. The simulated cumulative distribution functions were then compared to the WMAP cumulative distribution function using Eq.(5.8). The probability for the results were also found by using Eq.(5.9). When finding the probability the expression was summed up to $i = 10^4$ in Eq.(5.9), and this was found to be sufficient to get a stable result.

6.4 The Northern and Southern Hemispheres

As there are several reports on an asymmetry in the northern and southern hemispheres it is of interest to find the direction function and preferred direction statistic for each of these separately. In Hoftuft et al.[27] it is found that a preferred direction points towards $(l, b) = (224^\circ, -22^\circ) \pm 24^\circ$. Using this as the centre of a circle of radius $\pi/2$ the template in Fig.6.5 can be made by setting one of the hemispheres to zero and the other to one. In order to make this template three HEALPix functions were used. These are ang2pix, which gives the pixel number for the angles $(l, b) = (\phi, \theta)$, and pix2vec, which gives the vector of the pixel in Cartesian coordinates. Finally query_disc is used to find all the pixels in the disc of radius $\pi/2$ for the vector found by pix2vec. This has been coded below. All the pixel numbers in the disc is then returned in the array listpix, which can then be used to set all the pixels in that hemisphere either to zero or one. In the code example below it is the southern hemisphere that is set to one, so that the northern is masked out by the template.

```
call ang2pix_ring(nside, theta, phi, ipring)

call pix2vec_ring(nside, ipring, vector)

call query_disc(nside, vector, radius, listpix, nlist)

map_half = 0.0d0

do i = 0, npix/2 - 1
    map_half(listpix(i),1) = 1.0d0
enddo
```

The co-latitude, θ, and the longitude, ϕ, has to be in radians. The co-latitude is measured southward from the north pole from 0 to π, while the longitude is measured eastward from 0 to 2π on the sphere. So θ and ϕ has to have values which corresponds to this convention.

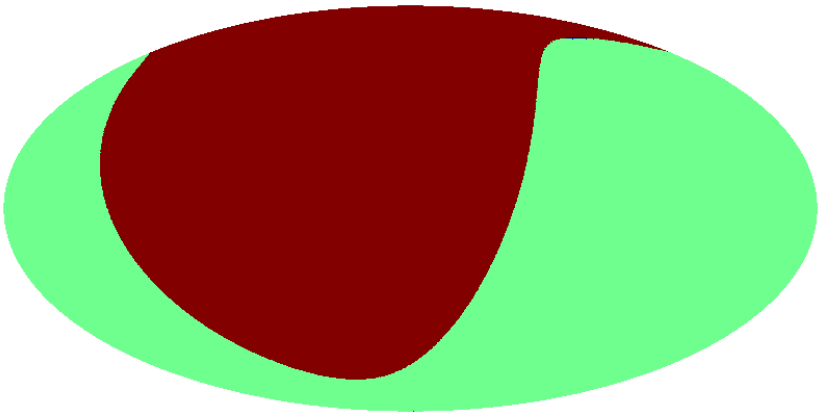

Figure 6.5: Template to analyse either the northern or southern hemisphere individually. One hemisphere is set to one and the other to zero, and this template is then multiplied into the map. Here it is the northern hemisphere that is masked out.

This template can then be multiplied with the gradient map to get only the CMB temperature gradients for one of the hemispheres. Thus this works like the mask to remove foreground contamination. The statistical tests were then applied to 1000 simulated maps for each hemisphere. These results where then compared to the WMAP data.

6.5 Simulating E-Mode Polarization

The E-mode polarization of the CMB has also been simulated. In order to do this the extended covariance matrix is required. This takes into account both temperature and polarization, and their cross correlation. This covariance matrix can easily be extended to include the B-mode polarization as well. From the power spectra of these we have

$$C = \begin{pmatrix} C_l^{TT} & C_l^{TE} \\ C_l^{TE} & C_l^{EE} \end{pmatrix} = LL^T. \tag{6.8}$$

The matrices L and L^T are a special case of LU-decomposition where the upper triangular matrix U is the transpose of the lower triangular matrix L. This is known as Cholesky factorization. The algorithm to find the elements of the lower matrix L and the upper matrix, L^T, is as follows.
The diagonal elements are given by

$$L_{ii} = \sqrt{C_{ii} - \sum_{k=1}^{j} L_{jk}}, \tag{6.9}$$

while the off-diagonal elements are given by

$$L_{ij} = \frac{1}{L_{jj}} \left(\sqrt{C_{ij} - \sum_{k=1}^{j} L_{ik} L_{jk}} \right). \tag{6.10}$$

We therefore get the following elements in the matrix L for the above covariance matrix

$$\begin{aligned} L_{11} &= \sqrt{C_l^{TT}} \\ L_{21} &= \frac{1}{\sqrt{C_l^{TT}}} C_l^{TE} \\ L_{22} &= \sqrt{C_l^{EE} - \frac{(C_l^{TE})}{C_l^{TT}}} \\ L_{12} &= 0. \end{aligned}$$

The a_{lm}'s are now given by

$$a_{lm} = L \begin{pmatrix} \eta_1 + i\eta_2 \\ \eta_3 + i\eta_4 \end{pmatrix} \tag{6.11}$$

where η_1, η_2, η_3 and η_4 are random numbers from a Gaussian distribution. As for temperature we get the same conditions as in Eqs.(6.7) and (6.2). So when $m \neq 0$ we get a division by the square root of two. Again the best-fit power spectra, to the WMAP data, for temperature, E-mode polarization and the TE cross-correlation have been used. This can now be coded similarly to the temperature a_{lm}'s in section 6.2.

```
call rand_init(rng_handle,12345+2563*myrank)

! Generate alms from the cls using the random numbers
do l = 2, lmax
   do m = 0, l

     eta  = rand_gauss(rng_handle)
     eta3 = rand_gauss(rng_handle)

     if(m==0) then
         alm(2,l,m) = (cl_te(l)/sqrt(cl_tt(l)))*eta &
         + ((cl_ee(l) - (cl_te(l)**2/cl_tt(l))))*eta3
     else
          eta2 = rand_gauss(rng_handle)
          eta4 = rand_gauss(rng_handle)

          alm(2,l,m) = (cl_bb(l)/sqrt(cl_tt(l)*2.0d0))*cmplx(eta,eta2)&
          +(sqrt(((cl_ee(l) - (cl_bb(l)**2/cl_tt(l)))/2.0d0)))&
          *cmplx(eta3,eta4)
```

```
     endif

   enddo
enddo
```

Only polarization maps without noise, instrumental beams and masks were generated. The purpose of this was to compare the E-mode polarization power spectrum to the gradient power spectrum. Here 1000 simulations of the E-mode polarization was made, and the power spectrum was found from these using Eqs.(3.20) and (3.22). Finally the average of these simulated power spectra were found. This power spectrum was then compared to the gradient power spectrum for the positive mode without any instrumental beam, noise or mask.

Chapter 7

Templates and Models

The direction function and preferred direction statistic can be used to look for a large scale pattern in the CMB. Such a pattern could be caused by, for example, rotation or defects. They can also be used to look for a dipole, residual foregrounds or point sources in the data. Here we review the templates for a dipole, foregrounds, point sources and a rotating universe described by the Bianchi VII_h model. These templates can be added to simulated CMB maps to test these statistics sensitivity to them. These statistics have also been tested for simulated maps with primordial non-Gaussianity.

7.1 Adding a Dipole

A dipole can easily be added to the simulated temperature maps. The dipole is described by

$$T(\hat{n}) = [1 + A(\hat{p}\cdot\hat{n})] \tag{7.1}$$

where A is the amplitude of the dipole, $\hat{p}$ is the unit vector for a given pixel, and $\hat{n}$ is a unit vector that describes the orientation of the dipole. Both $\hat{p}$ and $\hat{n}$ have components x, y and z. The components of $\hat{p}$ can be found using the HEALPix routine pix2vec for a given pixel, [19], and the orientation of the dipole was chosen as

$$\begin{aligned} x &= 0.9 \\ y &= \sqrt{1-0.9^2} \\ z &= 0.0. \end{aligned}$$

This dipole can be seen in Fig.7.1. With this dipole template the statistics sensitivity to a dipole could be investigated by varying the amplitude. The dipole was multiplied into the simulated temperature map.

Band	Dust:FDS	Free-free: Hα	Synchrotron:Haslam
K	6.3	4.6	5.6
Ka	2.4	2.1	1.5
Q1	1.5	1.3	0.5
Q2	1.4	1.3	0.5
V1	0.9	0.5	-0.2
V2	0.9	0.4	-0.2
W1	1.2	0.1	-0.3
W2	1.2	0.1	-0.4
W3	1.2	0.1	-0.3
W4	1.1	0.1	-0.3

Table 7.1: Foreground coefficients for the templates of dust, synchrotron and free-free emission for each channel of each frequency band. These coefficients are multiplied with the foreground templates for the maximum entropy method to get the foreground for each channel, [6].

7.2 Foregrounds

A foreground template with dust, synchrotron and free-free emission can be made by using the foreground maps on the LAMBDA webpage[1]. There is one map for each component. The templates have been made by using the Maximum Entropy Method for each of the five WMAP frequency bands, see Bennett et al.[6]. The coefficients for each component for each channel are given in Table 7.1.

The foreground components are given in mK antenna temperature, so this has to be converted to thermodynamic temperature which is given by

$$\delta T = \delta T_A[(e^x - 1)^2/x^2 e^x] \tag{7.2}$$

where $x = h\nu/kT_0$, and h is the Planck constant, ν is the observing frequency, k is the Boltzmann constant and T_0 is the CMB temperature of 2.725K, see Bennett et al.[6]. Table 6.1 gives the typical frequencies for the different bands. The different components, synchrotron, dust and free-free emission, are multiplied with the coefficients in Table 7.1, and then added together to make one map. This map is then converted from antenna temperature to thermodynamic temperature using Eq.(7.2). The template is shown in Fig.7.2. This template can then be multiplied by an amplitude so as to vary its strength, and it is then added to the temperature map.

7.3 Point Source Model

A point source model was made using the point source catalogue for the CMB-free method which identifies 417 point sources in a linear combination map of Q-,V- and W-band maps, see Gold et al.[17]. The catalogue contains the galactic coordinates of

[1] see http://lambda.gsfc.nasa.gov/

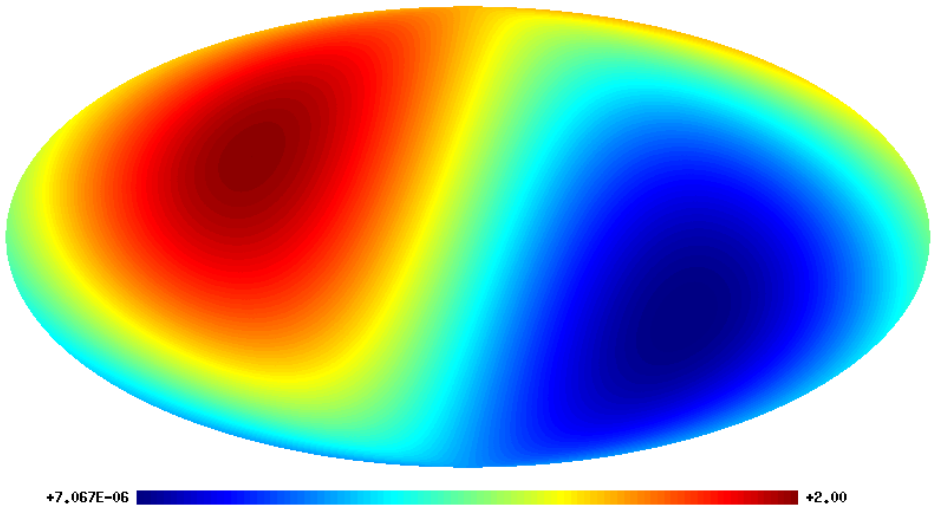

Figure 7.1: Dipole template used to test the statistics sensitivity to a dipole. This dipole was multiplied into the simulated temperature maps.

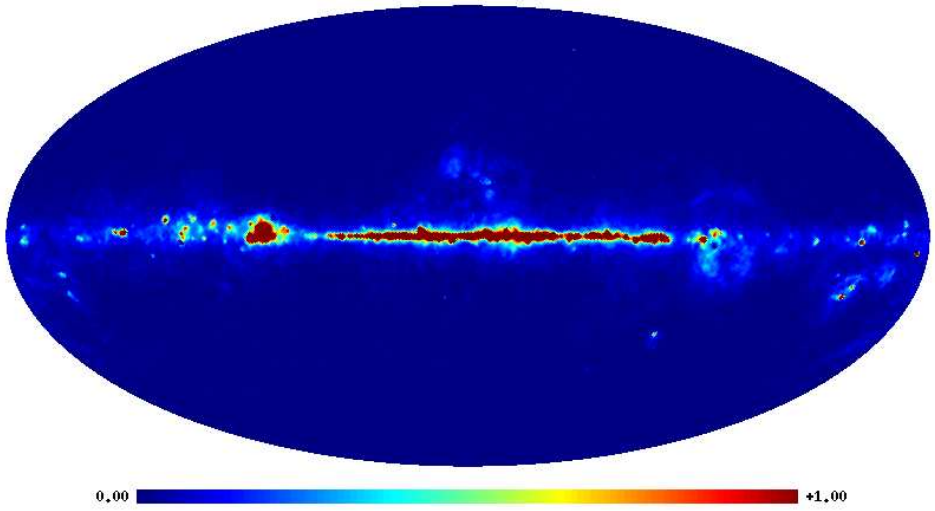

Figure 7.2: Foreground template, for the V1-channel, used to test the statistics for its sensitivity to foregrounds. It contains dust, synchrotron and free-free emission. The strongest foreground contaminant is our own galaxy.

the point sources, their flux in Jansky for each of these bands, with a flux error in Jansky. The catalogue also contains identification and distances.

The positions and flux's were used to make a high resolution map, with $N_{\text{side}} = 2048$, using the ang2pix HEALPix routine, [19]. The pixel for each position was then set

equal to the flux. Using the HEALPix routine map2alm this was then smoothed in harmonic space using Eq.(6.3) with the WMAP instrumental beam for the channel, or frequency band, of interest. The resolution of the map was set to $N_{\rm side}$ of the simulated temperature map. This was then made into a map again which was the point source template.

Since the conversion from Jansky to temperature is just a constant factor the template was kept in Jansky. An amplitude was used to vary the strength of the point sources, while at the same time the different strengths of the point sources were retained. By adjusting the amplitude of the template the statistics could be tested to see how sensitive they are to point sources. The final template can be seen in Fig.7.3. The point source template was added to the temperature map.

The same point source template was also used to test the effect of point sources in the positive gradient power spectrum. Simulations of CMB sky maps with point sources was made and the average of 1000 simulated positive gradient power spectra was found. When making this power spectrum the point source template was multiplied by an amplitude of 75 which gives strength close to that found in the WMAP data. This is for a point source template with resolution of $N_{\rm side} = 512$. In this case maps for each frequency band were used, not for each channel, so the averaged instrumental beam of each frequency band was used.

7.4 The Bianchi VII$_h$ model

The Bianchi VII$_h$ model describes an open universe, $\Omega_0 < 1$, with universal rotation and spiraling of the geodesics. In this model the temperature anisotropies can be found from

$$\begin{aligned}\frac{\Delta T}{T}(\theta_0,\phi_0) = &\left[\left(\frac{\sigma_{12}}{H}\right)_0 A(\theta_0) + \left(\frac{\sigma_{13}}{H}\right)_0 B(\theta_0)\right]\sin(\phi_0)\\ &+\left[\left(\frac{\sigma_{12}}{H}\right)_0 B(\theta_0) - \left(\frac{\sigma_{13}}{H}\right)_0 A(\theta_0)\right]\cos(\phi_0)\end{aligned} \tag{7.3}$$

where $\theta_{obs} = \pi - \theta_0$ and $\phi_{obs} = \pi + \phi_0$, and

$$\begin{aligned}A(\theta_0) = &C_1[\sin(\theta_0) - C_2(\cos(\psi_E - 3h^{(1/2)})\sin(\psi_E))]\\ &+\int_{\tau_E}^{\tau_0}\frac{s(1-s^2)\sin(\psi)}{(1+s^2)^2\sinh^4(h^{1/2}\tau/2)}d\tau\end{aligned} \tag{7.4}$$

and

$$\begin{aligned}B(\theta_0) = &C_1[3h^{1/2}\sin(\theta_0) - C_2(\sin(\psi_E - 3h^{(1/2)})\cos(\psi_E))]\\ &+\int_{\tau_E}^{\tau_0}\frac{s(1-s^2)\cos(\psi)}{(1+s^2)^2\sinh^4(h^{1/2}\tau/2)}d\tau.\end{aligned} \tag{7.5}$$

Here

$$C_1 = (3\Omega_0 x)^{-1}, \tag{7.6}$$

$$C_2 = \frac{2s_E(1+z_E)}{1+s_E^2}, \tag{7.7}$$

$$C_3 = 4h^{1/2}(1-\Omega_0)^{3/2}\Omega_0^{-2}, \tag{7.8}$$

and

$$s = \tan\left(\frac{\theta_0}{2}\right)\exp[-h^{1/2}(\tau-\tau_0)], \tag{7.9}$$

$$\psi = (\tau-\tau_0) - h^{1/2}\ln\left[\sin^2\left(\frac{\theta_0}{2}\right) + \exp(2h^{1/2}(\tau-\tau_0))\cos^2\left(\frac{\theta_0}{2}\right)\right]. \tag{7.10}$$

The limits are given by

$$\tau_0 = 2h^{-1/2}\sinh^{-1}[(\Omega_0^{-1}-1)^{1/2}] \tag{7.11}$$

and

$$\tau_E = 2h^{-1/2}\sinh^{-1}\left[\left(\frac{\Omega_0^{-1}-1}{1+z_E}\right)^{1/2}\right]. \tag{7.12}$$

This model has two variables Ω_0, the current total energy density, and x (or h) which is given by

$$x = \left(\frac{h}{1-\Omega_o}\right)^{1/2}. \tag{7.13}$$

The physical meaning of x is related to the characteristic wavelength over which the principle axes of shear and rotation changes orientation,[3]. The amplitudes, $(\frac{\sigma_{12}}{H})_0$ and $(\frac{\sigma_{13}}{H})_0$, are dimensionless, and can be chosen to equal each other. This can then be used to adjust the amplitude of the model. For more details on this model see Barrow et al.[3] and Collins and Hawking [10].

By solving the above equations a template of the Bianchi VII$_h$ model can be made with an amplitude that can be varied. The integral can be solved using numerical integration, and it has been found that Simpson's method is sufficient to do this. The algorithm for Simpson's method is

- Chose the number of mesh points and fix the step, h
- Calculate the function for the limits a and b, (given by τ_0 and τ_E in this case)
- Perform a loop over n to $n-1$ summing up

  $$4f(a+h) + 2f(a+2h) + 4f(a+3h) + ... + 4f(b-h) \tag{7.14}$$

  where f is the function
- Multiply by $\frac{h}{3}$

Parameter	Best-fit value
x	0.55
Ω_0	0.50
$\left(\frac{\sigma}{H}\right)_0$	2.4×10^{-10}
$\left(\frac{\omega}{H}\right)_0$	6.1×10^{-10}
(l, b)	(222°,-62°)

Table 7.2: Best-fit parameters of the Bianchi VII_h model. These are the parameters found by Jaffe et al.,[28].

where $h = \frac{b-a}{n}$ with n number of steps, [1]. This model has got some attention because of the features in the southern hemisphere that could explain the asymmetry which has been observed by some research groups and could cause the features seen in the WMAP data, [14], [15], [39], [40]. To see this the model can be rotated so that the spiral no longer lies along the z-axis. The rotated model, which fits the observations, can be seen in Fig.7.4. The rotation can be done using the Euler angles $(42°, 28°, -51°)$ in harmonic space, see Wandelt et al.[43]. This best fit model to the WMAP data have the parameters listed in Table 7.2 rotated by the above Euler angles. This model is that found by Jaffe et al.[28] (see also Jaffe et al.[29]). The model was added to the temperature map.

7.5 A Non-Gaussian Model: Testing different f_{NL}'s

A model with non-Gaussian anisotropies has also been tested. The cosmological model which these maps are based on is a ΛCDM model with $\Omega_b = 0.05$, $\Omega_c = 0.25$, $\Omega_v = 0.70$, $h = 0.65$ and $n = 1.00$. The 300 simulated CMB temperature maps for this model has been made by Frode Hansen, Michele Liguori and Sabino Matarrese. The a_{lm}'s from these maps are built with two parts, a_{lm}^G and a_{lm}^{NG} such that

$$a_{lm} = a_{lm}^G + f_{NL} a_{lm}^{NG}. \tag{7.15}$$

Here f_{NL} is the amplitude of the primordial non-Gaussianity. These maps were then treated in exactly the same way as all the other maps that the statistical tests have been applied to. The maps have also been scaled so that the first peak in its power spectrum corresponds to the first in the power spectrum of the ΛCDM model with Gaussian anisotropies. So the value of C_l at $l = 220$ was set to be $5786\mu K^2$. The details and description of how these maps were made is found in M.Liguori et al.,[34],[35].

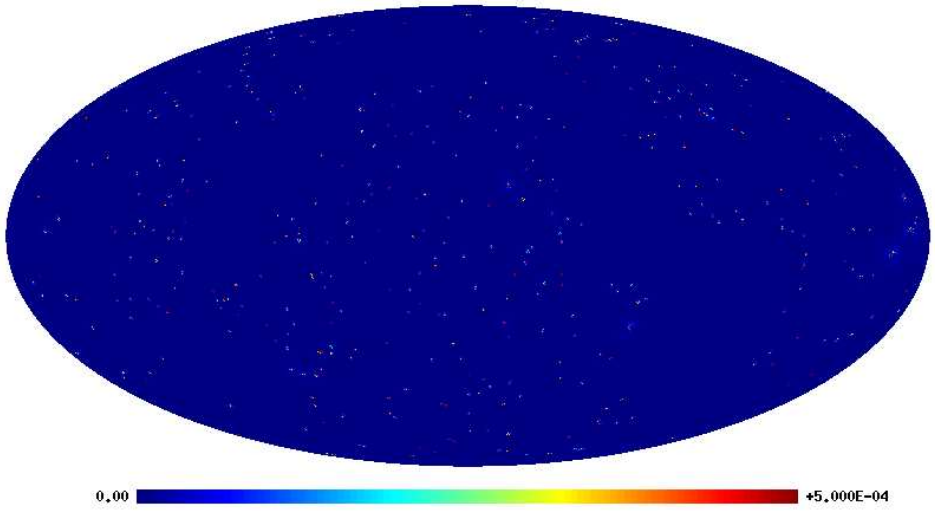

Figure 7.3: Point source template used to test the statistics for its sensitivity to point sources. This point source model was also used to look at the point source contribution to the gradient power spectrum.

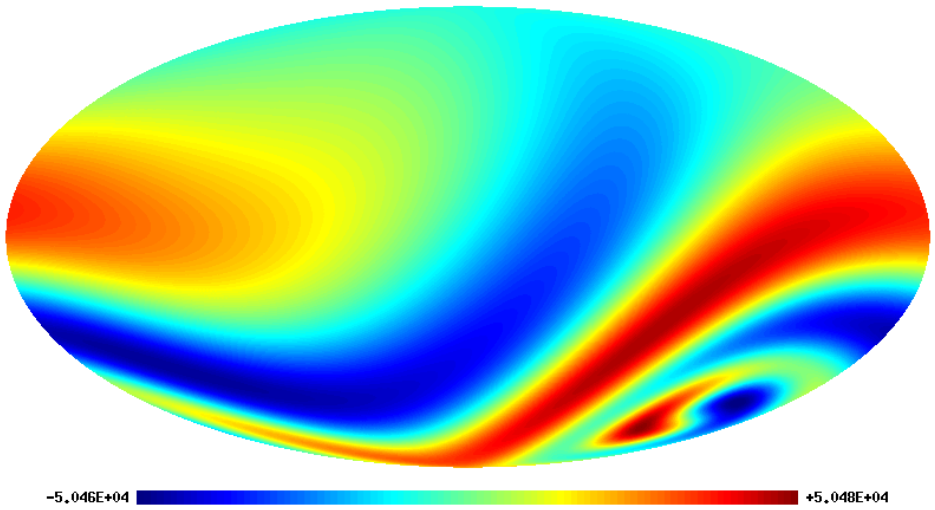

Figure 7.4: Rotated version of the Bianchi VII$_h$ model which the statistical tests were tested for. The parameters chosen were $x = 0.55$ and $\omega_0 = 0.5$ which is the best-fit model to the WMAP data found by Jaffe et al., [28].

Chapter 8

Implementing the MASTER algorithm

We now have everything we need to run simulations, calculate the gradients, and find the statistics from these and from the WMAP data. We also have the equations to implement the MASTER algorithm. In this chapter the details of the implementation of the MASTER algorithm will be presented as well as the treatment of the maps which differs from that done previously when applying the statistical tests. Some of the code of the equations used are also presented. We will also look at the CPU time and the memory requirements of this algorithm.

8.1 Details on the Implementation

As for the statistical tests simulated CMB temperature maps, see section 6.2, were used to get power spectra to compare with the estimates form the WMAP data. These simulated CMB sky maps were also used to test the algorithm. However, when analysing the maps to get the power spectra the instrumental beam was not changed. The original beam for the frequency was kept and the maps were analysed with $N_{\text{side}} = 512$.

The mask in Fig.6.3 was also applied to the simulations and to the WMAP sky maps, but was smoothed with a beam of $50'$. The second mask, which was applied after the gradient had been found, was smoothed with a beam of $100'$ and the point source mask was also used. The reason for the smaller second mask was that the maps had not been smoothed with a large beam, and so the first mask was smoothed less. This means that a smaller mask was sufficient to deal with the border effects.

The point source mask was also used as point sources will have an effect on the results as the maps have not been smoothed with a larger beam. Thus the point source mask was kept in the mask in Fig.6.3 when estimating the temperature power spectrum. For the gradients the point source mask was added to the larger mask applied after the gradients had been found. Adding the point source mask before finding the gradients will only cause more border effects for which a larger point source mask would be required. Since the point source mask is not added before finding the gradients some

effect could appear in the power spectrum.

In this analysis the maps for each channel in each frequency band was added, and the average was found to give maps for the Q-, V- and W-bands. The instrumental beams were also averaged for each frequency band. The HEALPix routine map2alm was again used to find the a_{lm}'s of these maps, and from these the pseudo-power spectrum was found using Eq.(3.6). There is also a HEALPix routine, map2alm_spin, which converts a spin-s map into spin a_{lm}'s which is needed when finding the gradient power spectra, or the polarization power spectra, see section 3.4.

The noise is found for each pixel as described in section 6.2 using Eq.(6.4). A map of just the noise can be made, and then treated in the same way as if it was a CMB temperature map. Thus when estimating the gradient noise power spectrum the gradients of the noise map are calculated in the same way as for the CMB sky maps. The same masks are also applied to the simulated noise maps. The noise power spectrum is then found from the same equation, Eq.(3.6), as the CMB temperature pseudo-power spectrum, or gradient pseudo-power spectra. Monte Carlo cycles were run to get an average of the noise power spectrum. Here 1000 simulations were used to get estimates of the temperature noise power spectrum, as well as the gradient noise power spectra.

Having subtracted the noise power spectrum from the pseudo-power spectrum only the total beam, instrumental beam and smoothing due to the finite pixel window, and the effect of the mask need to be removed. The total beam has here been included in the mode-mode coupling kernel which removes the effect of the mask. The implementation of the mode-mode coupling kernel for temperature and gradients are presented in sections 8.1.1 and 8.1.2.

When these components have been found we can use Eq.(4.15) and Eq.(4.41) to get an estimate of the temperature or positive gradient power spectrum respectively. The example below implements Eq.(4.41) for the positive gradient power spectrum.

```
do b = 0, nbins - 1
  do bb = 0, nbins - 1
    do l = llow*bb, llow + llow*bb - 1
      cls(b) = cls(b)+(Mbb_total(b,bb)*pbl(bb,l)*(cls_spin(l,1)-Nl(l,1)))&
      +(Mbb_total(b,bb+nbins)*pbl(bb,l)*(cls_spin(l,2) - Nl(l,2))))
    enddo
  enddo
enddo
```

Both the temperature and gradient power spectra were binned with 25 C_l's in each bin using the binning operators given by Eqs.(4.16) and (4.17). All of these equations are found in chapter 4.

8.1.1 Mode-Mode Coupling Kernel: Temperature

Having found the noise power spectrum we now need the mode-mode coupling kernel and we also need to remove the total beam from the pseudo-power spectrum. The

mode-mode coupling kernel can be found from Eq.(4.12) in section 4.1. To evaluate this expression we need to find the power spectrum of the mask. This can be done in the same way as for the pseudo-power spectrum and the noise power spectrum using Eq.(3.6). We also need the Wigner 3j symbols which can be found by using the routine DRC3JJ[1]. For the CMB temperature power spectrum the mode-mode coupling kernel was coded as seen below.

```
do l_1 = 0,lmax
  do l_2 = l_1,lmax
    l2      = real(l_1,dp)
    l3      = real(l_2,dp)
    lminint = abs(l_1-l_2)
    lmaxint = l_1+l_2
    l1min   = real(lminint,dp)
    l1max   = real(lmaxint,dp)
    ndim    = lmaxint-lminint+1

    call  DRC3JJ(l2, l3, m2, m3, l1min, l1max, wig3j(lminint:lmaxint),&
    ndim, ier)
    if(ier/=0.0d0) print*,'Error in coefficients', ier

    do l_3 = lminint, lmaxint
       Mll(l_1,l_2) = Mll(l_1,l_2) + ((2.0d0*l3 +1.0d0)&
                    *(2.0d0*real(l_3,dp)+1.0d0)&
                    *Wl(l_3,1)*(wig3j(l_3))**2)
    enddo

    Mll(l_2,l_1) = Mll(l_1,l_2)/(2.0d0*l3 +1.0d0)*((2.0d0*l2) + 1.0d0)

  enddo
enddo
```

Here m2 = 0 and m3 = m2 give the zero-spin Wigner 3j symbols. The routine to find the Wigner 3j symbols takes in m2 and m3, l2 and l3, and returns all values of the symbol for all possible values of l1. These are then summed over to find the mode-mode coupling kernel. Also the loop over l_1 and l_2 has been code so that the full mode-mode coupling matrix is found by setting Mll(l_2,l_1) equal to Mll(l_1,l_2). This simply fills up the entire matrix while reducing the number of loops, and therefore the time requirements.

The total beam, B_l, was multiplied into the mode-mode coupling matrix which was then binned using Eqs.(4.16) and (4.17). Finally the inverse of this binned matrix was found and this inverse multiplied by 4π to get the mode-mode coupling kernel for temperature.

[1]This routine has been made by Gordon, R. G., Harvard University, and Schulten, K., Max Planck Institute

8.1.2 Mode-Mode Coupling Kernel: Gradients

For the gradients the mode-mode coupling kernel is given by Eq.(4.42), described in section 4.2.2. When implementing Eq.(4.42) the loops over l_1 and l_2 are identical to the temperature case in section 8.1.1, but we now have two expressions for $M_{l_1 l_2}$.

```
do l_3 = lminint, lmaxint
  Mll_spin(l_1,l_2,1) = Mll_spin(l_1,l_2,1) + (ls(l_3)&
                        *((2.0d0*l3) + 1.0d0)&
                        *Wl(l_3,1)*wig3j(l_3)**2 &
                        *(1.0d0 + (-1.0d0)**(l_1+l_2+l_3)))

  Mll_spin(l_1,l_2,2) = Mll_spin(l_1,l_2,2) + (ls(l_3)&
                        *((2.0d0*l3) + 1.0d0)&
                        *Wl(l_3,1)*wig3j(l_3)**2 &
                        *(1.0d0 - (-1.0d0)**(l_1+l_2+l_3)))
enddo

Mll_spin(l_2,l_1,1) = Mll_spin(l_1,l_2,1)/((2.0d0*l3) + 1.0d0)&
                      *(2.0d0*l2+1.0d0)
Mll_spin(l_2,l_1,2) = Mll_spin(l_1,l_2,2)/((2.0d0*l3) + 1.0d0)&
                      *(2.0d0*l2+1.0d0)
```

Here m2 = 1 and m3 = −m2 for the spin-1 Wigner 3j symbols, and the routine to find the Wigner 3j symbols, DRC3JJ, is the same as in section 8.1.1. Also Mll_spin(l_1,l_2,1) gives $K^{+}_{ll'}$ and Mll_spin(l_1,l_2,2) gives $K^{-}_{ll'}$. As for temperature the indices of the final expression for the mode-mode coupling matrix is exchanged. The mask power spectrum is found in the same way as for temperature, but for the last mask applied to the gradient map which is larger.

However, as there are two components these were combined to give the matrix

$$\begin{pmatrix} K^{+}_{ll'} & K^{-}_{ll'} \\ K^{-}_{ll'} & K^{+}_{ll'} \end{pmatrix} \tag{8.1}$$

which is an $l_{\max} \times l_{\max}$ matrix. This large mode-mode coupling matrix was then binned using Eqs.(4.16) and (4.17), and the total beam, B_l, was multiplied into this matrix.

Finally the factor 8π was multiplied into the inverse mode-mode coupling matrix. This then accounts for the mask and the beam so that these, together with the noise could be removed from the pseudo-power spectra and give an estimate of the gradient power spectra.

8.2 CPU Time and Memory Usage

We will now look at the time and memory usage of this algorithm. In Fig.8.1 the CPU time for this algorithm, when estimating the gradient power spectra, is shown as a

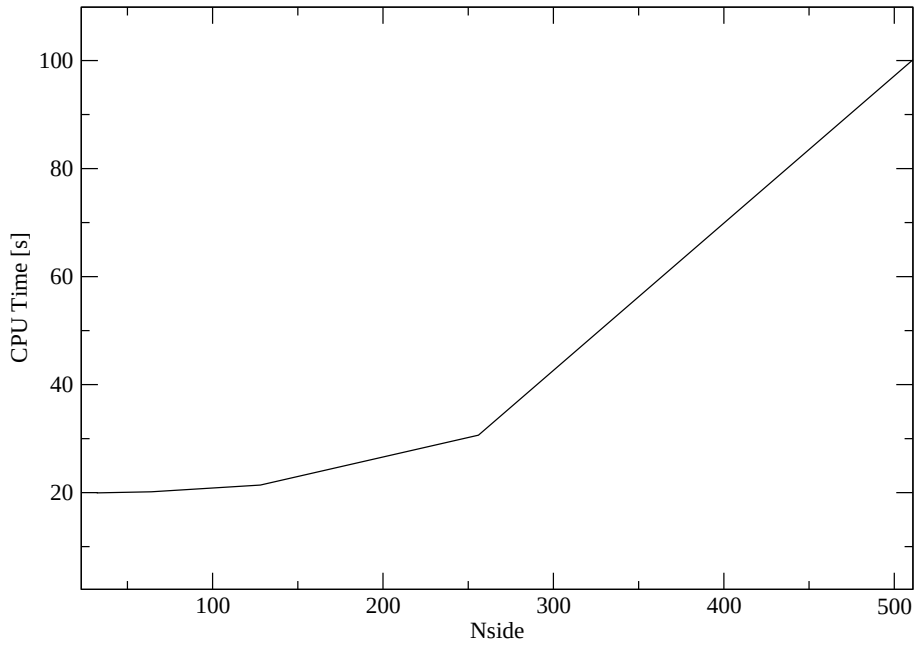

Figure 8.1: CPU time for different map resolutions,$N_{\rm side}$, has been plotted. This shows how the higher resolution maps use more CPU time as expected, and how much more compared to the lower resolution maps.

function of $N_{\rm side}$. Here the calculation of the gradients and the pseudo-power spectrum is included in the CPU time as we are mainly focusing on the gradient power spectra. Thus finding the temperature power spectrum is less time consuming.

From this plot it can be seen that the CPU time increases with the resolution of the map as expected, but the analysis for $N_{\rm side} = 512$ does not take a lot of time.

Also, for low $N_{\rm side}$ the difference in the CPU time becomes smaller. This is partly due to the smaller difference in resolution and partly to the mask used which has a resolution of $N_{\rm side} = 512$ so that its resolution has to be changed for the lower resolution maps. This becomes more time consuming for the lower resolution maps. In addition there is also the time used to setup simulated maps or read in WMAP data.

Due to the relatively short time it takes to run this algorithm it is feasible to run many simulations of the positive gradient power spectrum. In this work 1000 simulated maps were used which was completed in a couple of hours when paralellizing the code and running it on 20 CPUs.

The code presented in this chapter has not been optimized much, and more can

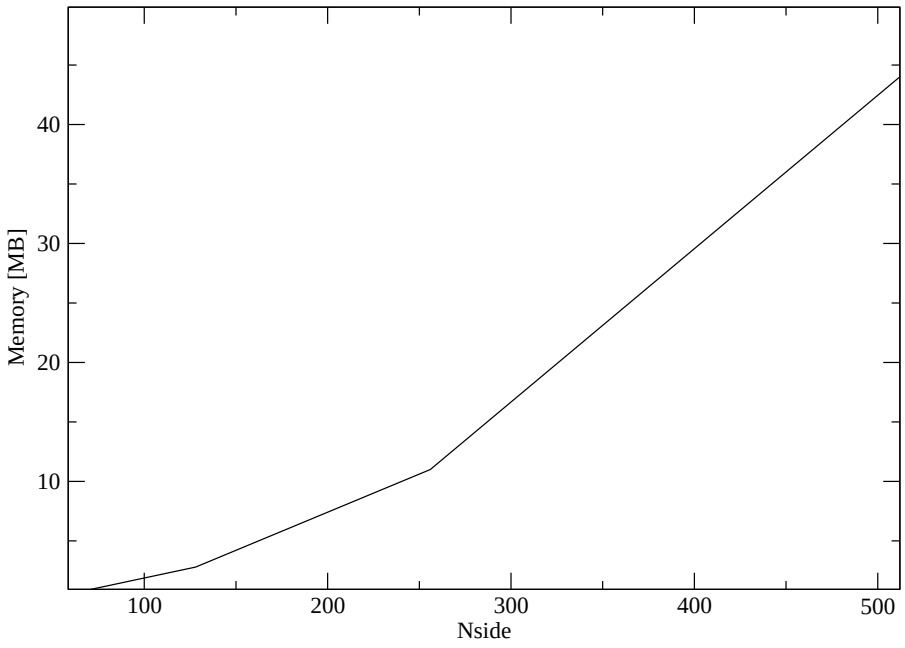

Figure 8.2: Minimum amount of memory required as a function of $N_{\rm side}$ has been plotted. This is the minimum amount of memory used by the MASTER algorithm alone. Additional memory to store maps and gradients is required as well as when binning the power spectrum.

probably be done to reduce the CPU time. This could be an advantage when in the future the power spectra is estimated up to higher values of l from higher resolution maps. Although the CPU time is much larger for Nside $= 512$ than the lower resolutions, this algorithm is still viable for higher resolutions as well, like for estimation up to $l = 2048$.

In Fig.8.2 the memory usage of the MASTER algorithm is presented as a function of $N_{\rm side}$. This is an estimation of approximately how much memory is used to store variables. The values presented are the minimum amount of memory needed for the algorithm. There will be smaller additions when binning the power spectrum, but this will depend on how many bins that are chosen. In addition to this the array holding the temperature map and the gradient map will take up memory of order $N_{\rm pix} = 12 \times N_{\rm side}^2$ multiplied by 64 bits if using double precision variables. All variables here have been saved as double precision variables to avoid loss of precision.

Part III

Results

Chapter 9

Templates and Models: Results

We will now look at the results for the maximum value of the direction function for the different templates and models presented in chapter 7. The sensitivity of the maximum value of the direction function, Eq.(5.1), to these has been tested by varying the strength or amplitude of the templates or models. Here 1000 simulations have been run for each template and for a number of amplitudes, and the results are presented as histograms of the distribution of these results. The simulated maps have been treated as described in sections 6.2 and 6.3.

9.1 Testing for a Dipole

The first template that was considered was a dipole. The results for three different amplitudes, compared to a map without a dipole, can be seen in Fig.9.1. The dipole moves the results to higher values of the maximum value of the direction function. For a dipole with an amplitude of 1.0 the direction function gives results that does not overlap with the test distribution without a dipole. Even for a dipole amplitude of 0.5 the difference between the distributions are easily seen. From these results the amplitude of the dipole is found to be approximately 0.3 at 2σ. So the maximum value of the direction function is sensitive to a dipole. This is in agreement with [8]. This can also be used to see if the WMAP results for this statistic is affected by a dipole.

9.2 Results on the Sensitivity to Point Source

A point source model was also added to simulated temperature maps to test the statistics sensitivity to point sources. Here it was tested if, for a map smoothed with a beam of 4° and a resolution of $N_{\text{side}} = 128$, the point sources could be resolved with the maximum value of the direction function, or affect the results of this statistic. It was also test how strong the point sources would have to be in order for the maximum of the direction function to detect them.

In Fig.9.2 the results are shown with the point source model compared to the results for sky maps without point sources. It can be seen that the amplitude required for this

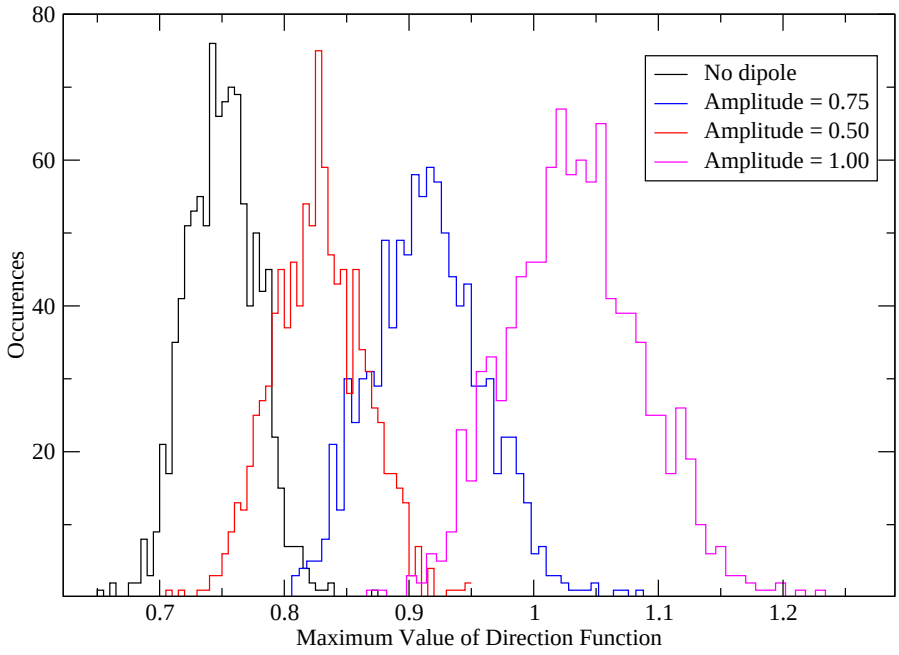

Figure 9.1: Results for three different amplitudes of the dipole. These are then compared with the results for sky maps without a dipole. It can be seen that the maximum value of the direction function is sensitive to dipoles with amplitudes of less than 1.0.

statistic to resolve the point sources is large, close to 300. For a point source amplitude of 600 the distribution with point sources does not overlap with the distribution without point sources. From these distributions it is found that the point sources amplitude is approximately 246 at 2σ. When finding the statistic from the WMAP data this can be compared to these results to see if they are affected by point sources.

A 4° beam has been used on all maps which the direction function has been applied to, and it was also used here. However, this makes the point sources undetectable by the statistic unless the amplitudes are large as can be seen from the results presented in this section. Thus to look for point sources in the data, using this statistic, a smaller beam should be used. This was not done here due to time constraints. However, the effect of point sources in the data have been investigated further in chapter 11. In this chapter the gradient power spectrum has been used to find a relationship between the strength of the point sources and the frequency of observation. The effect of point sources on this power spectrum is also shown.

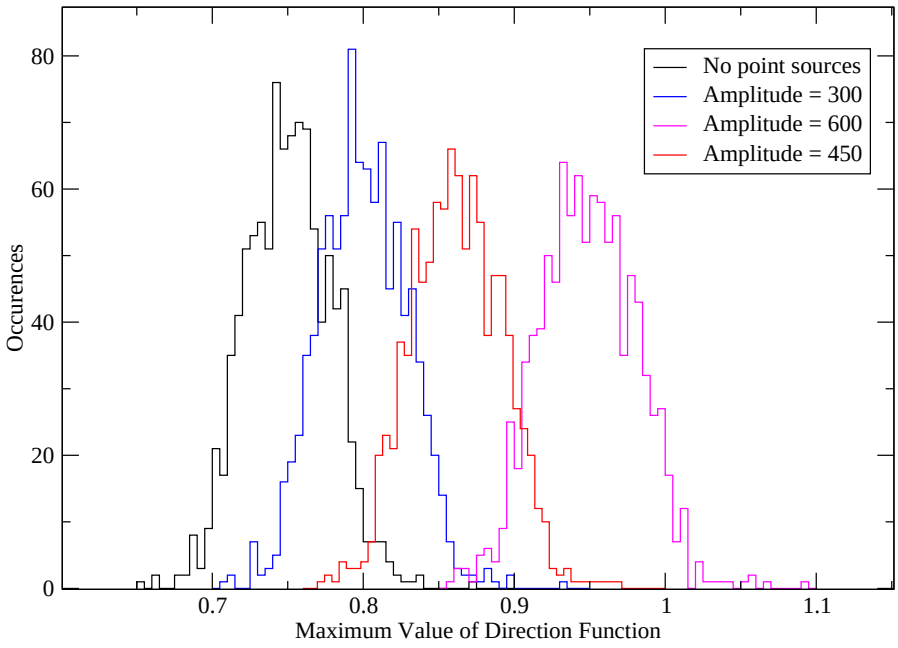

Figure 9.2: Results for the point source model for three different amplitudes compared to the results without any point sources. At the level of smoothing used the maximum of the direction function is not very sensitive to point sources.

9.3 Effect of Foregrounds

In Fig.9.3 the results for the maximum value of the direction function for foregrounds are seen. This plot shows the results for three different amplitudes compared to a map without any foregrounds. Since the foregrounds are a lot stronger than the CMB temperature even small amplitudes of these makes a difference to the results of the direction function as this increases the gradients. No masks were applied when testing for foregrounds and the result without the foreground template does not have a mask applied to it either. It thus differs from the above results without a dipole or point sources.

With an amplitude of 0.125 only the far end of the tail of this distribution is overlapping with the tail of the distribution without any foregrounds. With an amplitude of 0.150 the foreground distribution no longer overlap with the distribution without foregrounds. For the foregrounds an amplitude of approximately 0.04 at 2σ was found. So the maximum value of the direction function is very sensitive to foregrounds. Thus

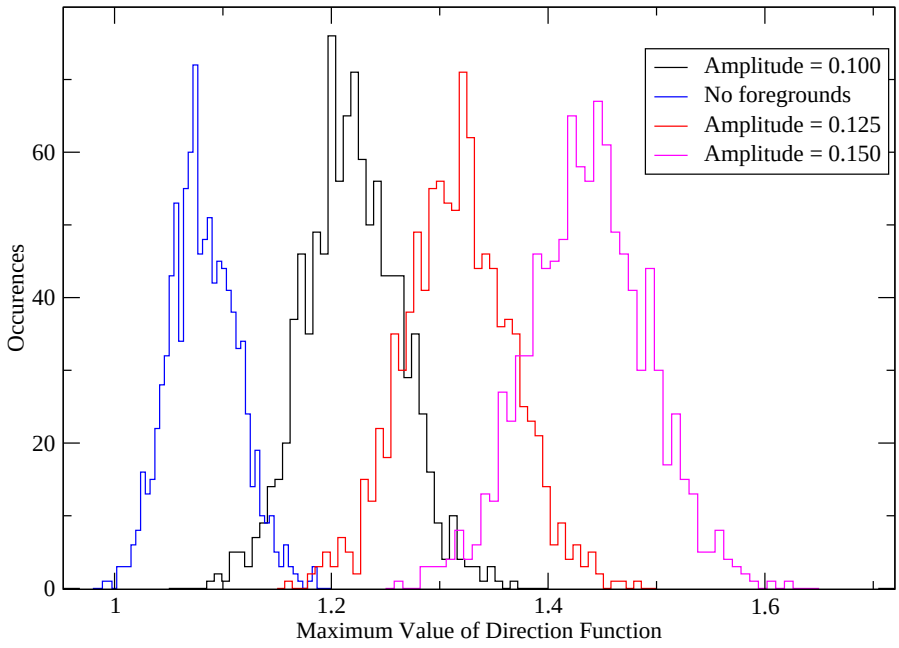

Figure 9.3: Results for foregrounds for three different amplitudes. These are compared to the results for sky maps without any foregrounds. The maximum of the direction function is very sensitive to foregrounds as these are a lot stronger than the CMB signal, and it shows how important it is to mask out the foregrounds.

not masking out the foregrounds would make the value of the direction function a lot larger than if it was only affected by the CMB temperature, and it is therefore essential that the foregrounds are masked out. This also means that any residual foregrounds in the map can affect the results of this statistic, and thus also the preferred direction statistic. By comparing the WMAP results with these results it can be checked for foreground contamination.

9.4 Results for the Bianchi VII$_h$ Model

In Fig.9.4 the results for the Bianchi VII$_h$ model is shown. The distributions of results for the three different amplitudes of the Bianchi VII$_h$ model have been plotted along with the results for a universe without the Bianchi VII$_h$ structure. All amplitudes are of order 10^{-6} in the plot. For this model an amplitude was found of approximately

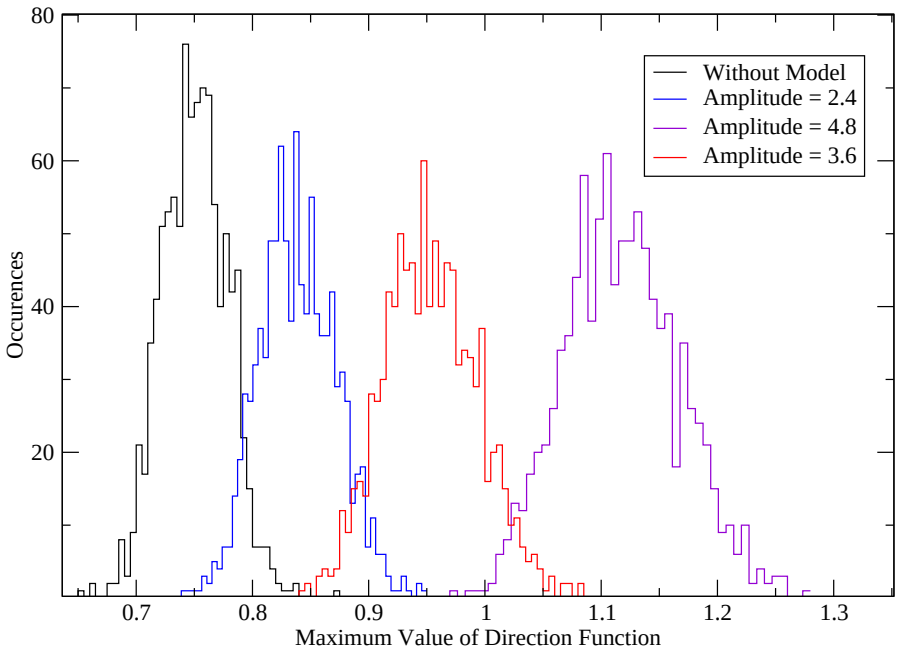

Figure 9.4: Results for three different amplitudes of the Bianchi VII$_h$ model compared to the results without this model. The amplitudes are of order 10^{-6}. From this it can be seen that the maximum of the direction function cannot differ between a Bianchi VII$_h$ universe with the best-fit amplitude of 2.4×10^{-10}, Jaffe et al.,[28], and a universe without any of the features of this model.

1.22×10^{-6} at 2σ. If the amplitude is lower than this the maximum of the direction function does not detect the Bianchi VII$_h$ structure.

The best-fit amplitude found by Jaffe et al.[28] was 2.4×10^{-10}. All the parameters for the best-fit model are given in section 7.4, Table 7.2. However, the maximum of the direction function cannot differ between this best-fit model and a map without any template. For the statistic to be able to detect a Bianchi VII$_h$ universe the amplitude has to be of order 10^{-6}. If this is not the case the statistic will not be able to detect whether we live in a Bianchi VII$_h$ universe, i.e. a rotation universe.

9.5 Statistics Sensitivity to Non-Gaussianity

In Fig.9.5 and Fig.9.6 the results for the Non-Gaussian model is shown. The maximum of the direction function was tested for various values of the amplitude of primordial non-Gaussianity, f_{NL}. For f_{NL} equal to 0, 100 or -100 the statistic cannot differ between the maps. For the statistic to detect the non-Gaussianity in the maps f_{NL} has to be of order 10^3. Only when f_{NL} is greater than this is there a difference in the results of this statistic. For positive value of f_{NL} it was found that this amplitude was approximately 2957 at 2σ. For negative values of f_{NL} it was found to be approximately -2732 at 2σ.

When the amplitude of the primordial non-Gaussianity, f_{NL}, increases the the statistic moves to higher values. However, the range of the results also increases, so that the different distributions of results overlap. This makes it difficult to determine which distribution the results may come from. Thus, there would have to be a large non-Gaussianity, $f_{NL} > 5000$, in order for the statistic to give completely different results. This means that this statistic cannot be used to put any further constraints on the values of f_{NL} compared to other research groups. This can also be seen from the amplitudes at 2σ. Unless there is a large non-Gaussianity in the CMB this statistic will not detect it.

The value of f_{NL} has been constrained by many different research groups. Creminelli et al. found $-36 < f_{NL} < 100$ with a 95% confindence level (C.L.), using a three point function on the three year WMAP data, [11]. Yadav and Wandelt found $27 < f_{NL} < 147$ with a 95% C.L, by analysing the bispectrum of the three year WMAP data, [45]. They also rejected $f_{NL} = 0$ at 2.8σ. This rules out the slow-roll inflationary scenario. Hikage et al. found the constrains $-70 < f_{NL} < 91$ (at 95% C.L.) using Minkowski functionals, [25]. Comparing these estimates to that of the statistic used here it is unlikely that this statistic will give any further insight into the constraints on f_{NL} when applied to the WMAP data. With the high resolution data from Planck it is hoped that f_{NL} will be constrained further, and so also the models of inflation.

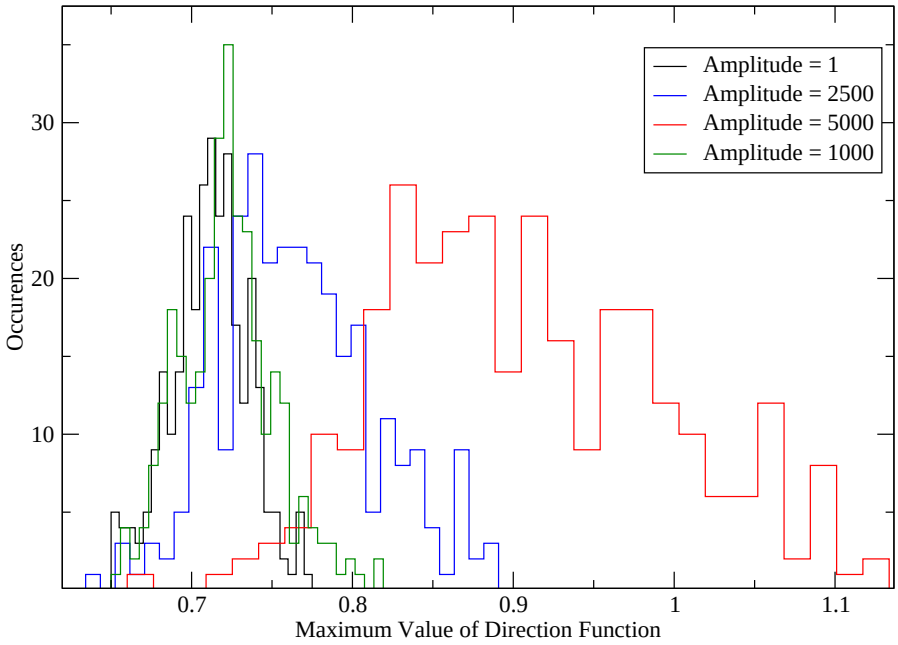

Figure 9.5: Maximum value of the direction function for a model with primordial non-Gaussianity. The amplitudes are the f_{NL}'s used in the simulations. Here positive values of f_{NL} have been chosen when running the 300 simulations. It can be seen that it will be difficult to use this statistic to gain any further knowledge of the amount of non-Gaussianity as this would have to be large for the statistic to be able to differ between this case and the Gaussian anisotropies.

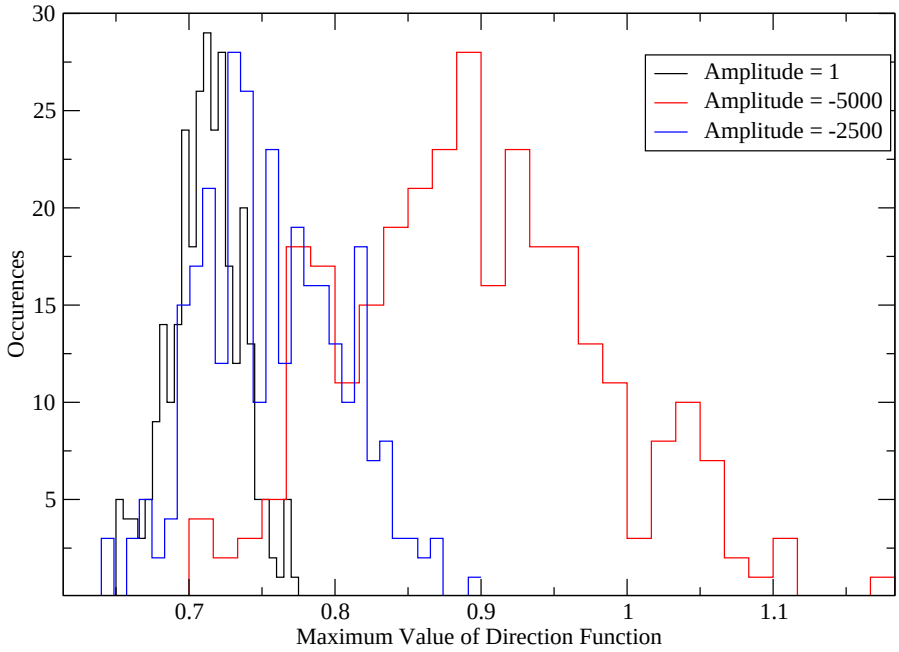

Figure 9.6: Maximum value of the direction function for a model with primordial non-Gaussianity. The amplitudes are the f_{NL}'s used in the simulations. Here negative values of f_{NL} have been investigated. Large negative values of f_{NL} is also required for the statistic to be able to detect any non-Guassianity in the CMB.

Chapter 10

The WMAP data: Results from the Statistical Tests

We have now seen how the maximum value of the direction function, Eq.(5.1), is sensitive to various templates. Here we will look at the statistical tests for simulations of the CMB with Gaussian anisotropies compared to that found from the WMAP seven year data. Although it has been shown that the direction function is not very sensitive to some of the templates and models tested in chapter 9 it will still be applied to the WMAP data along with the other statistical test defined in chapter 5. It may still detect some effect or anomalies in the CMB.

10.1 Testing the Gradient Distribution

Before we look at the results from the direction function and preferred direction statistic the results from the other statistical tests of the gradient distribution will be presented. The gradients from a CMB map can be found from Eqs.(3.11) and (3.14). Here gradients from a 1000 simulations of the ΛCDM model have been compared with the gradients from the WMAP data. Two tests were applied, these were the χ^2-test and the Kolmogorov-Smirnov test.

Fig.10.1 shows two histograms of all the D-values of the Kolmogorov-Smirnov test, both for the simulations compared to WMAP and for simulations compared to other simulations. This shows that the simulated CMB sky maps give cumulative distribution functions, of the gradient probability distributions, very close to the cumulative distribution function of the WMAP data, with a difference of order 10^{-2}. This is also the case when using this test on simulations only. The probability for the Kolmogorov-Smirnov results has also been calculated using Eq.(5.9). The probabilities for the results in Fig.10.1 were found to be more than 50% in all cases. The distribution of the probabilities has a peak at 50%, while the rest of the results are distributed evenly between 50% and 100%. So none of the results from this test are unlikely.

For the χ^2-test 500 simulations were used to find the mean, and then another 500 simulations were used make a distribution of the χ^2 results. Here the gradient

probability distribution was divided into one hundred intervals. By finding χ^2 from the WMAP gradients these could now be compared with the χ^2 distribution. This can be seen in Fig.10.2 for the χ^2-test without the covariance matrix. The value of χ^2 for WMAP was ≈ 92, and lies close to the middle of distribution.

With the covariance matrix the results are more spread out and higher values of χ^2 also appear in the distribution seen in Fig.10.3. Here 800 simulations were used to build the covariance matrix and find the mean of each interval. The same number of intervals were used, and 400 simulations were used to get the distribution of χ^2 in Fig.10.3. With the covariance matrix the WMAP result became $\chi^2 \approx 80$. This shows that there is some correlation between the results of the χ^2-test.

From these results there does not seem to be any anomalies in the gradient distribution of the WMAP data. The gradients from this data seems to come from the same distribution as the gradients from the simulated maps. Thus the simulated maps, using the ΛCDM model with Gaussian anisotropies, is a reasonable model to use for comparison with the WMAP data.

10.2 Results from the Direction Function and Preferred Direction Statistic

Having compared the gradients from simulations and WMAP data, to see that the simulations are reasonable, we now turn to the direction function and preferred direction statistic given by Eq.(5.1) and Eq.(5.2). Figs.10.4 and 10.5 show the results from 1000 simulated maps as histograms of the maximum and minimum values of the direction function respectively, as well as the WMAP results. The preferred direction statistic which is the ratio of the maximum to minimum values, Eq.(5.2), has also been found for all the simulations and for WMAP. The histogram of these results can be seen in Fig.10.6.

The WMAP results for the maximum of the direction function is within 2σ of the mean of this distribution. However, the minimum value, and the ratio of the maximum to minimum, both lie within 1σ of the mean. The WMAP results shown in the figures is that of V1-channel. The results for the other channels are given in Table 10.1 and are close to the V1-channel results. All these results lie within the same standard deviations of the mean of their distributions as the V1-channel results, so 2σ for the maximum and 1σ for the minimum for the direction function, and within 1σ for the ratio. In this table the probability to exceed (PTE) can also be found for all the results. For the V1-channel these are 92.1% for the maximum value, 78.9% for the minimum and 64.5% for the ratio.

From the results of all the channels there are some variations, the largest of which are for the W-band channels. There seems to be a small effect from the different noise properties and instrumental beams of each channel, but the basic results are still the same. The Gaussian beam of 4° that was used to smooth the maps has therefore been successful in reducing the noise in the maps so that is does not affect the results by much. Thus there does not seem to be any preferred direction in the CMB, or any

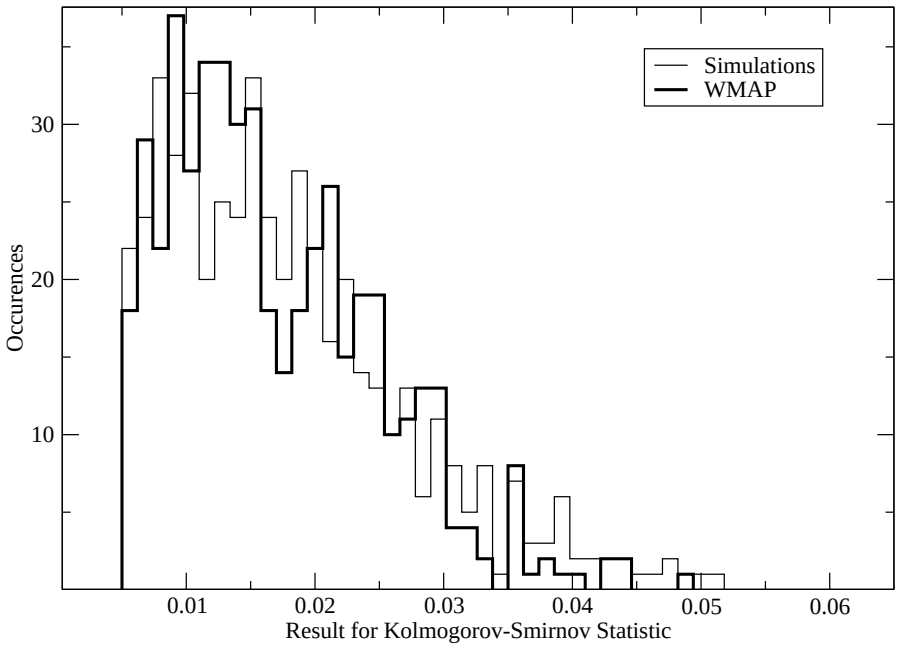

Figure 10.1: Kolmogorov-Smirnov test applied to the gradients of 1000 simulated temperature maps, with Gaussian anisotropies, compared to the WMAP data from the V1-channel. As all the values are small the difference between the cumulative distributions from simulations and from the WMAP data is small.

other anomalies that can be detected with these statistics. The ΛCDM model with Gaussian fluctuations also holds in this case.

The results from the maximum of the direction function can also be compared to the simulations with the different templates in chapter 9. From the result of a dipole it can be seen in the results from WMAP that there is no dipole which is affecting the result. Neither are there any foregrounds that have not been masked out properly, and would affect the result. This can be seen as the result from WMAP does not move towards higher values of the statistic, and as it is close to the middle of the distribution for the simulated sky maps. The choice of a beam of 4° also reduces the effect of point sources so that these are not affecting the result noticeably either.

It is also not possible to determine from these results whether we live in a Bianchi VII_h universe, or to get any further constraints on the value of the amplitude of non-Gaussianity, f_{NL}, as considered in section 9.5. Thus the best-fit Bianchi VII_h model is not ruled out by the statistic, nor is a value of f_{NL} between 100 and -100 which also

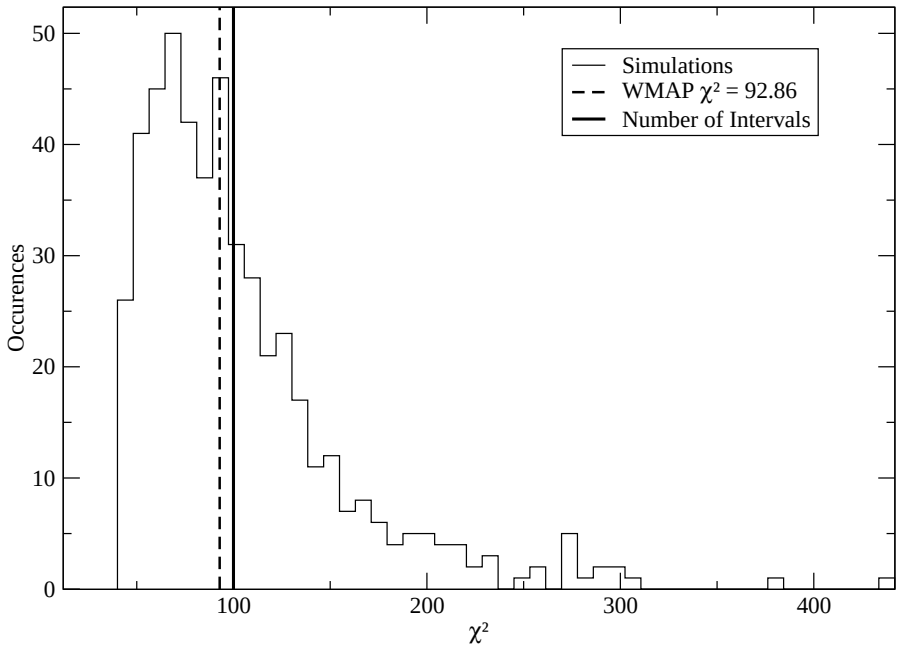

Figure 10.2: χ^2 distribution for 500 simulated CMB sky maps. The results from the WMAP data for the V1-channel is marked by a dashed line. As it is in the middle of the distribution, the gradient distribution from WMAP is not very different from the gradient distributions from the simulated maps. The WMAP result is also close to the number of intervals, 100 marked by the thick line, which is the χ^2 result expected if the gradients are from the same distribution.

includes the slow-roll scenario.

10.3 The Results for the Northern and Southern Hemispheres

There have been various reports on asymmetries in the northern and southern hemispheres in the WMAP data and other anomalies in the different hemispheres, see [42], [14],[23], [27],[39] and [40]. There are reports on a cold spot in the southern hemisphere, [42], and on a lack of structure in the northern, [39] and [40]. It is therefore interesting to look at the statistics in these two hemispheres separately.

In Figs.10.7, 10.8 and 10.9 the results are shown for the direction function and

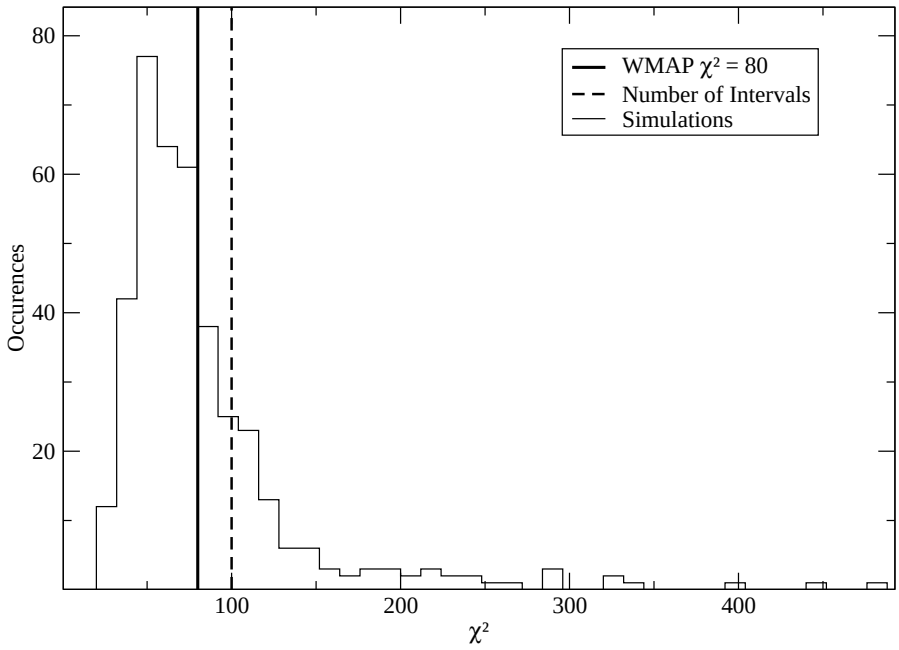

Figure 10.3: χ^2 distribution for 400 simulated CMB sky maps using the covariance matrix. The results from the WMAP data for the V1-channel is marked by a dashed line. The results differ some from the case without the covariance matrix. This shows that the results have some correlation.

the preferred direction statistic for the northern and southern hemispheres separately. Again simulations of the CMB with Gaussian anisotropies, using the ΛCDM model, have been used for comparison, and the results plotted as histograms of its distributions. For the maximum and minimum of the direction function, Eq.(5.1), the WMAP result for the V1-channel is found in the tail of the distribution in the northern hemisphere, while it is closer to the mean of the distribution in the southern. That is, the maximum value of the direction function is within 2σ in the northern hemisphere, and within 1σ in the southern hemisphere, while the minimum value is within 3σ in the northern hemisphere and within 1σ in the southern. For the ratio of the maximum to minimum the results are within 1σ for both the northern and the southern hemispheres, but the result in the northern hemisphere still lies furthest from the mean.

Also, the results for the northern and the southern hemispheres are at different ends of their distributions. While the maximum and minimum in the northern hemisphere is at the lower end of the distribution, the results for the southern hemisphere is at

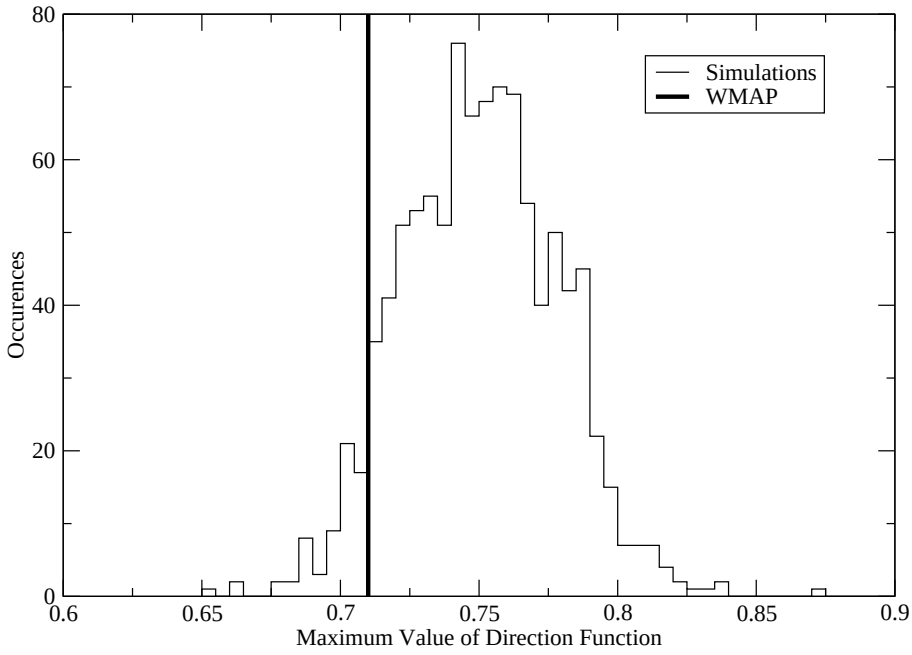

Figure 10.4: Maximum value of the direction function for simulated CMB sky maps compared to the result from the WMAP V1-channel. The WMAP result is marked by the thick line.

the higher end of the distribution, and as noted above the results in the northern hemisphere is further from the mean of the distribution. This effect can also be seen in the probability to exceed for this channel. For the maximum in the northern hemisphere it is 95.5% and for the minimum it is 99.5%. Thus only 0.5% of the distribution has smaller minimum values than the WMAP result. On the other hand, in the sourthern hemisphere these probabilities are 22.5% for the maximum and 15.2% for the minimum. This shows the asymmetry previously reported in the CMB. What is causing this effect has a greater impact on the maximum and minimum values of the direction function in the northern hemisphere than any effect in the southern hemisphere. But as the ratio of the maximum and minimum is not anomalously large, or small, there is no preferred direction in the northern hemisphere, or in the southern hemisphere.

The results for the other channels, of each frequency band, are given in Table 10.2 and Table 10.3. Again the results for the different channels are consistent. Also, from the results in the previous section it can be seen that the effect of the asymmetry is averaged out when considering the whole map, making the CMB sky close to the

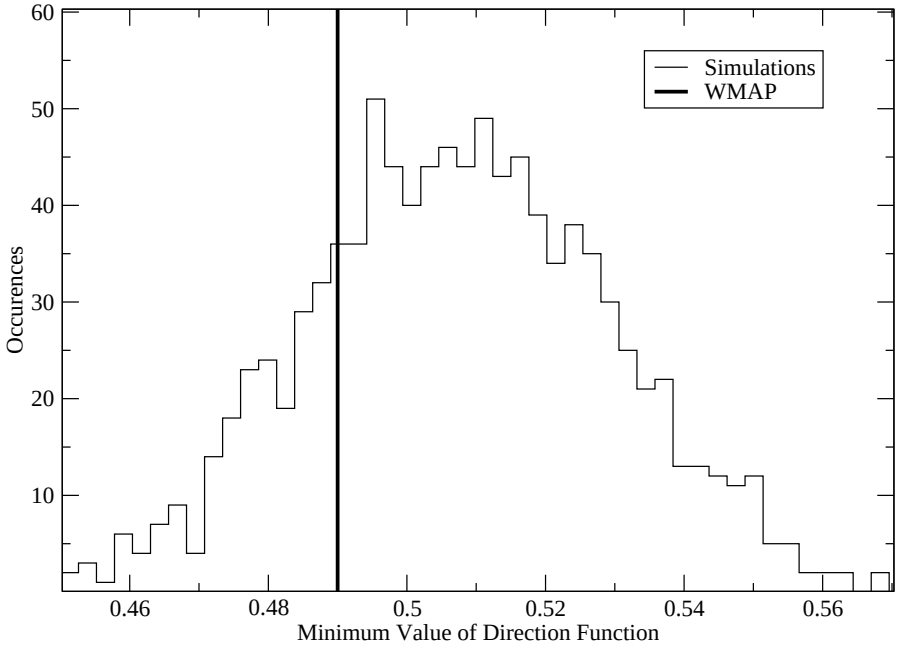

Figure 10.5: Minimum of direction function for 1000 simulations compared to the results for the WMAP V1-channel. The WMAP result is marked by the thick line.

simulated CMB results over all.

The difference between the results in the northern and southern hemispheres have also been found and compared to the simulations. In Fig.10.10 and Fig.10.11 the distributions of these results are plotted as histograms. The difference between the results found for the maximum and minimum is larger in the WMAP data than that found from most of the simulations, placing the WMAP results in the tail of these distributions. The result for the maximum value of the statistic is within 2σ, and the minimum value is within 3σ of the mean of these distributions. The PTE of these results are for the maximum 95% and for the minimum 98.8%.

Thus this large difference is not expected from simulations, and shows the asymmetry in the two hemispheres as well. Although the asymmetry in the CMB has been considered to be a statistical fluke by the WMAP team, independent research groups, using various methods, keep detecting it.

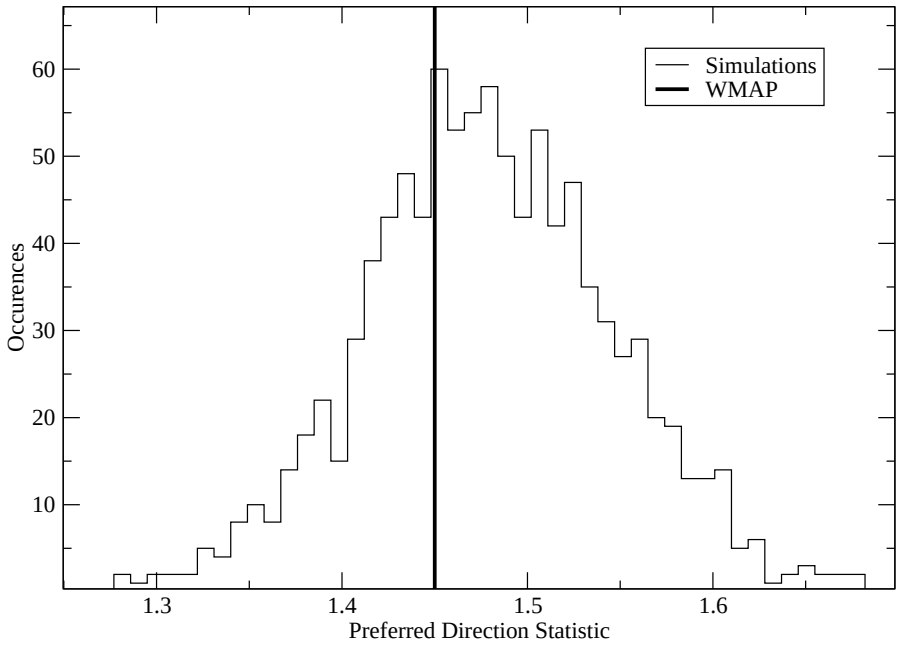

Figure 10.6: Preferred direction statistic, or the ratio of the minimum to maximum values of the direction function, for 1000 simulations compared to the WMAP V1-channel. The WMAP result is marked by the thick line.

Band	Maximum Value	PTE	Minimum Value	PTE	Ratio (max/min)	PTE
Q1	0.710	92.6	0.491	76.1	1.446	69.4
Q2	0.710	92.5	0.491	76.1	1.446	69.3
V1	0.713	91.2	0.490	78.9	1.455	64.5
V2	0.711	92.8	0.488	80.5	1.457	62.5
W1	0.715	92.6	0.491	81.3	1.456	63.3
W2	0.723	89.0	0.499	72.0	1.449	67.9
W3	0.708	96.9	0.495	79.2	1.430	78.1
W4	0.728	84.8	0.495	78.9	1.471	53.5

Table 10.1: Results for the preferred direction statistic and direction function for all the channels of Q, V and W - band. The maximum and the minimum of the direction function, as well as the ratio of these, are given along with their probability to exceed (PTE), which is given as %.

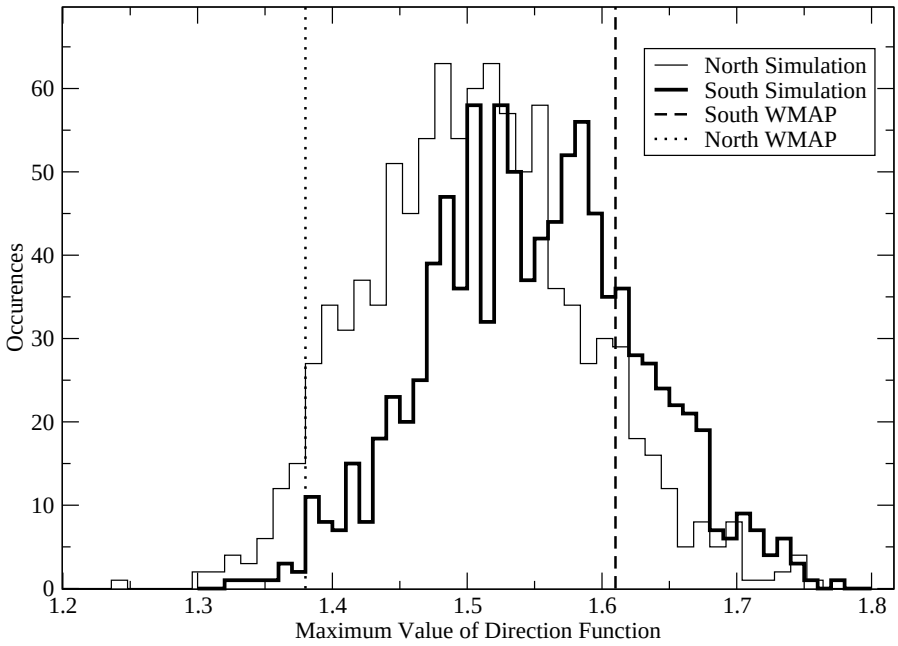

Figure 10.7: Maximum value of the direction function for the northern and southern hemisphere. The WMAP results for the V1-channel for each hemisphere has been compared to 1000 simulations.

Band	Maximum Value	PTE	Minimum Value	PTE	Ratio (max/min)	PTE
Q1	1.374	-	0.868	-	1.583	-
Q2	1.377	-	0.866	-	1.590	-
V1	1.380	95.5	0.864	99.5	1.597	18.7
V2	1.377	-	0.865	-	1.592	-
W1	1.385	-	0.881	-	1.572	-
W2	1.378	-	0.874	-	1.576	-
W3	1.370	-	0.865	-	1.584	-
W4	1.404	-	0.874	-	1.607	-

Table 10.2: Results for the preferred direction statistic and direction function for all the Q, V and W - band channels. These are the results for the northern hemisphere. There is currently no data on the PTE for the other channels other than V1. The PTE is given in %.

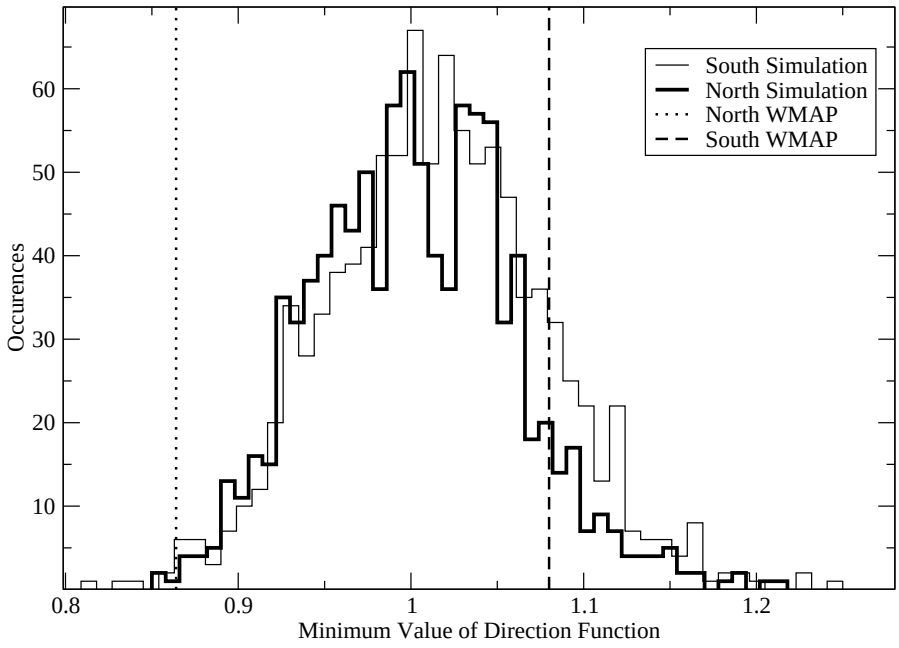

Figure 10.8: Minimum value of the direction function for the northern and southern hemispheres. The WMAP result for the V1-channel for each hemisphere has been compared to 1000 simulations.

Band	Maximum Value	PTE	Minimum Value	PTE	Ratio (max/min)	PTE
Q1	1.606	-	1.080	-	1.487	-
Q2	1.602	-	1.080	-	1.484	-
V1	1.610	22.5	1.080	15.2	1.491	64.7
V2	1.609	-	1.070	-	1.503	-
W1	1.598	-	1.070	-	1.493	-
W2	1.641	-	1.100	-	1.492	-
W3	1.595	-	1.100	-	1.450	-
W4	1.630	-	1.090	-	1.495	-

Table 10.3: Results for the preferred direction statistic and direction function for all the Q, V and W - band channels. These are the results for the southern hemisphere. There is currently no data on the PTE of the channels other than V1. The PTE is given in %.

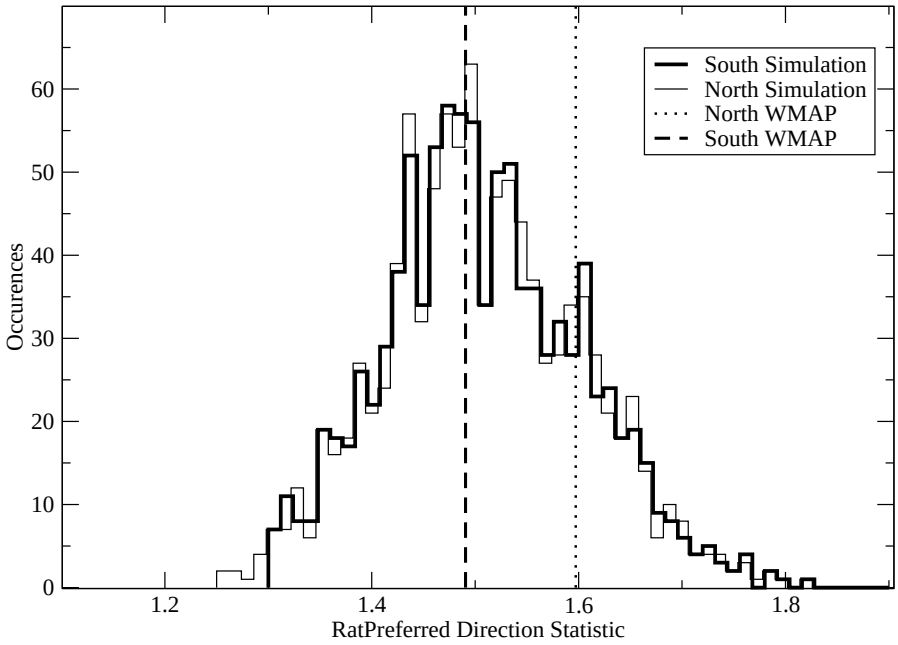

Figure 10.9: Ratio of the maximum and minimum values of the northern to southern hemispheres has been compared the the WMAP V1-channel for each hemisphere. This gives the preferred direction statistic for 1000 simulations used to make the distribution for each hemisphere.

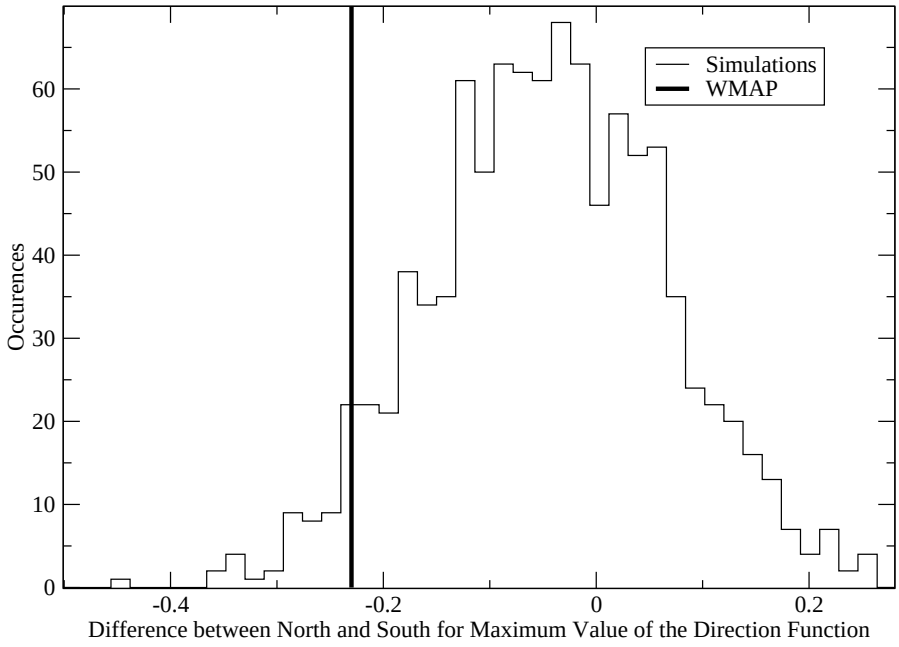

Figure 10.10: Difference of the maximum values of the direction function for the northern and southern hemispheres. This difference for the WMAP V1-channel has been compared to 1000 simulations.

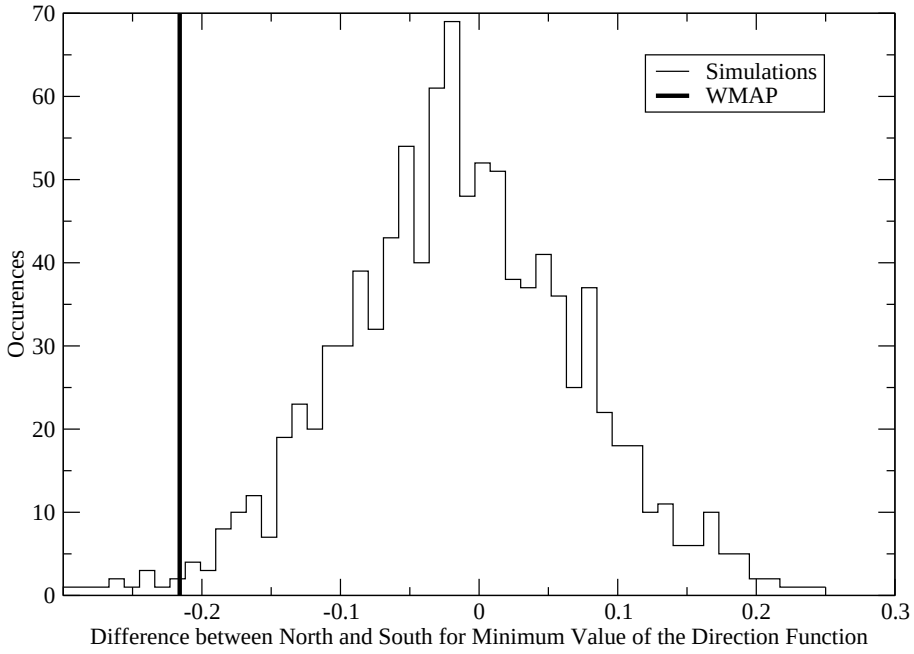

Figure 10.11: Difference of the minimum values of the direction function for the northern and southern hemispheres. This difference for the WMAP V1-channel has been compared to 1000 simulations.

Chapter 11

The WMAP data: Estimating the Gradient Power Spectrum

In chapter 4 the MASTER algorithm to estimate the temperature, polarization and gradient power spectra was presented, while the details of its implementation was reviewed in chapter 8. Here the results for the temperature and gradient power spectra are presented when using this algorithm. First the gradient power spectra for the ΛCDM model from simulations without noise, instrumental beam or mask will be presented. The positive gradient power spectrum has then been compared to simulations of the polarization E-mode power spectrum for the same model, also without noise, instrumental beam and mask. Then the temperature power spectrum results as a test of the MASTER algorithm are presented, and then the positive gradient power spectrum has been estimated for each of the three frequency bands. Finally the effect of point sources in the gradient power spectrum is investigated.

11.1 The Gradient Power Spectrum for the ΛCDM model

Before estimating the power spectra, from the WMAP data, simulations of the ΛCDM model were made, and the power spectra found from these. Here the power spectra of these simulated sky maps without noise, instrumental beam, or mask are shown in Fig.11.1 and Fig 11.2, and has been plotted as $C_l(l(l+1)/2\pi)$. The gradient power spectra have here been plotted up to $l_{max} = 2000$, and the average of 1000 simulations was used. This was a first approximation to what the gradient power spectrum for the ΛCDM model would look like.

The positive power spectrum, Fig.11.1, has acoustic peaks similarly to the temperature power spectrum. If only the C_l's of the positive gradient power spectrum is plotted it can be seen that this has the same shape as the temperature power spectrum, just with larger values of the C_l's. The negative power spectrum, however, does not show these features, Fig.11.2. It is only an increasing function.

From these plots it can be seen that the values of the C_l's are a lot large for the positive power spectrum than for the negative. So even thought there is a mixing of

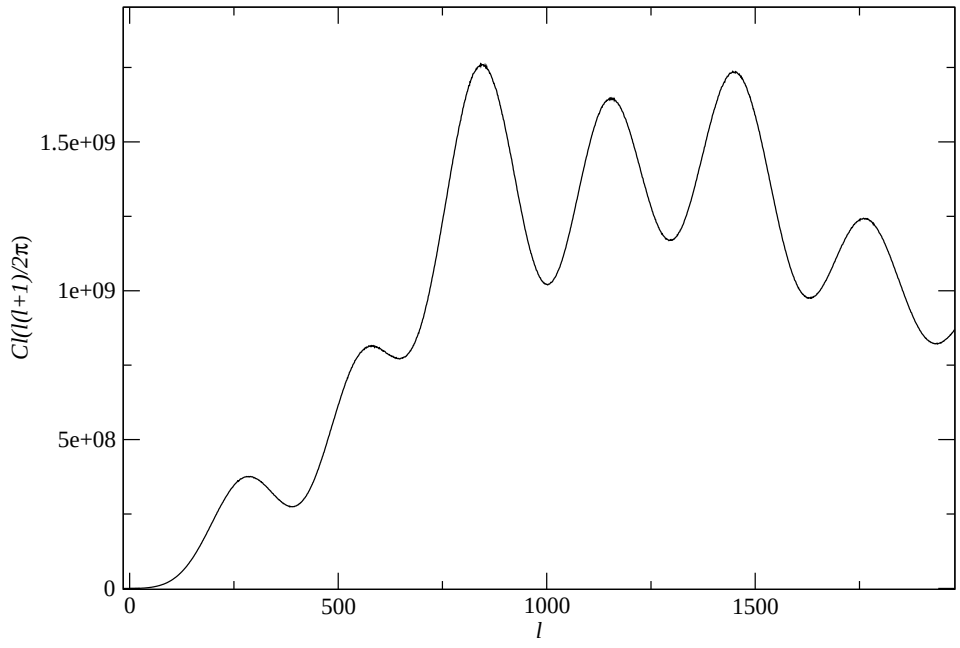

Figure 11.1: Gradient power spectrum from simulations of the temperature gradients using the ΛCDM model. Noise, instrumental beam and mask has not been applied to the simulated CMB sky maps in this case. This plot shows the positive gradient power spectrum which has acoustic peaks similarly to the temperature power spectrum.

the two, when estimating the power spectra, the negative component will not affect the positive significantly. But the other way around this is not the case. However, it is the positive component that has been focused on here, and which is estimated using the MASTER algorithm in section 11.3. To estimate the negative components the MASTER algorithm with pure modes, proposed by Smith, [41], would have to be used so the positive mode does not dominate. This is similar to the polarization power spectra where the E-mode is a lot stronger than the B-mode. Thus the positive gradient power spectrum is the easiest to estimate.

The positive gradient power spectrum can also be used as a consistency check of the E-mode polarization power spectrum, and these have both been plotted in Fig.11.3. Here the gradient power spectrum has been scaled by a factor of 2.2×10^{-8}.

In this figure the polarization power spectrum and gradient power spectrum is out of phase. However, they are not exactly out of phase, as can be seen at the lowest and highest l's in the plot. It is therefore not possible to find a function which is model

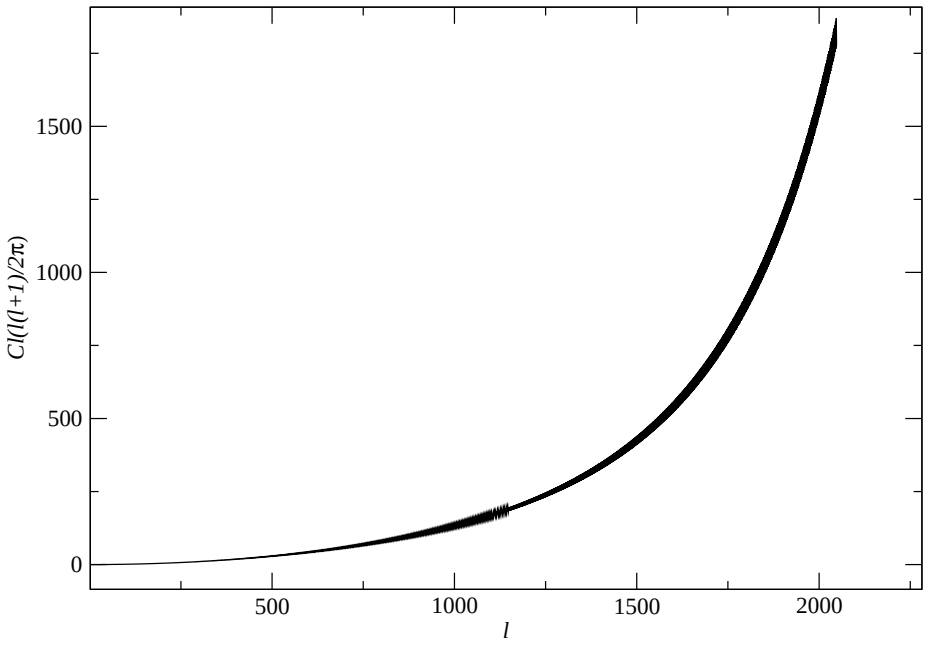

Figure 11.2: Gradient power spectrum from simulations of the temperature gradients using the ΛCDM model. Here the negative gradient power spectrum has been plotted, and this has been found without applying a mask or adding noise and instrumental beam to the CMB sky maps. The negative power spectrum has smaller values of C_l's than the positive, and it has not been estimated from the WMAP data here.

independent, and which gives the polarization power spectrum from the gradient power spectrum, or visa versa. Instead we can find out where the peaks of the polarization power spectrum correspond to a trough in the gradient power spectrum, or the other way around.

There are only two places where a peak and a trough are exactly out of phase in the two power spectra. These are a minimum in the E-mode polarization spectrum at approximately $l = 1155$ which is the fourth minimum. This corresponds to the fourth maximum in the gradient power spectrum. There is also a maximum in the polarization spectrum at approximately $l = 1300$ which is the fifth peak in the spectrum. This maximum corresponds to a minimum in the gradient power spectrum. The rest of the minima and maxima are shifted and not exactly out of phase.

However, the first few peaks and troughs are more interesting because these are easier to measure as they are on larger scales. So for the gradient power spectrum

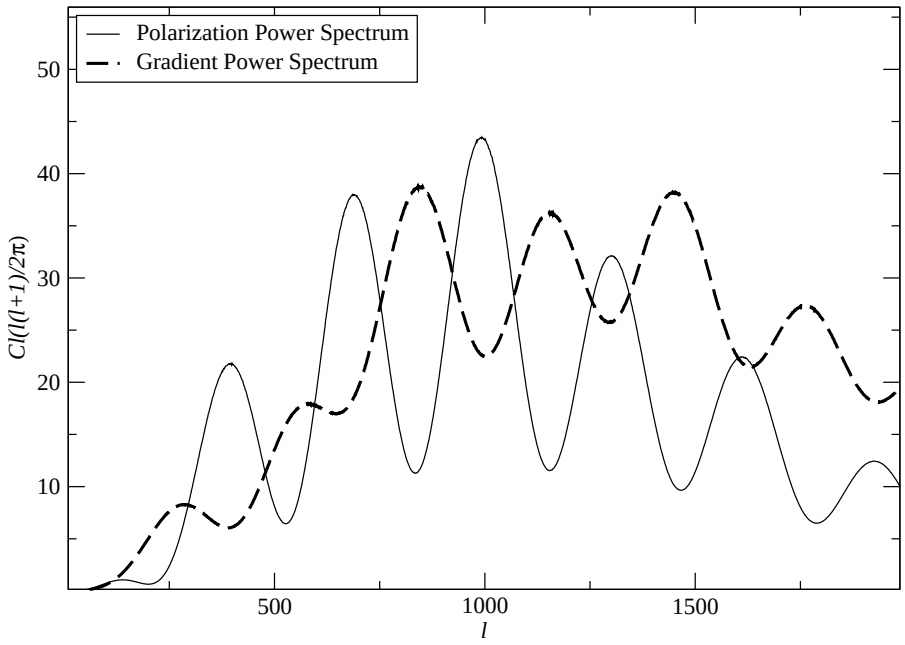

Figure 11.3: Positive gradient power spectrum compared to the E-mode polarization power spectrum. Both power spectra are averages of 1000 simulated CMB sky maps without noise, instrumental beam or mask. The gradient power spectrum has been scaled so that it can be displayed together with the E-mode power spectrum. This comparison can be used for consistency checks of the polarization E-mode power spectrum.

we find the first minimum at $l \approx 391$, while the polarization power spectrum has its first maximum at $l \approx 395$. The second maximum in the gradient power spectrum is at $l \approx 575$ with the corresponding polarization minimum at $l \approx 527$. The second minimum of the gradient power spectrum is at $l \approx 648$ corresponding to the third peak in the polarization power spectrum at $l \approx 687$. Finally the third peak in the gradient power spectrum can be found at $l \approx 845$, and this corresponds to the third minimum in the polarization power spectrum at $l \approx 835$. Although the exact positions of the maxima and minima are somewhat difficult to determine this can be used as guideline when comparing the two power spectra.

Comparison of these two power spectra can be used as a consistency check of the observational data. It may be possible to do this with the polarization data from Planck or QUIET, or some other experiment to observe the CMB polarization. It is

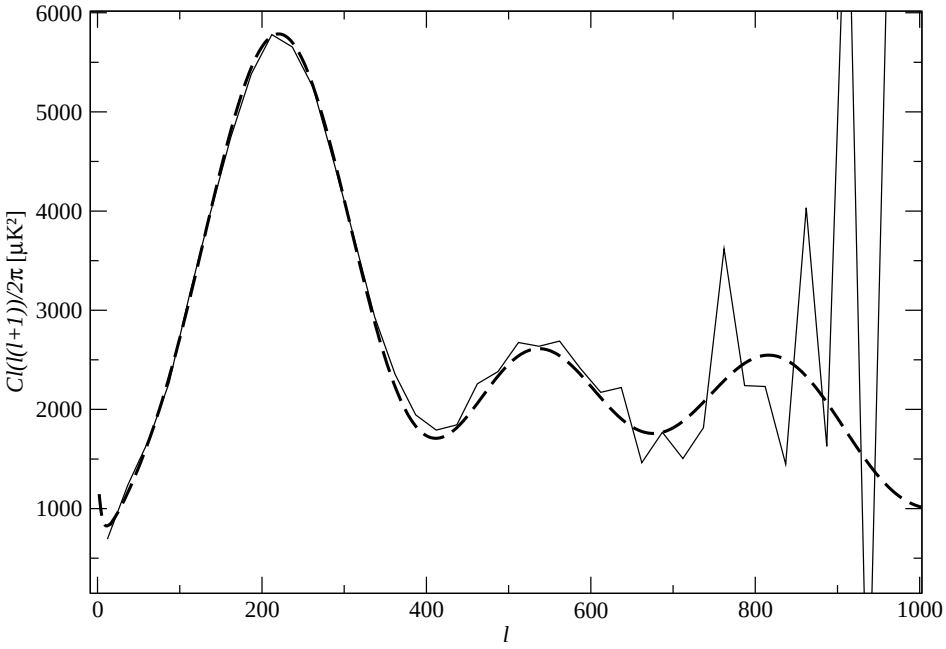

Figure 11.4: Temperature power spectrum for V-Band. The power spectrum has been binned with 25 C_l's in each bin. The black line is the power spectrum estimate from WMAP and the dashed line is the best-fit ΛCDM model spectrum.

also possible to find the second derivative of the CMB temperature. This would tell us where there are saddle points which would mean a quadrupole and E-mode polarization, see section 2.4.

11.2 Estimating the Temperature Power Spectrum

As a first step the MASTER algorithm was implemented for temperature only. The result from this can be seen below in Fig.11.4 for V-band. The estimated power spectrum from WMAP has been compared to the best-fit power spectrum from the ΛCDM model. As described in chapter 4, finding the temperature power spectrum is somewhat easier than finding the gradient power spectra, but the algorithm is similar. Thus by first finding the temperature power spectrum only smaller adjustments to the code was required to find the gradient power spectrum. This also meant that much of the algorithm could be test before applying it to the gradients.

As can be seen in Fig.11.4 the estimated power spectrum from WMAP is not a perfect fit. The somewhat larger values of this power spectrum, compared to the best-fit power spectrum, could be due to unresolved point sources. At smaller scales the power spectrum is also affected by noise, and here only the first and second peaks can be seen clearly. Data with less noise, and a better estimate of the noise power spectrum which would remove more of the noise, would leave more of the features of the power spectrum visible.

The temperature power spectrum, along with the E-mode polarization power spectrum and the TE cross correlation power spectrum, has been estimated by the WMAP team. Plots of their estimates for the seven year data can be found in Larson et al.,[32]. In the future it will be of interest to estimate the temperature power spectrum for even smaller scales making more of the acoustic peaks visible, and putting better constraints on cosmological parameters. As so much can be learned from the power spectrum better estimates is of great interest. In particular the high resolution data from Planck could provide better estimates.

11.3 Estimating the Gradient Power Spectrum

In Figs. 11.5, 11.6 and 11.7, are presented the positive gradient power spectrum for Q-band, V-band and W-band respectively. They have been compared to simulations of the gradient power spectrum with the noise and beam properties of each band. The simulated power spectra have then been estimated using the MASTER algorithm to remove these components along with the mask used. The errors are the standard deviation from these simulations. In total 1000 simulations were averaged to create the simulated power spectra.

The WMAP results are shown as points and the simulations as a curve. The error bars, the standard deviation of the simulations, have been placed on the WMAP results to better see whether these are with in one standard deviation of the simulations.

All the result for the three frequency bands for the WMAP data can be seen in Fig.11.8. Here the difference between the three WMAP gradient power spectra can be seen. In this plot it can also be seen that the best result is for the W-band, see Fig.11.7. It can also be seen that the point sources strength is different for the three bands with the largest values of C_l for Q-band. Fluctuations due to noise can also be seen in this plot.

Fig.11.9 shows the difference between the simulated power spectrum and the WMAP result for each frequency band on large scales. It can be difficult to see from the power spectra if there is a difference between simulations and WMAP on large scales, but this difference can be seen here.

Even though the noise is removed from the data it is only an approximation to the noise power spectrum based on simulations of Gaussian noise. Thus this will make the simulated power spectra look better as the noise here is almost the same as that which is removed.

As can be seen in Figs. 11.5, 11.6 and 11.7 the C_l's have somewhat larger values form

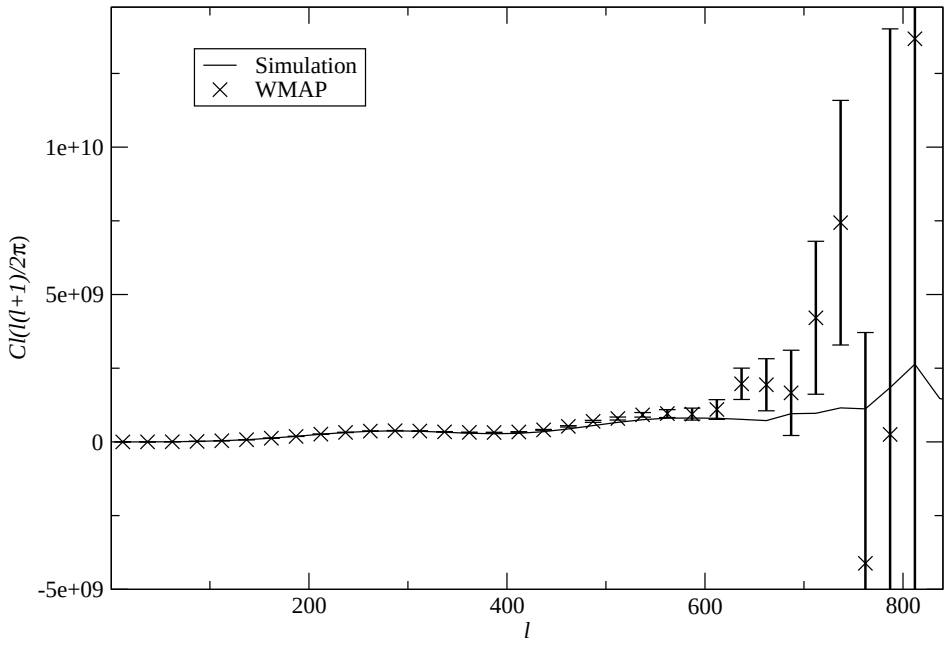

Figure 11.5: Positive gradient power spectrum for Q-band. There is an effect of point sources which makes the WMAP results differ from the simulations by increasing the values of the C_l's for the WMAP power spectrum. Here the WMAP result is plotted as points, and the simulated power spectrum is given by the solid line.

the second peak than that expected from simulations. As noted for the temperature power spectrum this could be the effect of unresolved point sources in the data.

To investigate the effect of point source in the gradient power spectrum the point source model was added to the simulated CMB sky maps. The gradient power spectrum from these simulations can be seen in Fig.11.10. The point source template used here has stronger point sources than that found in the WMAP data, so the effect is stronger in these simulations but it is still the same effect. A more accurate study can be done by converting the point source flux's in Jansky to temperature. The effect of the point source, to increase the values of C_l's at small scales, is also the same as that seen in the estimated gradient power spectra for each frequency band.

The presence of point sources increases the values of the C_l's, and any point sources that has not been masked out would cause this effect to be seen in the estimates from the WMAP data. However, some of the effect could be due to another problem related to the masking of the point sources. In this estimation the point sources have not been

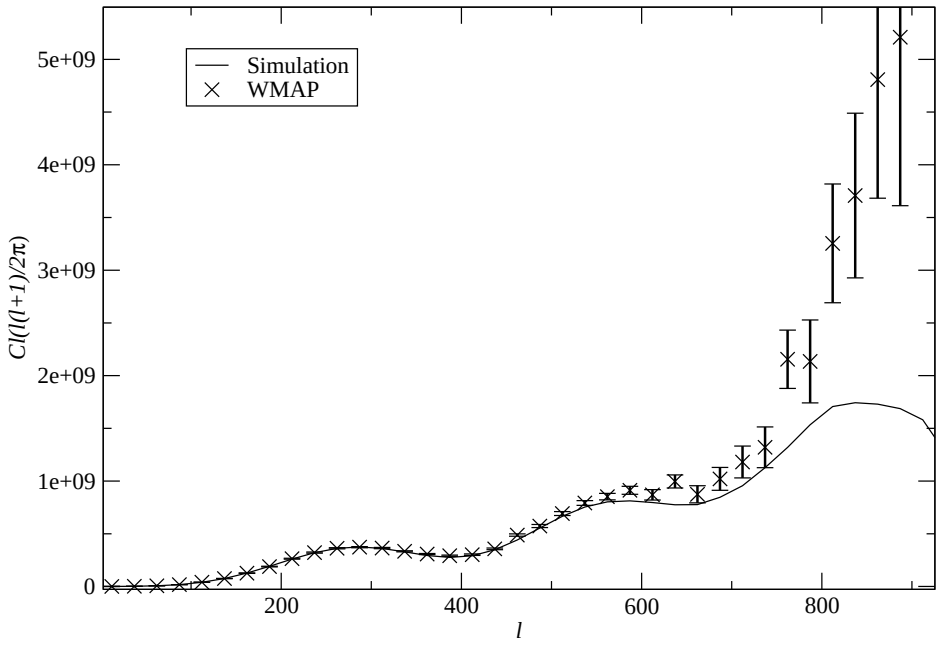

Figure 11.6: Positive gradient power spectrum for V-band. The point source problem can also be seen here. The V-band power spectrum is given by the points, and the solid line gives the simulated power spectrum for comparison.

masked out until after the gradients of the temperature map have been found. This could cause the gradients around the points source to be larger than if they were not there which could cause the larger values in the WMAP power spectra.

This is similar to the effect observed when masking out the point sources before finding the gradients. This causes border effects around the point source mask which is not masked out when applying the second mask. This increases the gradients around these points. However, this effect is stronger than that seen in the figures which is why this approach was not used here. This problem also makes point source more visible in the gradient power spectrum than in the temperature power spectrum were they can easily be masked out.

It might be possible to improve these results by masking out the point source in the temperature map, find the gradients, and then apply a larger point source mask to remove the border effects. This has not been attempted here. It might also be possible to go directly from the expressions for the gradients to the spin a_{lm}'s used when finding the power spectrum. This might also improve matters.

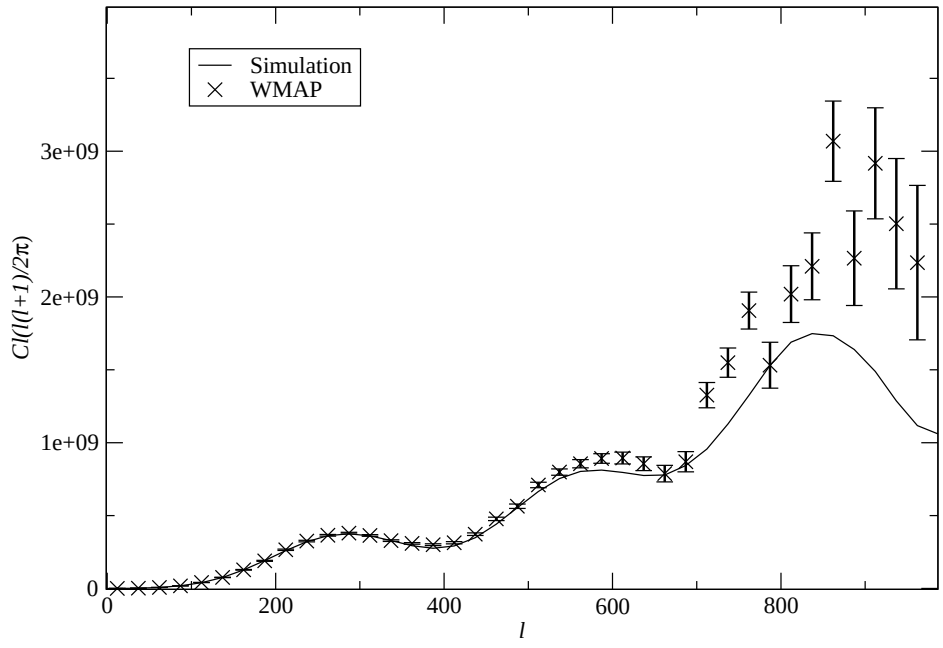

Figure 11.7: Positive gradient power spectrum for W-band. This is the best result for this power spectrum. But here, as in the other two bands, the effect of point sources can also be seen to increase the values of the C_l's. The W-band power spectrum is given by the points while the solid line gives the simulated power spectrum for comparison.

However, a lot of the effect of the point source is masked out by applying the point source mask after finding the gradients. This can be seen in Figs.11.11. But as the gradients make the point sources more visible in this power spectrum this can also be used to look for them.

Since the effect of point sources is visible in the positive gradient power spectrum this has been used to find the relationship between the strength of the point sources and the frequency of observation. The point sources as been found to follow a power law so that

$$S \propto \nu^{\beta}. \tag{11.1}$$

Here ν is the frequency and S is the strength of the point sources. The WMAP gradient power spectrum with point sources was compared to the simulated gradient power spectrum added to the gradient power spectrum of the point source template times an

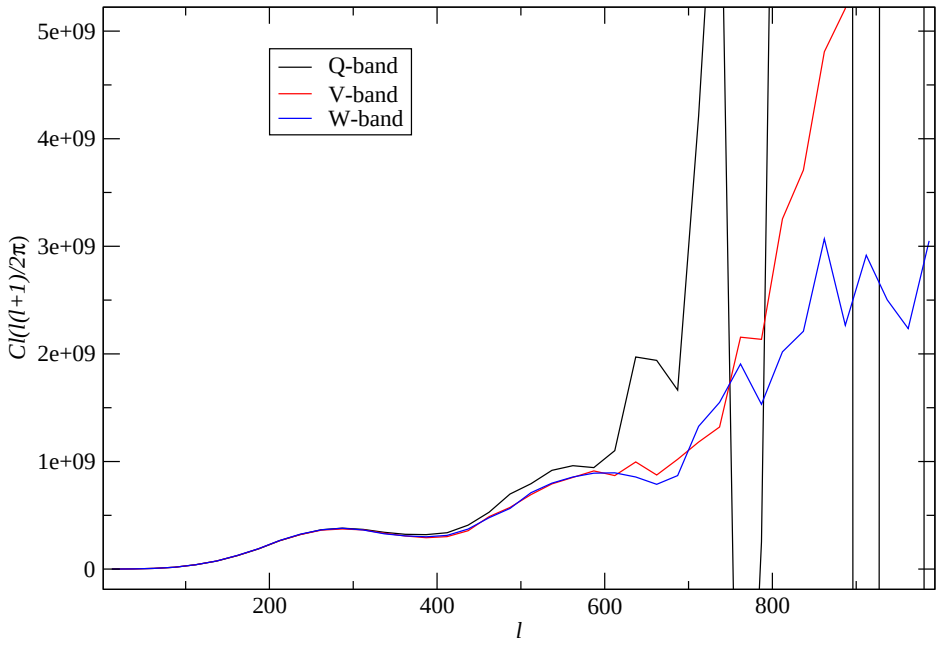

Figure 11.8: Positive gradient power spectra for Q-,V- and W-Band plotted together. Here the difference between the three bands can be seen.

amplitude A, so

$$C_l^{\text{diff}} = C_l^{\text{WMAP}} - (C_l^{\text{sim}} + AC_l^{\text{point sources}}).$$

By using the χ^2-test given by Eq.(5.6) the amplitude of the point source gradient power spectrum could be estimated by finding the lowest value of χ^2. These amplitudes could then be plotted against the frequency of each band and the power law fitted to these points. From this analysis it was found that $\beta = -2.8 \pm 0.1$, or

$$S \propto \nu^{-2.8\pm0.1}. \tag{11.2}$$

Previously $\beta \sim -2$ has been found for the point sources in the WMAP data, see Bennett et al., [6].

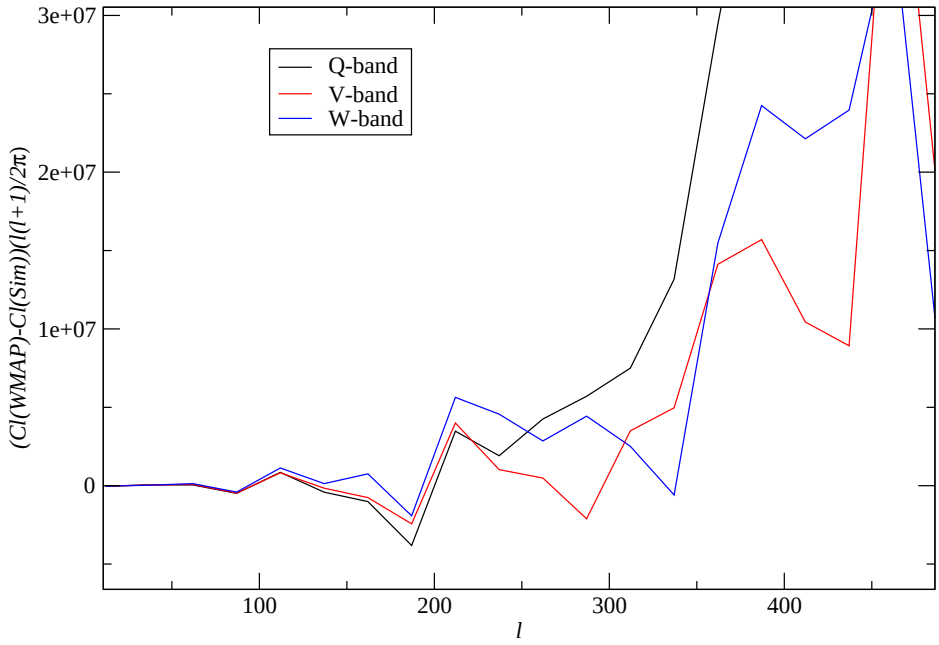

Figure 11.9: Difference between the simulated power spectra and the WMAP power spectra for smaller values of l. Although it is difficult to see in the plot of the power spectra for the frequency bands, there is a difference at larger scales as well between the simulations and the WMAP results.

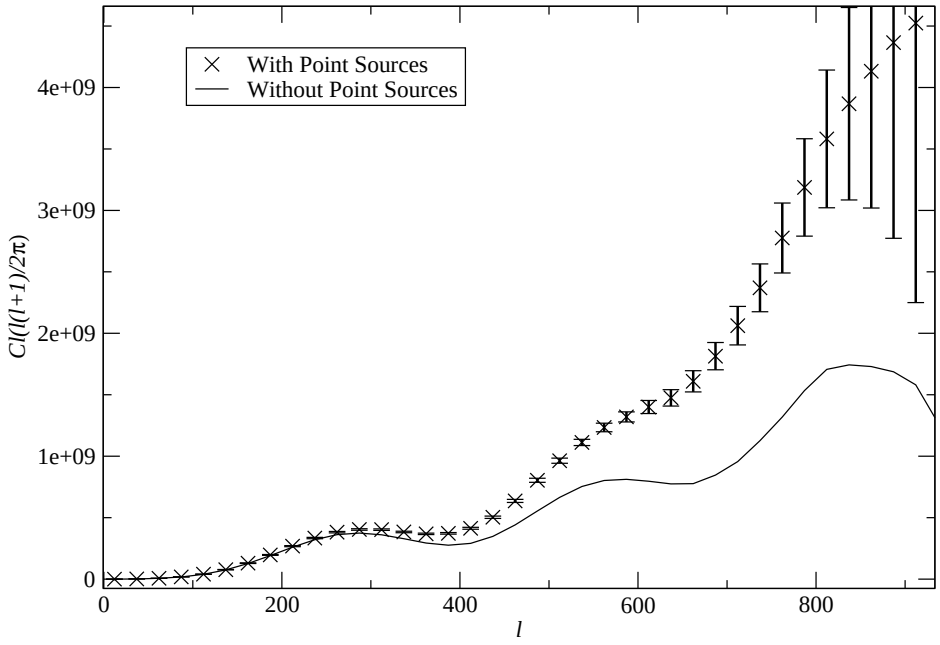

Figure 11.10: Simulations of the gradient power spectrum for V-band with and without point sources that has not been masked out. The point sources increases the absolute values of the gradients and therefore the C_l's.

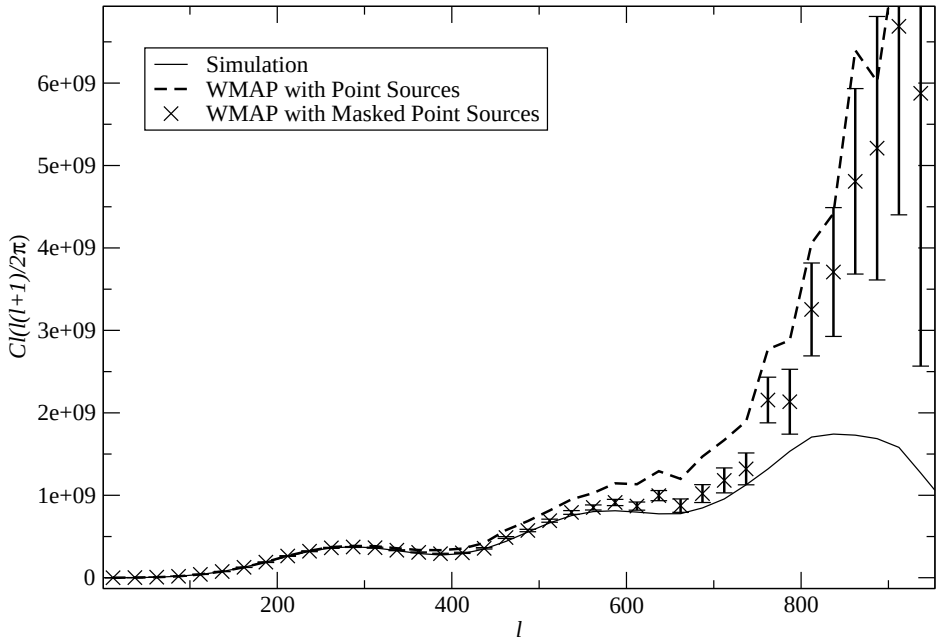

Figure 11.11: Positive gradient power spectrum for V-band with and without point sources that has not been masked out. These power spectra have been compared to the WMAP result for V-band with point source simulated sky maps with point source mask, but no point sources.

Chapter 12

Summary and Conclusion

Since the WMAP data became available it has been subject to many statistical tests. From these tests there are reports on anomalies and an asymmetry in the northern and southern hemispheres along with detections of non-Gaussianity. In this work statistical tests using the gradients of the temperature maps have been applied to the seven year WMAP data. One of these statistics can detect a preferred direction possibly due to some pattern in the CMB. But these statistical tests could also detect other anomalies.

The gradients of the temperature maps were first tested using the Kolmogorov-Smirnov test and χ^2-test. The gradient distribution of simulated sky maps were compared to the distribution of the WMAP data, and it was tested whether these came from the same distribution or not. From the results this seems to be the case, and no anomalies were detected when applying these tests. Thus the simulated maps were a reasonable approximation to the WMAP data.

The other statistical tests that were applied to the data were the maximum and minimum of the direction function, which is the dot-product of gradients and unit vectors on the sphere, and the preferred direction statistic which is the ratio of these. The direction function was found for 1000 simulated maps and its maximum and minimum along with the ratio were compared to the WMAP data. It was found that the maximum value of the direction function for WMAP lie within 2σ of the mean of the distribution of results from simulated CMB sky maps. The minimum of this function was found to lie within 1σ. The ratio of these, or the preferred direction statistic, was also within 1σ of the mean. This was the case for the results all the different channels of the WMAP satellite. These results show that there does not seem to be any anomaly or preferred direction in the CMB as the WMAP result is close to the results from the simulated sky maps. This is for a resolution of $N_{\text{side}} = 128$, and smoothing with a Gaussian beam of 4°.

However, when looking at the northern and southern hemispheres separately an asymmetry was detected as reported by many research groups. The results for the two hemispheres are at opposite sides of their distributions for the minimum and maximum values of the direction function. The WMAP result for the northern hemisphere

is within 2σ for the maximum and within 3σ for the minimum. The probability to exceed was also found to be 99.5% for the minimum value. However, in the southern hemisphere the results are within 1σ for these statistics.

The difference between the results in the two hemispheres were also larger than that expected from most of the results from the simulated sky maps. The difference between the maximum values were found to be within 2σ and the difference between the minimum values were found to be within 3σ. The probability to exceed for these results were found to be 95% for the maximum and 98.8% for the minimum. Thus, the asymmetry is detected with the results differing more from the simulated sky maps in the northern hemisphere than in the southern.

When we look at the preferred direction statistic it is found that, for both the northern and southern hemispheres, the result is within 1σ, but there is still a difference. But although the asymmetry is seen in the direction function there is still no preferred direction in either of the hemispheres as the preferred direction statistic is very close to the results from the simulated sky maps. So the effect causing the large difference in the maximum and minimum of the direction function does not cause a preferred direction.

The maximum of the direction function was also found from simulations with various templates and models. The effect of a dipole, foregrounds and point sources on this function was tested for various amplitudes. It was found that small amplitude dipoles and foregrounds were detected, with an amplitude of 0.3 at 2σ for the dipole and 0.04 at 2σ for the foregrounds. The point source template required larger amplitudes to be detected with 246 at 2σ. By comparing these with the WMAP results it could also be seen that the results are not influenced by a dipole in the data, residual foregrounds that have not been masked out, or point sources.

This was also tested for the Bianchi VII_h model which describes a rotating universe. This model has features that resembles those seen in the WMAP data, and could possibly explain the asymmetry. But the direction function cannot distinguish between the best-fit model and the ΛCDM model, and an amplitude of 1.22×10^{-6} at 2σ was found. It might, however, be interesting to evaluate the direction function for the two hemispheres individually for simulations with this model to see if it could be detected as an asymmetry. The statistics might then be able to detect this model for smaller amplitudes.

The direction function was also found for a model with primordial non-Gaussianity. Large values of the primordial non-Gaussianity amplitude f_{NL} was required to see a difference in the results with $f_{NL} = 2957$ or $f_{NL} = -2732$ at 2σ. Thus, as current constraints are $-100 < f_{NL} < 100$, this does not give any further information, and other methods should be used to constrain the value of f_{NL}.

From the gradients two power spectra can be estimated. Here the MASTER algorithm was used to estimate the positive gradient power spectrum which has acoustic peaks similarly to the temperature power spectrum. This power spectrum was estimated as it might give some further information about the CMB, and could be used as a

consistency check. Some of its uses, that were explored here, were a comparison with the polarization E-mode power spectrum and finding the relation between the strength of the point source and the frequency of observation. The comparison of the positive gradient power spectrum with the E-mode polarization power spectrum was done for the average of 1000 simulated sky maps up to $l_{\max} \approx 2000$. As the power spectra are out of phase a model invariant function could not be found which relates the two. However, the minima and maxima of these power spectra were compared and a guide was made of where these are with respect to each other. Generally a maximum in one power spectrum corresponds to a minimum in the other, or close to a minimum. This can then be used as a consistency check of the E-mode polarization power spectrum.

The positive gradient power spectrum was also used to detect point sources. Simulations with the point source template was made to see how these would effect the power spectrum. The amplitude of the point sources was then approximately that found in the WMAP data. This showed that the values of the C_l's increases when there are point sources in the data as these give larger gradients.

In the estimated positive gradient power spectra from the WMAP data a small effect was seen that increases the values of the C_l's. This could be due to unresolved point sources that has not been masked out. There might also be some effect from the point sources that have been masked out as these are not masked out until after the gradients have been found. This could increase the values of the gradients around the point sources. However, applying the point source mask before finding the gradients would cause border effects. A better way to mask out the point sources when finding the gradients should therefore be devised.

But as the effect of point sources can easily be seen in this power spectrum it could be used to find the relationship between their strength and the frequency of observation, $S \propto \nu^{\beta}$. Here $\beta = 2.8 \pm 0.1$ was found.

Since the preferred direction statistic, and the direction function, are very general statistical tests it is not surprising that they are not very sensitive to some effects. But this also makes them useful as they can just be applied to the data to see if there is anything there of interest. Thus it is still a useful tool in CMB analysis.

From the results of the WMAP data no detection of a preferred direction was made. But an asymmetry in the two hemispheres was detected. In particular the results in the northern hemisphere differ from that expected from the simulated sky maps. Still this anomaly does not have a preferred direction. What is causing this anomaly is not known, and further exploration of this is of interest.

Because the direction function is very general it is not very sensitive to the Bianchi VII_h model or the model with primordial non-Gaussianity. The best-fit amplitude of the Bianchi VII_h model is not ruled out, [28], neither are values of the amplitude of primordial non-Gaussianity, f_{NL}, between 100 and -100. So the slow-roll inflationary scenario is not ruled out by this statistic. To learn more about these models, and inflation, statistics which are sensitive to these effects have to be applied to the data. The search for signs of non-Gaussianity and inflation is ongoing, and with the Planck

data further constraints on inflationary models may be found.

However, the direction functions sensitivity to foregrounds and dipoles shows how important it is that these effects does not contaminate the data. From the statistics sensitivity to point sources these do not seem to affect the results from the WMAP data with the beam and resolution used here. When looking for point sources using the direction function, or preferred direction statistic, it would be more interesting to use a smaller beam than that applied to the data here. This would make the point sources more visible in the data. But due to time constraints on this project this was not done here. It would also be of interest to apply these statistical tests to the WMAP data using smaller beams as this would give more information.

Although no model independent function could be found that gives the positive gradient power spectrum from the polarization E-mode power spectrum a guide was still made which can be used as a consistency check. This could be a useful tool when better estimates of the E-mode polarization power spectrum have been made. It might also be of interest to find the second derivative and compare this to the E-mode polarization spectrum as the saddle points correspond to the quadrupole needed to create this polarization.

But when finding the positive gradient power spectrum a better way to mask out the point sources should be devised as the method used here might leave some residual effect which increases the values of the C_l's. Other point source which have not been catalogued may also contribute to this effect. With higher resolution data, with less noise, it will also be possible to get a better estimate the gradient power spectrum on smaller scales than found here. But the large effect of point sources in this power spectrum did make it possible to find a power law between the strength of the point sources and the frequency of observation. So even though point sources affect the gradient power spectrum this can also be very useful. It might also be possible to use this power spectrum to find the power law for point sources that has not been catalogued, and therefore not been masked out. Any other uses of this power spectrum should also be explored in the future as it might provide new insights.

Bibliography

[1] Han Atkinson, Elementary Numerical Analysis, *John Wiley and Sons*, third edition, 2004.

[2] R.J.Barlow, Statistics, A Guide to the Use of Statistical Methods in the Physical Sciences, *John Wiley and Sons*, 1989.

[3] J.D.Barrow et al., Universal rotation: how large can it be?, *M.N.R.A.S.* , 1985, 213, pp. 917-943.

[4] N.Bartolo et al., Non-Gaussianity from Inflation: Theory and Observations, 2004, *astro-ph/0406398v2*.

[5] C.L.Bennett et al., The Microwave Anisotropy Probe (MAP) Mission, *ApJ*, 583, pp. 1-23, 2003, *astro-ph/0301158v1*.

[6] C.L.Bennett et al., First Year Wilkinson Microwave Anisotropy Probe (WMAP) Observations: Foreground Emission, *ApJ*, 2003, *arXiv:1001.4758v2* .

[7] C.L.Bennett et al., Seven-year Wilkinson Microwave Anisotropy Probe (WMAP) Observations: Are There Cosmic Microwave Background Anomalies?, *ApJS*, 2011, *arXiv:1001.4758v2 [astro-ph.CO]*.

[8] E.F. Bunn, and D.Scott, A Preferred-Direction Statistic for Sky Maps, *M.N.R.A.S*, 2000, 313, pp. 331, *astro-ph/9906044*.

[9] Petter Callin, How to calculate the CMB spectrum, 2006, *astro-ph/0606683v1*.

[10] C.B.Collins and S.W.Hawking, The rotation and distortion of the Universe, *M.N.R.A.S.*, 1973, 162, pp. 307-320.

[11] P.Creminelli et al., Limits on f_{NL} parameters from the Wilkinson Microwave Anisotropy Probe three-year data, *JCAP*, 2007, *astro-ph/0610600*.

[12] P.Dennery and A.Krzywicki, Mathematics for Physicists, *Dover*, 1996.

[13] Scott Dodelson, Modern Cosmology, *Academic Press*, 2003.

[14] H.K.Eriksen et al., Hemispherical Power Asymmetry in the Three-year Wilkinson Microwave Anisotropy Probe sky maps, *ApJ*, 2007, *astro-ph/0701089v2*.

[15] H.K. Eriksen et al., Testing for Non-Gaussianity in the Wilkinson Microwave Anisotropy Probe Data: Minkowski Functionals and the length of the Skeleton, *ApJ*, 2005, *astro-ph/0401276v3*.

[16] Ø.Grøn and S.Hervik, Einstein's General Theory of Relativity with Modern Applications in Cosmology, *Springer*, 2007.

[17] B.Gold et al., Seven-Year Wilkinson Microwave Anisotropy Probe (WMAP) Observations: Galactic Foreground Emission, *ApJS*, 191, 2010, *arXiv:1001.4555v3 [astro-ph.GA]*.

[18] K. M. Górski et al., The HEALPix primer, *astro-ph/9905275*, 2000.

[19] K.M. Górski et al., HEALPix – a Framework for High Resolution Discretization, and Fast Analysis of Data Distributed on the Sphere, *ApJ*, 2005, 622, pp. 759-771, *astro-ph/0409513v1*.

[20] A.H.Guth, Inflationary universe: A possible solution to the flatness and horizon problems, *Physical Review D*, 1981, 23.

[21] F.K.Hansen et al., Gabor Transforms on the Sphere with Applications to CMB Power Spectrum Estimation *M.N.R.A.S.*, 2002, *astro-ph/0207464v1*.

[22] F.K.Hansen et al., Fast cosmic microwave background power spectrum estimation of temperature and polarization with Gabor transforms, *M.N.R.A.S.*, 2003, 343, pp. 559-584.

[23] D.Hanson et al., Directionality in the Wilkinson Microwave Anisotropy Probe polarization data, *M.N.R.A.S.*, 2007, 381, pp. 2-6.

[24] J.B.Hartle, Gravity An Introduction to Einstein's General Relativity, *Pearson Eduction, Inc., publishing as Addison Wesley*, 2003.

[25] C. Hikage et al., Limits on primordial non-Gaussianity from Minkowski Functionals of the WMAP temperature anisotropies, *M.N.R.A.S.*, 2008, 389, pp. 1439-1446.

[26] E.Hivon et al., MASTER of the cosmic microwave background anisotropy power spectrum: A fast method for statistical analysis of large and complex cosmic microwave background data sets, *ApJ*, 2002, 567, pp. 2-17.

[27] J.Hoftuft et al., Increasing evidence for hemispherical power asymmetry in the five-year WMAP data, *ApJ*, 2009, *astro-ph/0903.1229v2*.

[28] T.R.Jaffe et al., Evidence of vorticity at large angular scales in the WMAP data: A violation of the cosmological isotropy?, *ApJ* , 2005, *astro-ph/0503213v2*.

[29] T.R.Jaffe et al., Fast and efficient template fitting of deterministic anisotropy cosmological models applied to WMAP data, *ApJ*, 2006, *astro-ph/0603844v1*.

[30] Jaroski et al., Design, Implementation and Testing of the MAP Radiometers, *ApJS*, 2003, 145, *astro-ph/0301164v2*.

[31] J.Kaplan et al., CMB Polarization as complementary information to anisotropies, 2003, *astro-ph/0310650v3*.

[32] D.Larson et al., Seven-year Wilkinson Microwave Anisotropy Probe (WMAP) Observations: Power Specta and WMAP-derived Parameters, *ApJS*, 2011, *arXiv:1001.4635v2 [astro-ph.CO]*.

[33] D.Langlois, Isocurvature Cosmological Perturbations and the CMB, *C. R. Physique 4*, 2003, pp.953-959.

[34] M.Liguori et al., High-Resolution Simulations of Cosmic Microwave Background Non-Gaussian Maps in Spherical Coordinates, 2003, *astro-ph/0306248v1*.

[35] M.Liguori et al., Temperature and Polarization CMB Maps from Primordial Non-Gaussianities of the local type, 2007, *astro-ph/0708.3786v3*.

[36] A.Mazumdar and Jonathan Rocher, Particle physics models of inflation and curvaton scenario, 2010, *arXiv:1001.0993v2 [hep-ph]*.

[37] Page et al., The Optical Design and Characterization of the Microwave Anisotropy Probe, *ApJ*, 2003, 585, pp. 566-586, *astro-ph/0301160v1*.

[38] A.A. Penzias and R.W. Wilson, A Measurement of the Excess Antenna Temperature at 4080 Mc/s, *ApJ*, 1965, 142, pp.419-421.

[39] C.Räth et al., A Scaling Index Analysis of the WMAP three year data: Signatures of non-Gaussianities and Asymmetries in the CMB, *M.N.R.A.S*, 2007, *astro-ph/0702163v1*.

[40] C.Räth et al., A model-independent test for scale dependent non-Gaussianities in the cosmic microwave background, 2009, *astro-ph/0810.3805v2*.

[41] K.M.Smith, Pseudo-Cl estimators which do not mix E and B modes, *Physical Review D*, 2006, 74.

[42] P.Vielva et al., Detection of Non-Gaussianity in the Wilkinson Microwave Anisotropy Probe First-year data using Spherical Wavelets, *ApJ* , 2004, 609, pp. 22-34.

[43] B.D.Wandelt et al., Fast Convolution on the Sphere, *ApJ*, 2000, *astro-ph/0008227v2*.

[44] B.D.Wandelt et al., The Pseudo-Cl method: cosmic microwave background anisotropy power spectrum statistics for high precision cosmology 2000, *astro-ph/0008111v1.*.

[45] A.P.S.Yadav and B.D.Wandelt, Evidence of Primordial non-Gaussianity (f_{NL}) in the Wilkinson Microwave Anisotropy Probe three-year data at 2.8σ, *PHYSICAL REVIEW LETTERS*, 2008, 100.

[46] M.Zaldarriaga and U.Seljak, All-sky analysis of polarization in the microwave background, *Physical Review D*, 1997, 55, pp. 1830-1840.

[47] M.Zaldarriaga, The Polarization of the Cosmic Microwave Background, 2003, *astro-ph/0305272v2*.